Extension of a Reflection-Mode Digital Gradient Sensor (r-DGS) to Study Impact Induced Deformations, Damage, and Fracture

by

Amith Subhash Chandra Jain

A thesis submitted to the Graduate Faculty of
Auburn University
in partial fulfillment of the
requirements for the Degree of
Master of Science

Auburn, Alabama
May 10, 2015

Keywords: experimental mechanics, optical metrology, slope measurement, Non-destructive evaluation, fracture mechanics

Approved by

Hareesh V Tippur, Chair, McWane Professor of Mechanical Engineering
Jeffrey C Suhling, Quina Distinguished Professor of Mechanical Engineering
James S Davidson, Professor of Civil Engineering

Abstract

Reflective structures such as space mirrors, silicon wafers, solar reflectors, microelectronic devices to name a few, are made of stiff and brittle materials. They often suffer deformations and catastrophic failure when subjected to thermo-mechanical stresses. In these situations, accurate quantification of mechanical stresses and deformations is essential for safety and structural integrity. Non-contacting methods to perform such measurements at relatively high sensitivities and low cost are important when small deflections are to be detected and quantified.

Motivated by these, a full-field optical technique called reflection-mode Digital Gradient Sensing (r-DGS) has been extended in this thesis to the measurement of small angular deflections of light rays (~$10x10^{-6}$ radians) reflected off a specularly reflective surface when subjected to non-uniform quasi-static or dynamic stress fields. The working principle of the method along with its governing equations relating angular deflections of light rays to surface slopes is explained.

The feasibility of the method to study deformations in thin plates is first demonstrated under quasi-static conditions by quantifying out-of-plane deflections of a thin silicon wafer subjected to controlled loading and boundary conditions. The measurements performed on a clamped circular plate subjected to a central deflection are successfully compared with the theoretical solutions. The curvatures are also evaluated from the measured surface slopes and compared to their theoretical counterparts. From the measured slope data, surface topography is successfully deduced through numerical integration. Following these baseline experiments, the method is extended to the measurement of surface slopes during stress wave propagation in a thin plate by coupling r-DGS methodology with high-speed photography. Time-resolved measurements for the problem of a thin 'free-free' PMMA disk subjected to projectile impact by a steel ball is selected for this demonstration. The surface slopes in two orthogonal planes have been successfully measured during the transient event and used to evaluate topographical informa-

tion. The topographic measurements are successfully complemented using 3D elasto-dynamic finite element computations.

Next, the feasibility of r-DGS method to detect disbond and damage in layered plates is demonstrated. First a disbond detection study is carried out on an adhesively bonded bi-layered PMMA plate with an embedded defect. Subsequently its applicability is extended to detect delamination caused by the mechanical impact on glass fiber reinforced epoxy composite sheets. Thermal excitation of the damaged plates is used in these experiments to induce deformations and detect the resulting manifestations of the defect or damage by examining aberrations in the surface slope fields. The methodology is also employed to demonstrate the method's feasibility to map thermo-mechanical deformations of flip-chip silicon-die attachments to a ceramic substrate.

The r-DGS method is finally extended to study fracture mechanics problems by mapping surface slopes in the close vicinity of a deformed crack tip in edge cracked specimens under mode-I and mixed-mode (mode-I/II) loading conditions. Both quasi-static and dynamic loading configurations involving inertially loaded stationary crack and growing crack are studied and the corresponding stress intensity factor histories are evaluated. The stress intensity factors measured in these cases are in agreement with the analytical or finite element results demonstrating the feasibility of r-DGS to experimental fracture mechanics.

Acknowledgments

I would like to thank my advisor, Dr. Hareesh V. Tippur, for his guidance and support throughout my study at Auburn University. I am immensely grateful to him for providing me an opportunity to work in Laboratory for Failure Mechanics and Optical Techniques which has been one of the most fulfilling experiences of my life. I would also like to thank Dr.Jeffrey C. Suhling and Dr. James S. Davidson for agreeing to serve as my committee members as well as teaching me various courses that helped to move my research forward. I would also like to thank Dr. Michael E. Miller for assisting me with metal vapor deposition.

I gratefully acknowledge National Science Foundation (grant # CMMI- 1232821) and Department of Defense (grants # W31P4Q-14-C-0049, W911NF-12-1-0317) for extending financial and equipment support for this research. I would also like to thank my colleagues Balamurugan, Robert, Vinod, Oscar, Austin and Kailash who have guided me many a times and helped my research move forward.

Table of contents

List of Tables

List of Figures

Chapter 1 : Introduction

1.1 Motivation

Reflective engineering structures such as space mirrors, silicon wafers, solar reflectors, microelectronic devices, to name a few, are made of stiff, brittle materials which suffer deformations and failure when subjected to thermo-mechanical stresses. Quantification of mechanical fields in these is essential for structural design and integrity. Non-contacting methods to perform such measurements at relatively high sensitivities are needed when small deflections are to be detected and quantified in stiff structures and materials. Accurate measurement of mechanical quantities often proves to be a challenge as experimentalists rely on indirect data because tools to measure the desired quantity is complicated or does not exist. Quantities of primary interest in mechanical design are stresses and deformations due to external loading. A few methods such as moiré techniques, laser speckle photography and interferometry are capable of measuring quantities related to strain. Out-of-plane deformation measurements either require a complex experimental setup or use of expensive measurement tools. Techniques such as laser speckle photography, shadow moiré method and 3D DIC can measure deformations in the out-of-plane direction. Hence any new optical metrology tool or improvisation of an existing tool to perform such quantification by utilizing advances in technology will enhance the capability of design engineers and mechanics researchers alike.

Full-field optical techniques can be broadly classified into white light methods such as moiré/grid techniques, photoelasticity, and digital image correlation and coherent light methods such as holographic interferometry, laser speckle photography, shearography, to name a few. All

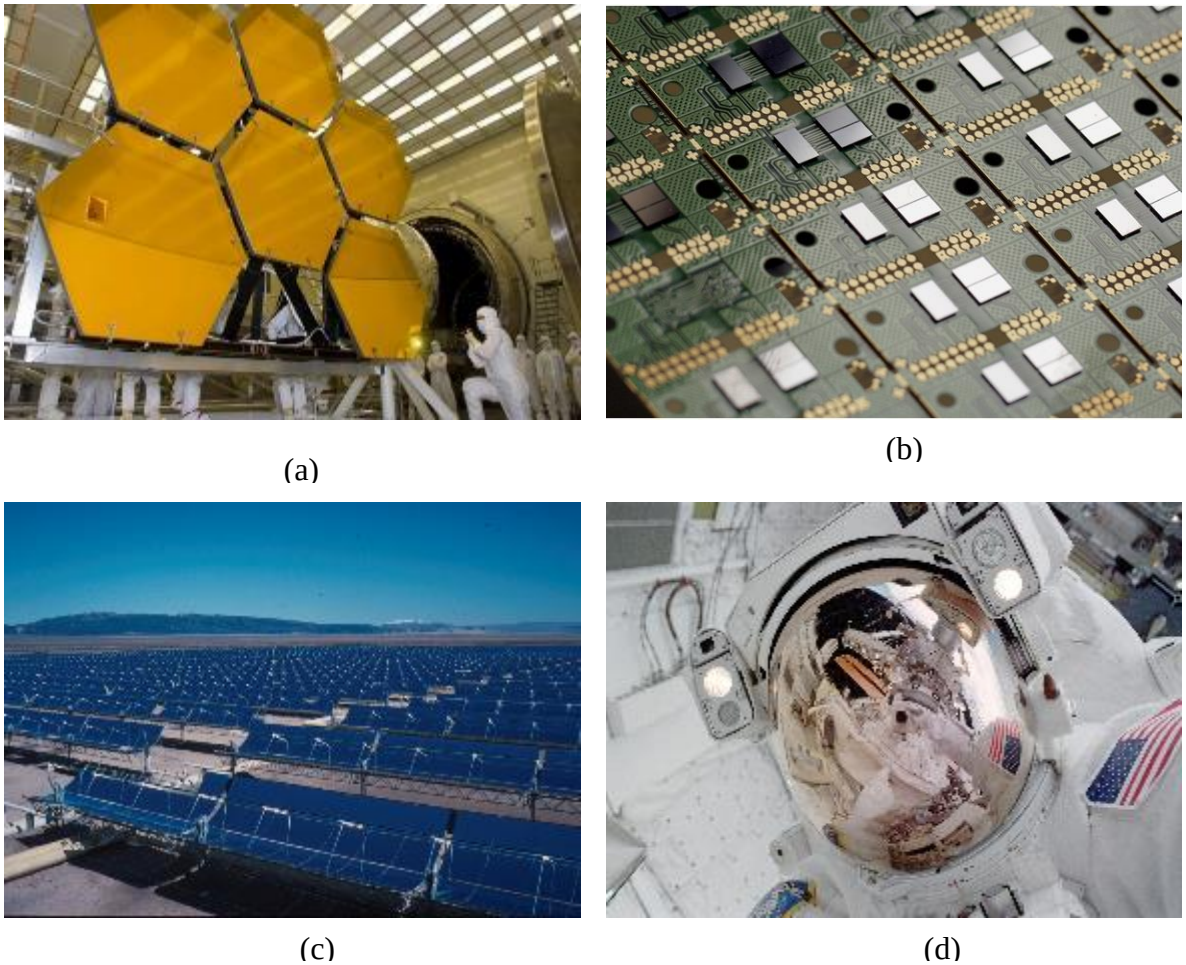

(a) (b)

(c) (d)

Figure 1.1: Examples of reflective engineering structures. (a) Mirrors used in space telescopes (http://www.nasa.gov/centers/marshall/news/news/releases/2011/11-102.html), (b) Silicon wafer die used in flip- chip assemblies (http://www.izm.fraunhofer.de/de/abteilungen/high_density_interconnectwaferlevelpackaging/arbeitsgebiete/Interconnects/projekte/jemsip-3d.html), (c) Solar panels used in solar plant (http://upload.wikimedia.org/wikipedia/commons/6/63/Solar_Plant_kl.jpg), (d) Astronaut helmet (http://www.astrolab.be/educatief/fotos/NASA/Space).

these optical techniques use light as the sensing signal, since light rays have the capability to act as the information carrier without contacting the specimen.

Motivated by these, this thesis deals with extending a full-filed optical technique called reflection-mode Digital Gradient Sensor (r-DGS) capable of measuring surface slopes of specularly reflective objects subjected to quasi-static and dynamic stress fields. The r-DGS technique utilizes 2D digital image correlation method to quantify the surface slopes. A brief survey of some of the existing full-field optical techniques for slope measurement is presented next.

1.2 Moiré methods

The moiré phenomenon can be used to measure in-plane as well as out-of-plane deformations. Moiré fringes are formed when a periodic geometric pattern such as linear gratings or dot pattern with a known periodicity is superimposed on an identical or a nearly identical pattern. The changes in the periodicity or orientation of the latter could be due to thermo-mechanical deformations.

Moiré method to measure in-plane displacements on planar surfaces involves the process of creating geometric patterns on the specimen surface either by affixing gratings or printing the same using microlithography. The shadow moiré technique which measures out-of-plane displacements, on the other hand, does not require geometric patterns to be affixed on the specimen. Instead, here geometric interference occurs when reference grating pattern and its shadow projected on the surface of the specimen being examined interfere. When the specimen suffers deformation, interference between the two sets of gratings produce moiré fringes with information about the out-of-plane displacement or its topography.

In the literature, there are variants of moiré principle for measuring surface slopes. Lichtenberg[1] showed that reflection moiré method can be used for measuring slopes of a

reflective face of a specimen. Reider and Ritter[2] have shown that Lichtenberg's reflection moiré method can be modified to capture slopes in real-time during transient events. Chiang[3] extended the method to dynamic bending problems and also eliminated the need for double exposure with the use of a reference mirror. The experimental setup for vibration studies of a plate by Chiang[4] is as shown in the Figure 1.2.

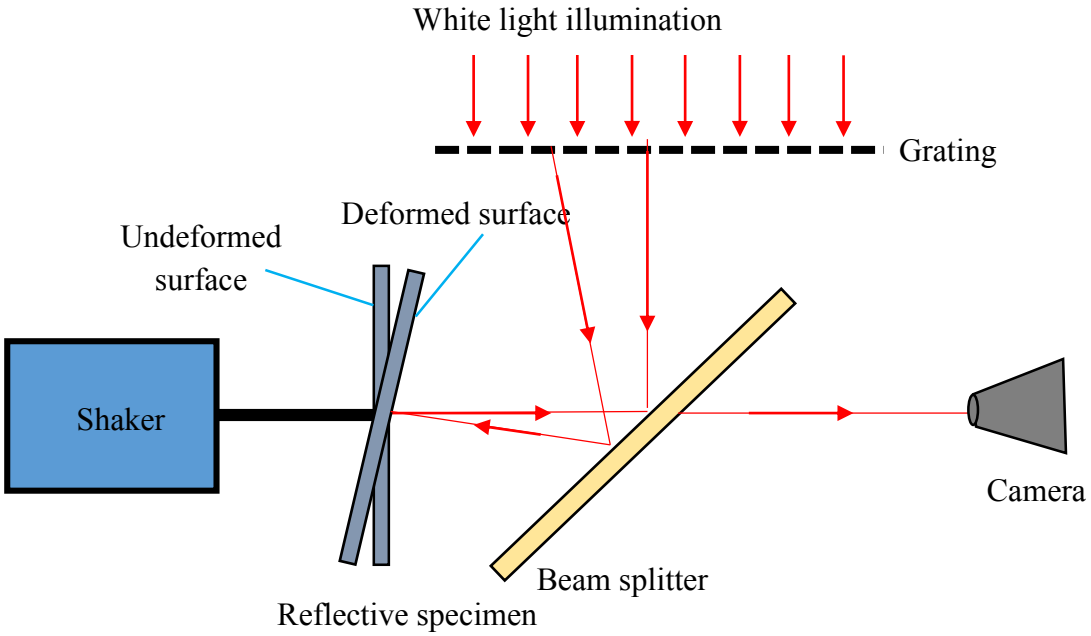

Figure 1.2: Experimental setup for vibration analysis of plates[4]

The experimental arrangement shown in Figure 1.2 consists of a diffused light source to illuminate a linear grating whose virtual image is formed by the specularly reflective surface of the plate being studied and in turn captured by the recording camera. When the object undergoes deformation the distorted grating seen on the object surface can be used to obtain surface slopes. By superposing these two grating images, contours of derivatives of out-of-plane displacement in the principal direction of the grating is observed. When two high density cross gratings are used instead of line grating, low contrast and two orthogonal slope fields are produced. Hence in these experiments optical spatial filtering was carried out to separate the two slope fields and remove

the gratings that produced the fringes from images to enhance their appearance. An example of the same is shown in Figure 1.3.

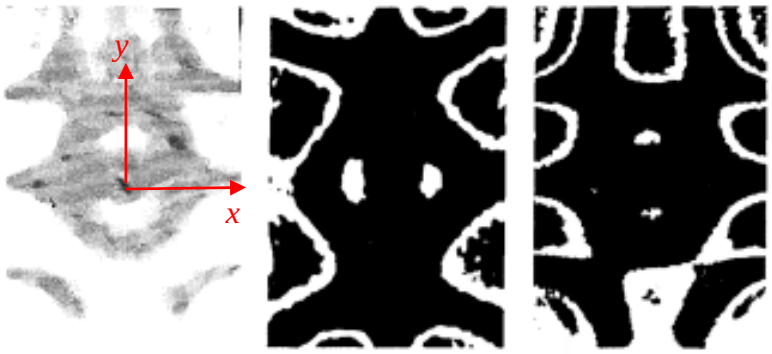

(a) (b) (c)

Figure 1.3: Separation of fringes after optical spatial filtering of a plate vibrating at 1525 Hz (a) Low contrast moiré fringes recorded by camera, after filtering (b) slope fringes along *x*-direction, (c) slope fringes along *y*-direction. (reproduced from Chiang[4])

1.3 Laser speckle photography

When a diffusively reflective specimen is illuminated using a coherent laser light, it appears coated with a granular pattern called laser speckles. This is due to stochastic constructive and destructive interference of wavelets of light bouncing off the "optically rough" sample surface [5]. That is speckles are formed when the mean pitch of the surface feature is greater than the wavelength of the coherent light used to illuminate the surface. For slope measurement, the speckles are photographed on a plane parallel to the object, before and after deformation via double exposure on a film to generate a 'specklegram'. The specklegram is then subjected to optical spatial filtering (using Fourier transform properties of a convex lens) to yield slope contours. One of the advantages of this method is rough/diffuse surfaces can be used without the limitation of a surface to be specular. Chiang[6] has used this method to measure surface slopes of a clamped plate

subjected to central deflection. The schematic of the optical arrangement to measure surface slopes is as shown in the Figure 1.4 and an example of measured surface slope contours in Figure 1.5.

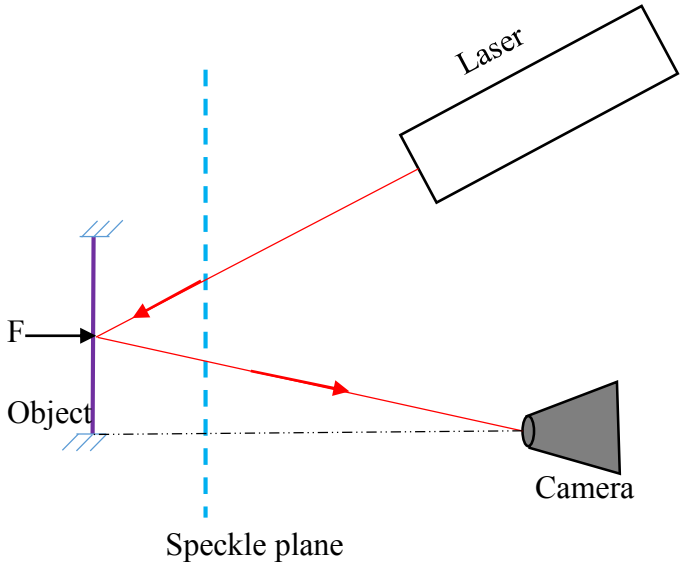

Figure 1.4: Schematic for the experimental setup for laser speckle photography.

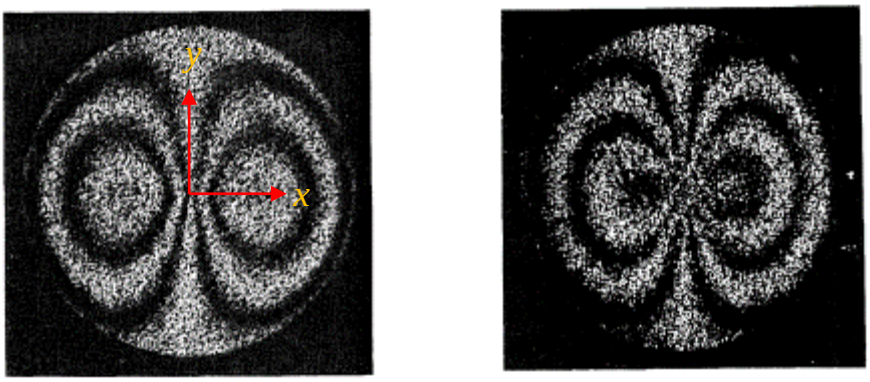

Figure 1.5: Surface slopes for circular clamped plate. PMMA material (left) and cardboard (right). (Reproduced from Chiang[6])

A variation of the above method for recording laser speckles immediately adjacent to the sample surface is used to track surface deformations. The technique is also a double exposure method where the speckle fields recorded before and after deformation of the sample are superimposed to obtain full-field in-plane deformations. Again this is done using optical spatial

filtering of superposed speckle fields recorded on a specklegram. Pointwise filtering of superposed specklegrams results in the so-called Young's fringes whereas full-field isothetic fringes representing contours of constant orthogonal displacements can be obtained using whole-field filtering.

Chiang [7] proposed a modification to the original method to create a specklegram using single exposure. A single exposure specklegram obtained in real-time via a holographically created reference speckle field was proposed. Their experimental setup is shown in Figure 1.6. The setup is similar to a conventional off-axis holographic system with a modification consisting of a half-wave ($\lambda/2$) plate in the optical path of the reference beam and a polarizer in front of the object surface. A single-exposure hologram of the object surface serves as the reference speckle field. The hologram after processing is placed back in its original position and illuminated by the reference beam. When the object is loaded real-time fringes appear due to interference of the two specklefields. This can be further processed using Fourier filtering to obtain deformation fields.

Another variation of laser speckle interferometry called electronic laser speckle interferometry has been used for studying slopes and out-of-plane displacement[8] and also strain distribution in ply wood[9].

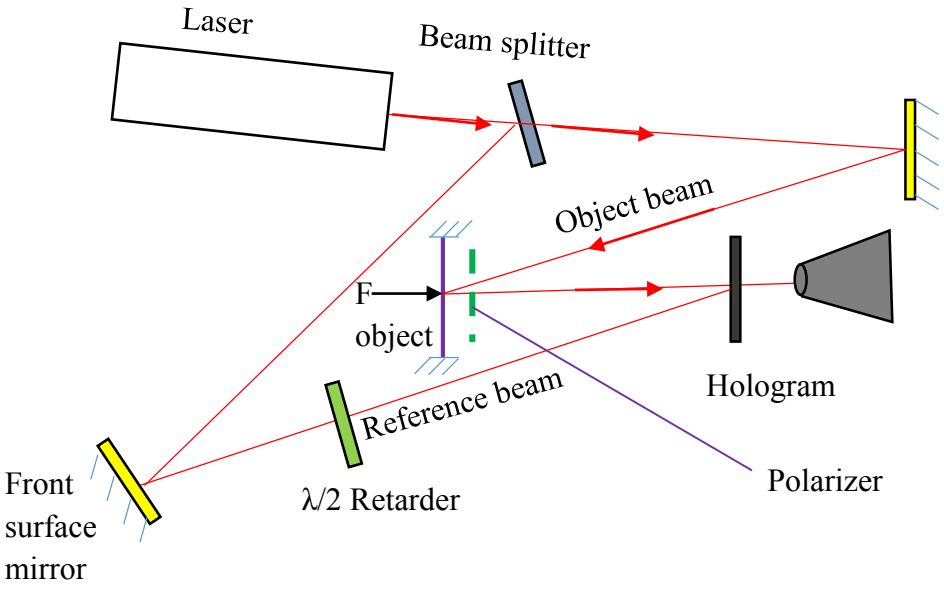

Figure 1.6: Schematic for real-time laser speckle photography[7].

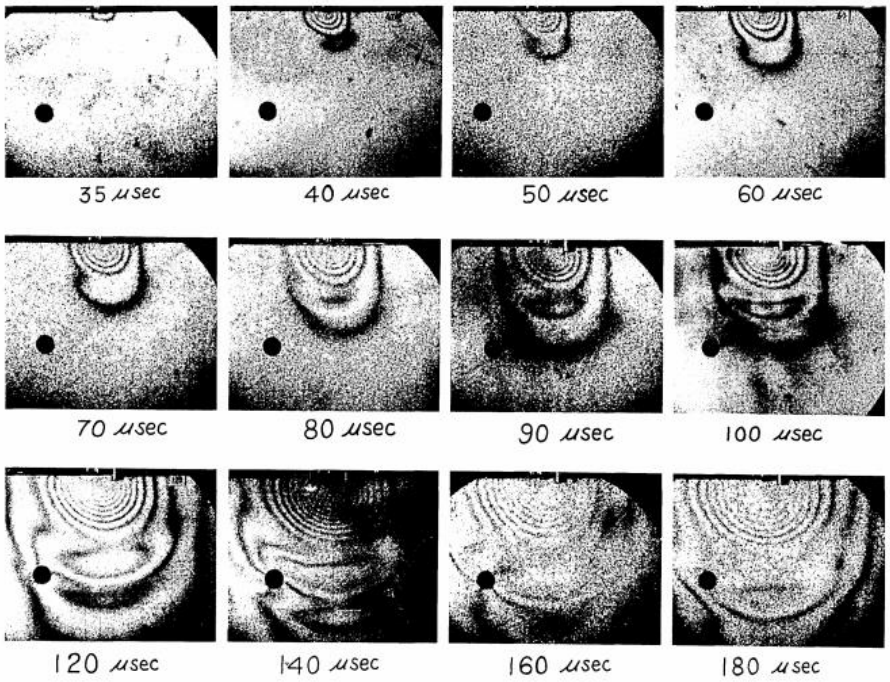

Figure 1.7: Isothetic fringes showing vertical displacement due to stress wave propagation in PMMA plate due to dynamic loading in the direction of impact. (Reproduced from [10]).

1.4 White light speckles

The technique based on white light speckles evolved from the laser speckle photography method and has the same governing equations. The surface of the object is covered with a retroreflective paint. This paint consists of small glass spheres embedded in an emulsion. The surface is then illuminated using white light and speckles are recorded on the recording device placed at the image plane. The working principle of white light speckle photography is same as the one for laser speckle photography. The main difference between these two methods is that the speckles are fixed on the specimen surface in white light speckle photography whereas they fill the space in front of the specimen for the latter. The experimental setup to utilize white light speckle photography is as shown in the Figure 1.8.

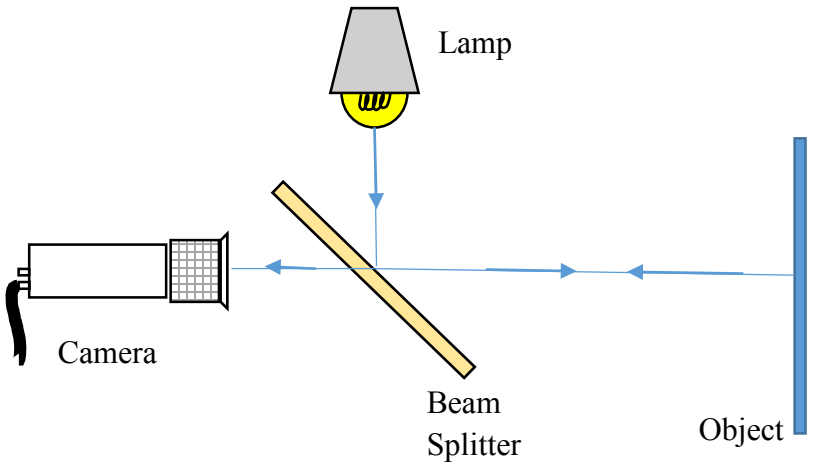

Figure 1.8: Schematic of the experimental setup for white-light speckle photography.

For displacement and strain measurement, a double exposure of the object is recorded before and after deformation. The resulting specklegram is then optically processed using whole-field or point-wise techniques to obtain displacement fringes.

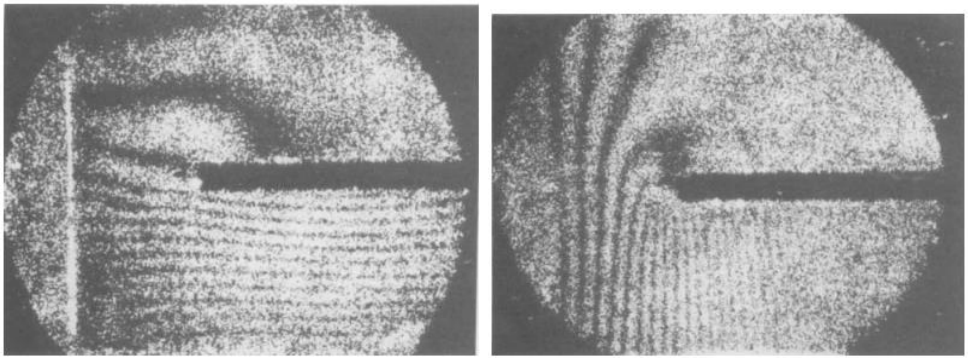

Figure 1.9: Notched PMMA under tension. Vertical displacement (left) and horizontal displacement (right). (Reproduced from[1]).

The dynamic applications of this method has been demonstrated by Chen[11, 12], and recently Chiang[13] has shown its application in micro/nanotechnology.

1.5 Grating techniques

Kao[14] introduced a family of grating techniques to measure slopes and curvatures of plates. The schematic of the experimental setup is as shown in Figure 1.10. It consists of a light source which is used to illuminate the surface of a reflective object. The field lens collects the reflected light rays from the object and an image is formed at the image plane. Gratings are erected in the light path for slope measurements. The gratings act as a filter by blocking the light rays from the object falling on the opaque lines and allowing only the light rays passing through the transparent spacings between the lines. The opaque lines of the gratings block the rays reflected from the reflective surface which results in the formation of shadow. This results in the formation of a shadowgram. When the object undergoes deformation, the diffracted light rays from the gratings result in interference pattern which can be interpreted as moiré pattern of different

[1] Optical Metrology. Kjell J. Gasvik

diffraction orders. By positioning the grating at a particular position and using double exposure technique, the shadowgram obtained will carry the slope information of the plate surface.

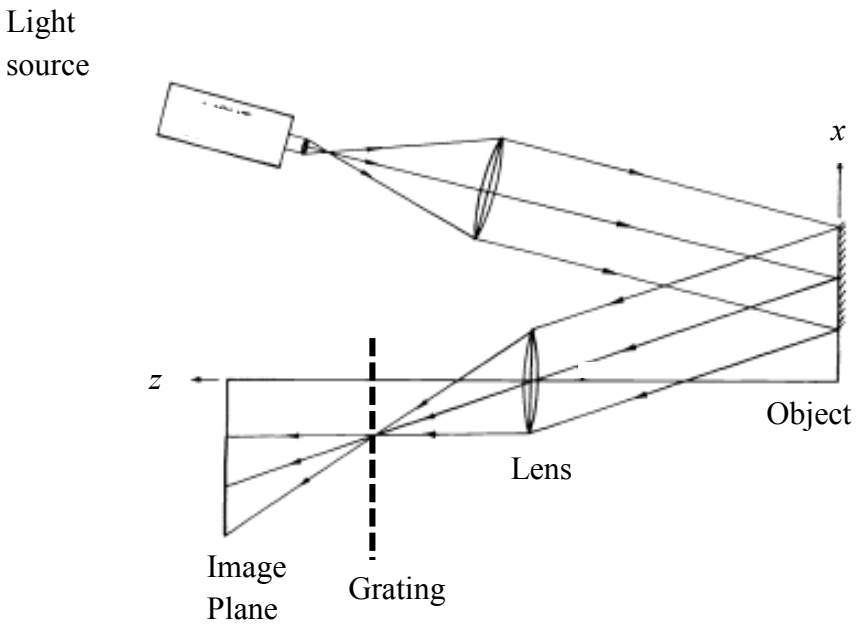

Figure 1.10: Schematic of the experimental setup to measure slope. Grating at the focal plane. (Reproduced from [14]).

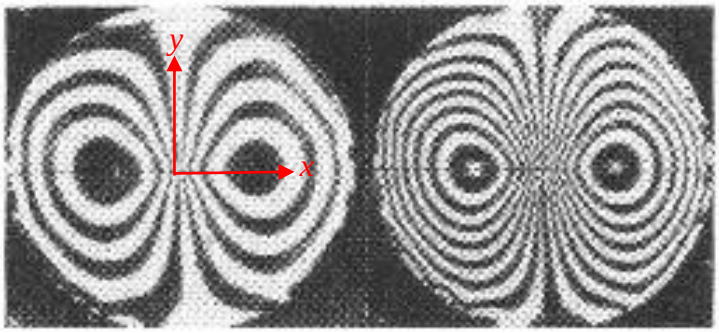

Figure 1.11: Slope contours for a circularly clamped PMMA plate for an applied central deflection of 0.0075 in. Grating of 10 lpi (left) and 20 lpi (right) was used. (Reproduced from [14]).

Kao[14] also showed that this method can be successfully used in mapping stress wave induced deformation in plates. Subramanian[15, 16] has shown that selective spatial filtering of the diffraction wave-fronts from the gratings can be used to obtain real-time slopes and curvatures.

1.6 Shearography

Shearography is a full-field coherent optical method for non-destructive evaluation and strain measurement.

The schematic of the experimental setup is as shown in the Figure 1.12. An expanded beam of laser beam is used to illuminate the object. A CCD camera is used to capture the speckle field reflected from the surface of the object. A device placed in front of the camera is used to accomplish the spatial shearing (lateral shifting) of laser speckles. The shearing device generates two laterally shifted images of the object which interfere with each other resulting in an interference pattern. Comparison of speckle patterns recorded before and after deformation of the object yields fringe pattern representing derivatives of surface deformations.

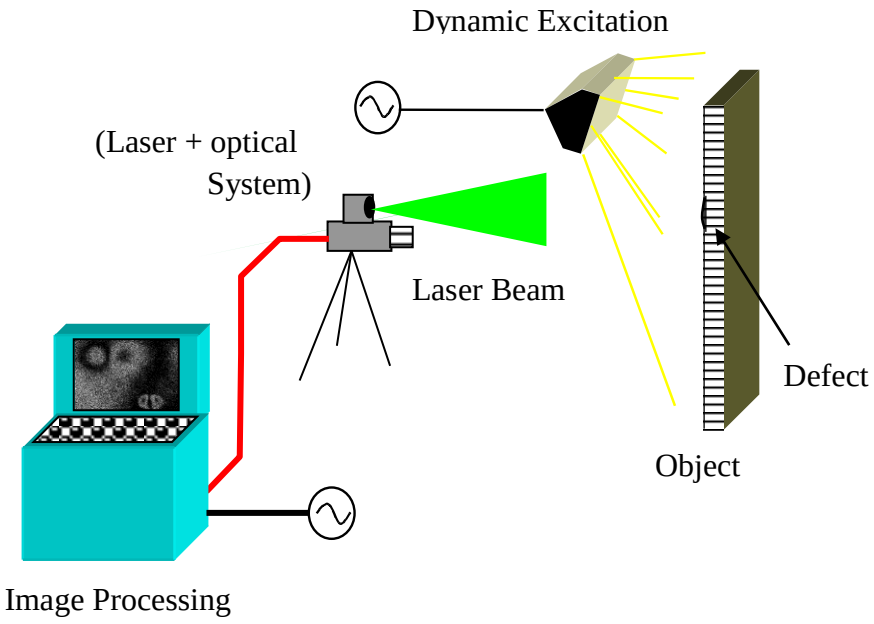

Figure 1.12: Schematic of the experimental setup to perform shearography. (Reproduced from [2]).

[2] http://www.testia.com/documents/5-Shearography

(a) (b)

Figure 1.13: (a) MIRA pressure vessel Filamentary wounded (Al-GFRP). (b) Delamination in the vessel due to high pressure. (Reproduced from[3]).

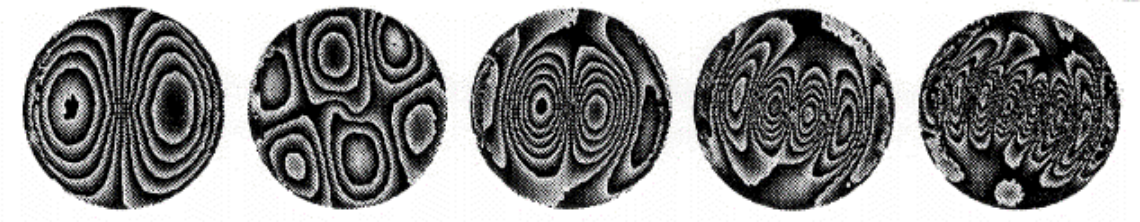

Figure 1.14: Shearograms showing surface slopes of a thin circular plate clamped all around and subjected to harmonic excitation at frequencies of 1270 Hz, 4300 Hz, 4860 Hz, 10900 Hz and 18960 Hz (left to right, from Universitat Gesamthochschule Kassel, Ing and Steinchen)

Shearography was first implemented by Hung[17] as a strain measurement and as NDE tool by Lee[18] and Toh[19].

1.7 Coherent gradient sensing (CGS)

CGS is a real-time interferometric technique that measures angular deflections of light rays. Tippur and Rosakis[20, 21] introduced this full-field optical technique that produced angular deflection of light rays due to changes in the refractive index (transmission CGS) and surface slopes due to thickness changes (reflection CGS) due to mechanical loads acting on transparent and reflective specimens, respectively.

[3] http://www.testia.com/documents/5-Shearography

The experimental setup for CGS, shown in Figure 1.15, in reflection-mode involves a specularly reflective object, two Ronchi gratings of identical pitch having principal directions parallel to each other, a beam splitter and a recording device. The two gratings are separated by a known distance along the optical axis. A collimated beam of light is first passed through the beam splitter and then incident on the specimen surface. Optical spatial filtering is also an integral part of the apparatus. The light rays reflected from the specimen surface are split into multiple wave fronts by the first grating and they again undergo diffraction as they pass through the second grating. Optical spatial filtering is carried by a lens that collects the diffracted wave fronts and displays them on the back focal plane as a linear array of spots. By filtering either the +1 or -1 diffraction order, two wave fronts propagating in the same direction but with a spatial shift are brought to focus on the image plane. The optical path difference between them produces interference on the camera plane. The resulting interference fringes represent contours of angular deflections of light rays and surface slopes.

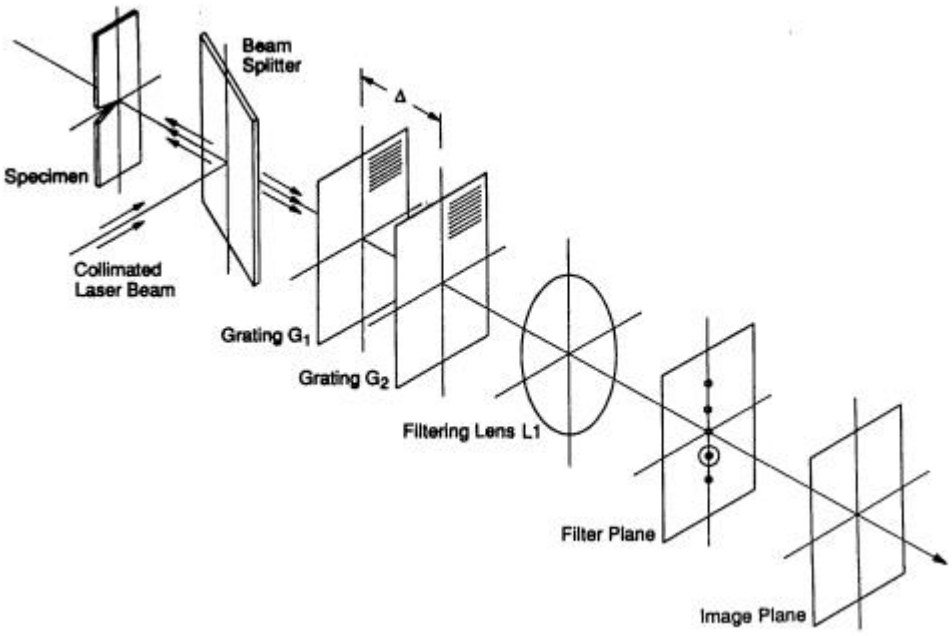

Figure 1.15: Schematic of the experimental setup for reflection CGS.(Reproduced from [21]).

The ability of CGS to measure surface slopes made it an effective tool for deformation measurements[22] and also to study fracture mechanics[23, 24] problems. CGS fringes of surface gradients along the crack direction in a AISI 4340 steel sheet subjected to mode-I loading is shown in Figure 1.16. Fracture parameters were extracted by analyzing these fringes in conjunction with crack tip field descriptions. CGS in reflection mode has been employed to study fracture behavior of a variety of novel materials including functionally graded materials by Rousseau[25, 26] and Kirugulige[23]. Liu[27] employed CGS to study fracture behavior of composites.

Reflection CGS has also been used to measure deformations of thin structures and films. For example, fringes for a thin circular silicon wafer clamped at the edges and subjected to central deflection is shown in Figure 1.17. Behavior of thin film substrates has been studied by Lee[18, 28] and Park[29] using CGS.

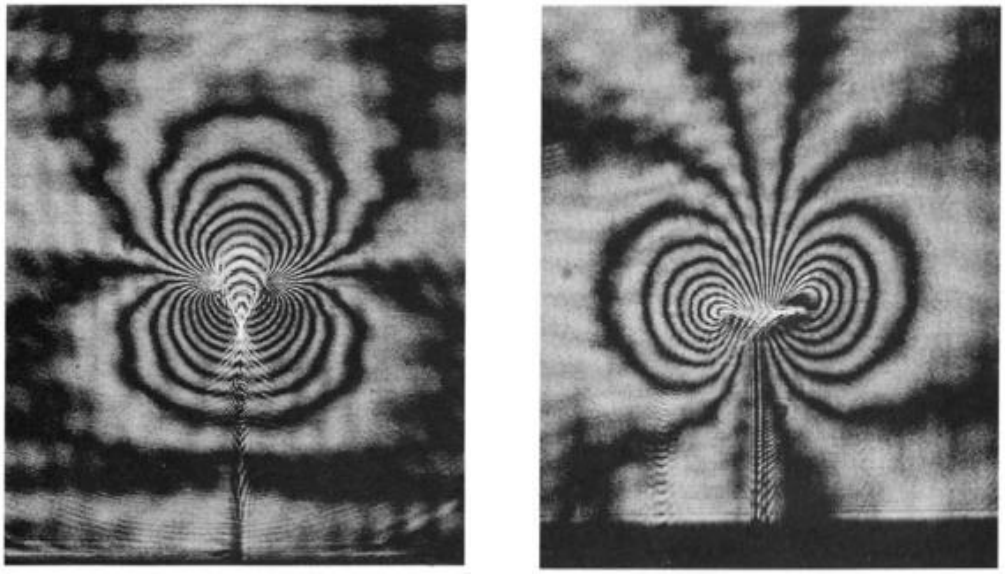

(a) (b)

Figure 1.16 : Surface gradient fringes from Reflection CGS along the loading direction (a) and perpendicular to the loading direction (b) for AISI 4340 steel. (Reproduced from[30]).

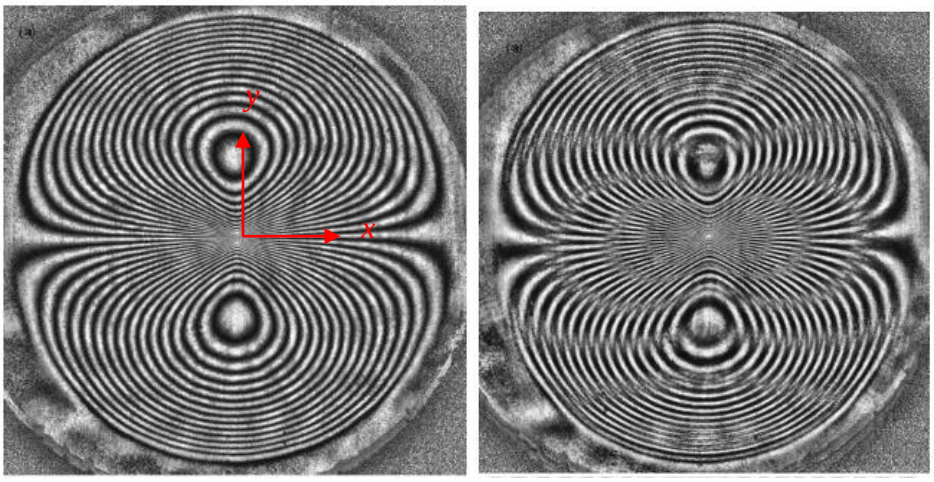

(a) (b)

Figure 1.17: Thin silicon wafer clamped at the edges and subjected to a central out-of-plane displacement of 80 μm. (a) slope fringes (b) curvature fringes. (Reproduced from [22]).

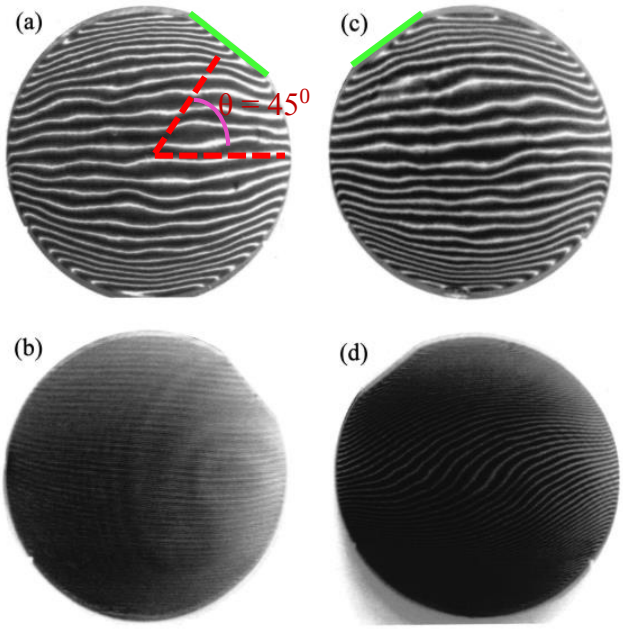

Figure 1.18: CGS fringe pattern for Aluminum deposited on silicon substrate subjected to thermal excitation. Temperature change (a) and (c) 7.5^0C and (b) and (d) 52.5^0C. Different sample orientation ($\theta = 45^0$(a) and (b), $\theta = 135^0$(c) and (d)). (Reproduced from[28]).

1.8 Objectives

The primary objective of this thesis is to extend r-DGS method as a small deformation measurement tool for studying specularly reflective solids subjected to non-uniform quasi-static and dynamic stress fields. The following are the major items addressed during this research:

- Develop a viable experimental apparatus to carry out surface slope measurements using r-DGS. Establish the relationship between angular deflections measured and the surface slopes.
- Conduct baseline quasi-static experiments to measure surface gradients in thin plates subjected to central out-of-plane deflection. Use measured slope fields to obtain curvatures and topography by differentiating and integrating them, respectively.
- Examine the effect of different experimental parameters such as sub-image size, sub-image overlap, effect of different speckle size, effect of target distance, on measurements.
- Develop an experimental setup to study stress wave propagation in plates due to projectile impact using r-DGS in conjunction with high-speed photography. Using the setup make time-resolved surface gradient measurements during wave propagation and deduce curvatures and topography.
- Demonstrate the feasibility of r-DGS in disbond and damage detection in layered plates. Extend the method to detect delamination caused by mechanical impact on composite plates. Also demonstrate the feasibility of r-DGS to measure deformation due to thermo-mechanical stresses in flip-chip assembles.
- Demonstrate the feasibility of r-DGS to study fracture mechanics problems under both static and dynamic loading conditions. Perform fracture experiments for both mode-I

and mixed-mode (mode I + mode II) loading conditions to measure deformations near stationary as well as growing cracks. Use the corresponding crack-tip field equations to extract stress intensity factors and their histories.

Chapter 2 : Reflection-Mode Digital Gradient Sensing (r-DGS): Working Principle

This chapter deals with the working principle of reflection-mode digital gradient sensor (r-DGS) and its experimental setup for implementation. The experimental setup is discussed in detail first and then a ray tracing analysis is provided next to explain the changes to the optical path of the light due to surface deformation. The optical measurements are then linked to the mechanical fields[31].

2.1 Experimental setup

The schematic of the experimental setup for implementing reflection-mode DGS method to measure surface slopes of a planar reflective object is shown in the Figure 2.1. The setup consists of a digital imaging device, a 50/50 beam splitter, a planar thin reflective specimen and a planar speckle target. The target plate is coated with alternate mists of black and white paints to create random speckles. The target plate is illuminated with the help of two LED light sources (not shown in the schematic). The digital camera fitted with a long focal length lens and an extension tube is focused on the target plane via the reflective surface of the specimen and through the beam splitter. The beam splitter placed in a stage is oriented at an angle of 45^{o} to the optical axis of the camera. The camera settings are chosen such that a good depth of field to keep speckles on the target in focus is achieved with a small aperture opening.

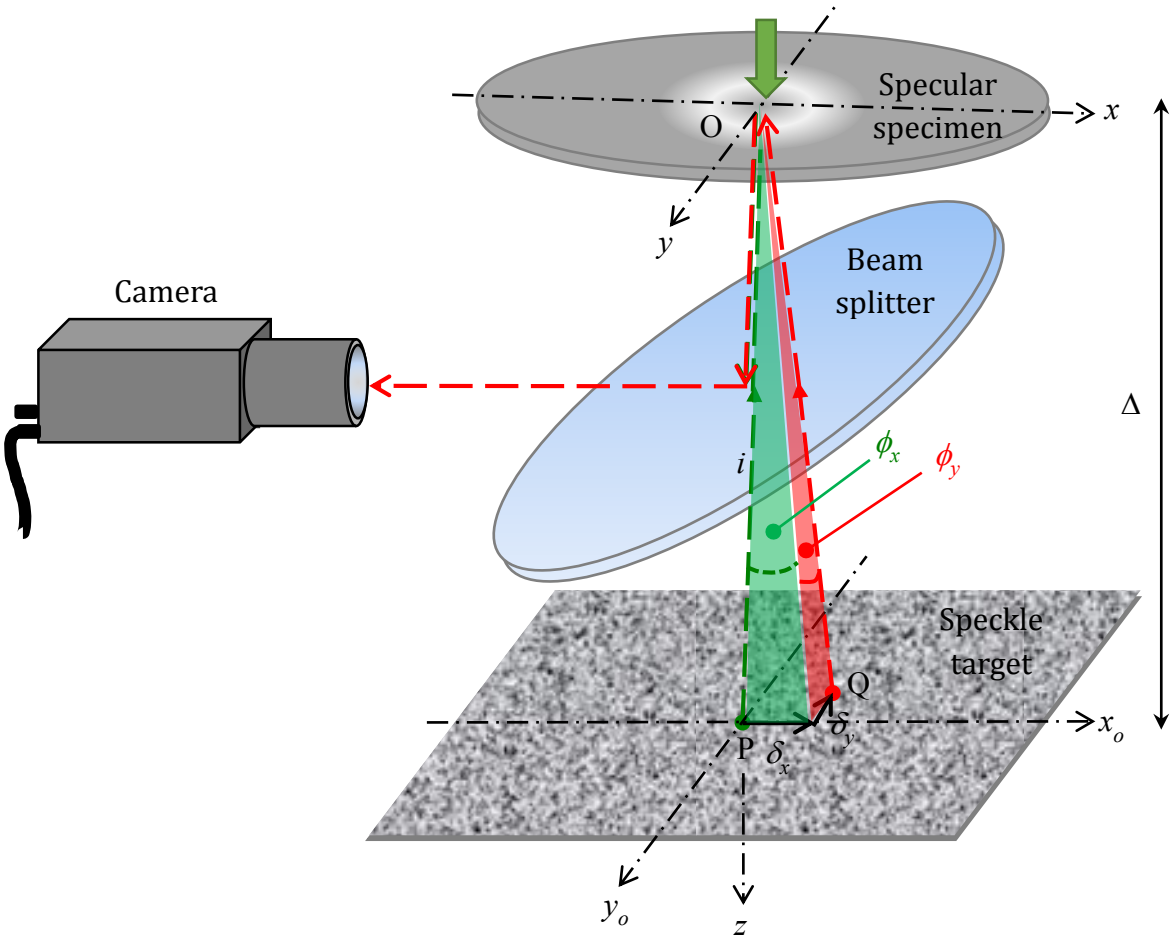

Figure 2.1: Schematic depicting the experimental setup for reflection-mode DGS (r-DGS) methodology.

2.2 Working principle

Figure 2.2 shows the optical path traced by the light ray between the specimen and the target plate (without the beam splitter for simplicity) in an r-DGS experimental setup. Let (x,y) be the specimen surface coordinate system while (x_o,y_o) the target plane coordinate system. Also let n and t be the unit normal and unit tangent to the specimen surface and θ_i denote angle of incidence and θ_r angle of reflection. Initially a point P is focused through point O on the specimen by the camera. At this state the specimen surface is flat and undeformed. In this condition, the incident ray i and

the reflected ray *r* are collinear to each other. When the specimen surface undergoes deformation *w* in the *z* direction (out-of-plane), point O moves to O *'* due to which point Q on the target surface is captured by the camera. The incident ray OP is deflected to O *'*Q by an angle $\phi_y (= \theta_i + \theta_r;\ \theta_i = \theta_r)$. By digital image correlation technique the displacement δ_y (δ_x in orthogonal direction) can be measured in the whole field of observation. The local surface slopes component in, say, the *x*-*z* and *y*-*z* planes can be evaluated as[31],

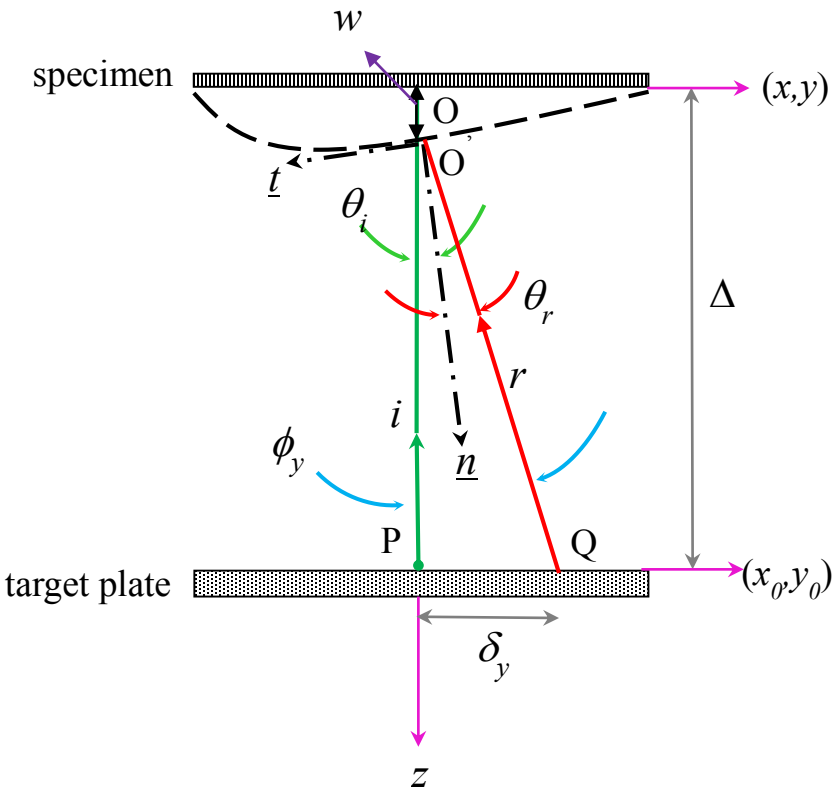

Figure 2.2: Planar representation of optical path in r-DGS setup (without beam splitter).

$$\frac{\partial w}{\partial x : y} = \frac{1}{2}\tan\left(\phi_{x:y}\right) = \frac{1}{2}\left(\frac{\delta_{x:y}}{\Delta}\right). \tag{2.1}$$

For small angular deflections, this can be written as,

$$\frac{\partial w}{\partial x : y} \simeq \frac{1}{2}\phi_{x:y} \simeq \frac{1}{2}\frac{\delta_{x:y}}{\Delta} \tag{2.2}$$

where $\phi_{x;y}$ represent angular deflections of light rays. Here Δ denotes the distance between the specimen and target planes and is the *optical lever* that controls the sensitivity of the method in addition to those associated with 2D digital image correlation such as the sub-image size, pixel overlap and the searching algorithm used.

2.3 2D Digital image correlation

For the evaluation of the displacement components δ_x and δ_y, r-DGS relies on 2D digital image correlation (DIC) principles. DIC process involves correlation of the images of the specimen surface covered with a stochastic pattern (also called a random speckle pattern) captured by a digital camera before and after deformation. The speckle pattern recorded under no-load conditions serves as the reference image. The speckle pattern on the object is perturbed due to the application of load which is captured as the deformed image. These images contain information of the gray scale distribution on the specimen surface in a discrete form at each pixel location.

Figure 2.3 shows the working principle of DIC. As shown in Figure 2.3(a) the undeformed image of 1000 x 1000 pixels is segmented into an array of rectangular sub-images with each sub-image of size 20 x 20 pixels. While correlating it with the deformed image, for every sub-image in the undeformed image, the corresponding sub-image (intensity distribution) is searched in the deformed image by performing grayscale correlation operation. For simplicity of understanding, Figure 2.3(b) shows the planar deformation of an isolated sub-image. Due to the application of external load, sub-image in the undeformed state centered at $O(x,y)$ is displaced to $O'(x+u, y+v)$ by distances u and v in the x- and y- directions, respectively. The displacement components u and

v can be obtained by affine coordinate transformation. The displacement components *u* and *v* corresponds to δ_x and δ_y respectively which aids in quantification of surface gradients using r-DGS as described in Equation 2.2.

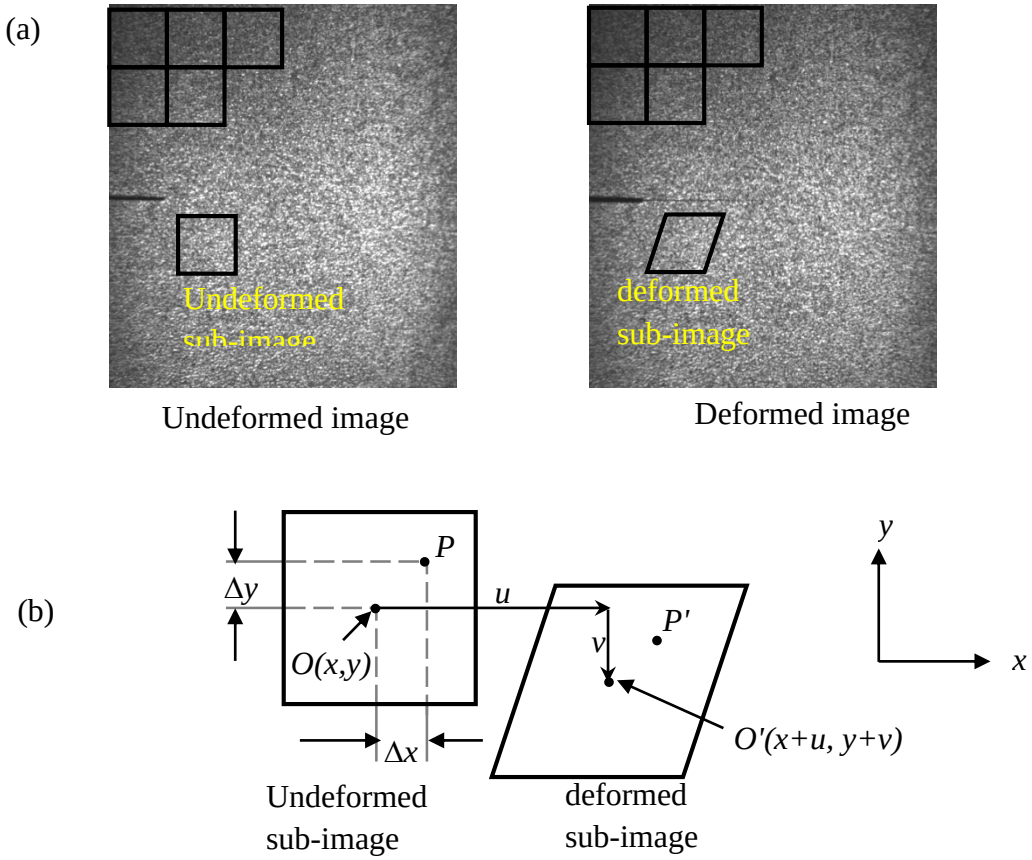

Figure 2.3: Working principle of 2D DIC. (a) Undeformed and deformed speckle images segmented into sub-images, (b) Sub-image displacement mapping scheme. (Reproduced from [32]).

Chapter 3 : Measurement of Surface Slopes in Thin Plates

Thin reflective engineering structures such as space mirrors, microelectronic devices, photovoltaic devices, to name a few often fail when subjected to mechanical stresses. Hence quantification of deflections, slopes and curvatures under static and dynamic loading conditions is critical. Non-contacting methods to perform such measurements at relatively high sensitivities are important when small deflections are to be detected and quantified in stiff structures and materials. It should also be noted that mechanical stresses in thin structures are proportional to curvatures which in turn are the first and second derivatives of slopes and deflections. As numerical differentiation of measured data is often prone to considerable errors, direct measurement of surface slopes instead of topography is preferred for evaluating curvatures.

In the following, experimental details for measuring orthogonal surface slopes for a circular silicon wafer clamped at the edge and subjected to a central deflection are explained. The measured surface slopes are compared with the theoretical counterparts. Subsequently, the measured slopes are differentiated to obtain curvatures and integrated to obtain surface topography. The processed results are compared with the theoretical counterparts as well. The DGS method in the reflection-mode is then extended to visualize the evolution of surface slopes due to impact loading of a free-free thin sheet by a stiff spherical impactor. Surface topographies obtained by impact loading are compared with numerically simulated counterparts.

3.1 Experimental details

The schematic of the setup to measure surface slopes of reflective planar specimens using the r-DGS method is shown in Figure 3.1. It consists of an imaging device (Nikon D3100 digital SLR camera), a beam splitter and a planar speckle target. The camera was fitted with an extension tube and a 70-300 mm lens. The beam splitter is placed in between the specimen and the target, and is oriented at 45^0 degrees to the optical axis of the camera. The camera is now focused on the target plane via the reflective surface of the specimen and through the beam splitter. A 280 μm thick, single face polished silicon wafer of 50.8 mm diameter was used in this demonstration. The unpolished face of the silicon wafer is glued to the steel washer using an epoxy adhesive. The inner and outer diameters of the washer are 25.7 mm and 76.2 mm, respectively. A central displacement was applied to the silicon wafer using a micrometer firmly mounted on a steel plate with circular aperture placed behind the silicon wafer inside a cylindrical holder. The speckles on the target plate were recorded with the help of the beam splitter. The target plane was at a distance (Δ) of 65 mm from the reflective surface. The camera was then focused on the target plate via the reflective face of the silicon wafer. The distance between the camera lens plane (L) and the specimen plane was 1200 mm. Under no-load conditions an image was recorded which served as the reference image. Then using the micrometer, central out-of-plane displacements w = 10 μm, 20 μm, 30 μm was imposed on the wafer. Figure 3.2 shows the distortion of the speckles relative to the undeformed counterpart at the central region of the silicon wafer due to an applied 30 μm displacement. Deformed images captured were then correlated with the reference image using ARAMIS, to extract in-plane displacement fields δ_x and δ_y. The image was segmented into 20 x 20 pixels (1pixel covered 39.6 μm on the target plane). Figure 3.3 shows the surface slopes (solid

lines) calculated over the entire circular region for an applied 30 μm displacement. The contour plots are shown in steps of 5 x 10^{-4} rad.

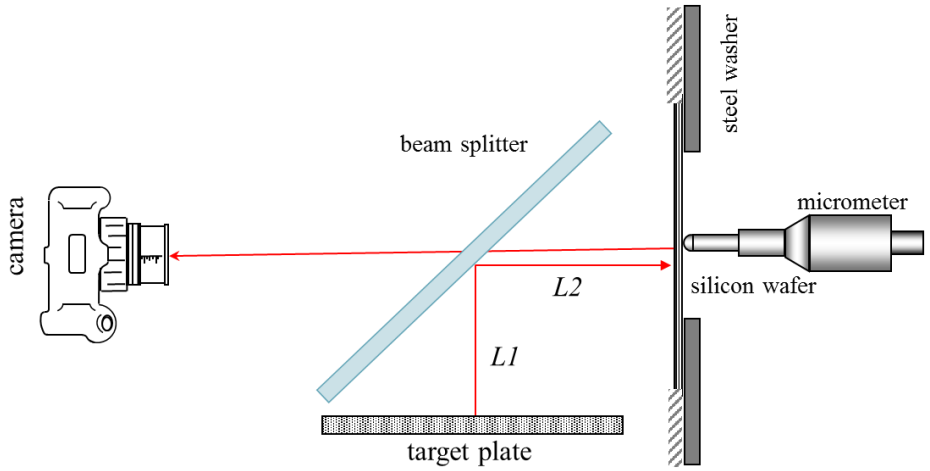

Figure 3.1: Schematic of DGS experimental setup in reflection.

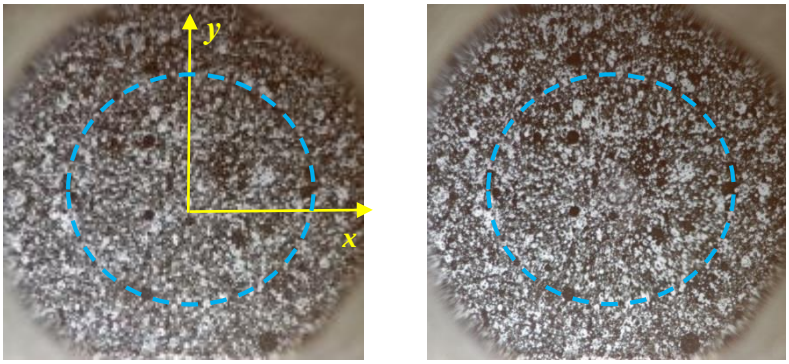

Figure 3.2 Undeformed (left) and deformed (right) images captured off the reflective face of silicon wafer subjected to 30 μm central displacement (inner diameter represented by dotted lines).

The surface slope measurements from reflection-mode DGS were compared with those for a clamped elastic plate subjected to a central deflection by a point force given by [22],

$$\frac{\partial w}{\partial x; y} = \frac{4(x; y)w}{R^2} \log\left(\frac{\sqrt{x^2 + y^2}}{R}\right) \tag{3.1}$$

where w is the out-of-plane displacement and R is the clamped radius of the wafer.

The analytically obtained contours (broken lines) are superimposed on experimentally measured surface slopes in Figure 3.3. Excellent qualitative and quantitative agreement between the two results is self-evident. Figure 3.4 shows the variation of experimentally measured surface slopes superimposed on the analytically obtained surface slope data. A good agreement can be seen from the plot.

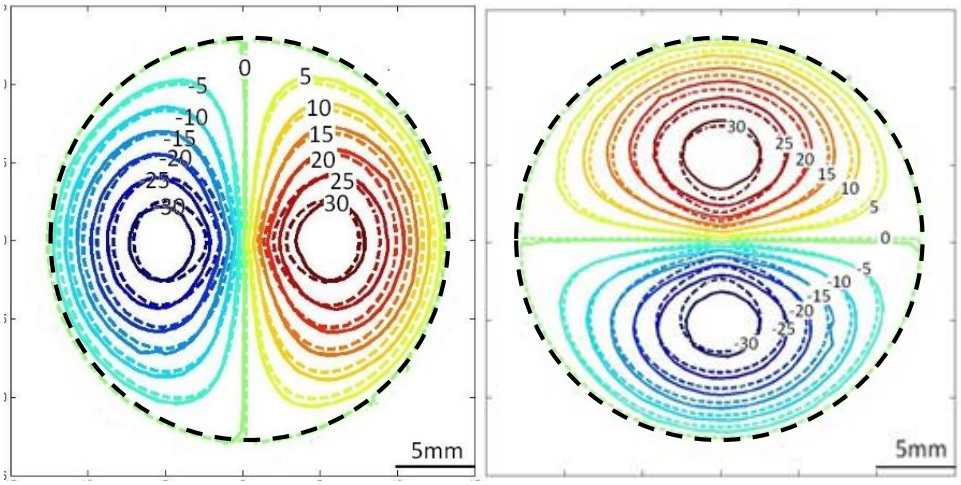

Figure 3.3: Experimental (solid lines) and analytical (broken lines) contours of $\frac{\partial w}{\partial x}$ (left) and $\frac{\partial w}{\partial y}$ (right) comparison for a clamped silicon wafer subjected to 30 μm central displacement. Contour levels are in 1 x 10^{-4} radians.

3.2 Surface curvatures of a silicon wafer subjected to central load

The δ_x and δ_y measurements from reflection-mode DGS were differentiated once with respect to in-plane spatial co-ordinates *x* and *y* to estimate curvatures. Surface slopes $\frac{\partial w}{\partial x}$ and $\frac{\partial w}{\partial y}$ being proportional to δ_x and δ_y, the respective curvatures [33] were calculated as,

$$\frac{\partial^2 w}{\partial x^2; y^2} = \frac{1}{2}\frac{\partial}{\partial x; y}\left(\frac{\delta_{x;y}}{\Delta}\right) \tag{3.2}$$

The contour plots of curvature measurements (solid lines) are shown in Figure 3.5. For comparison, the analytically predicted curvature fields given by [1],

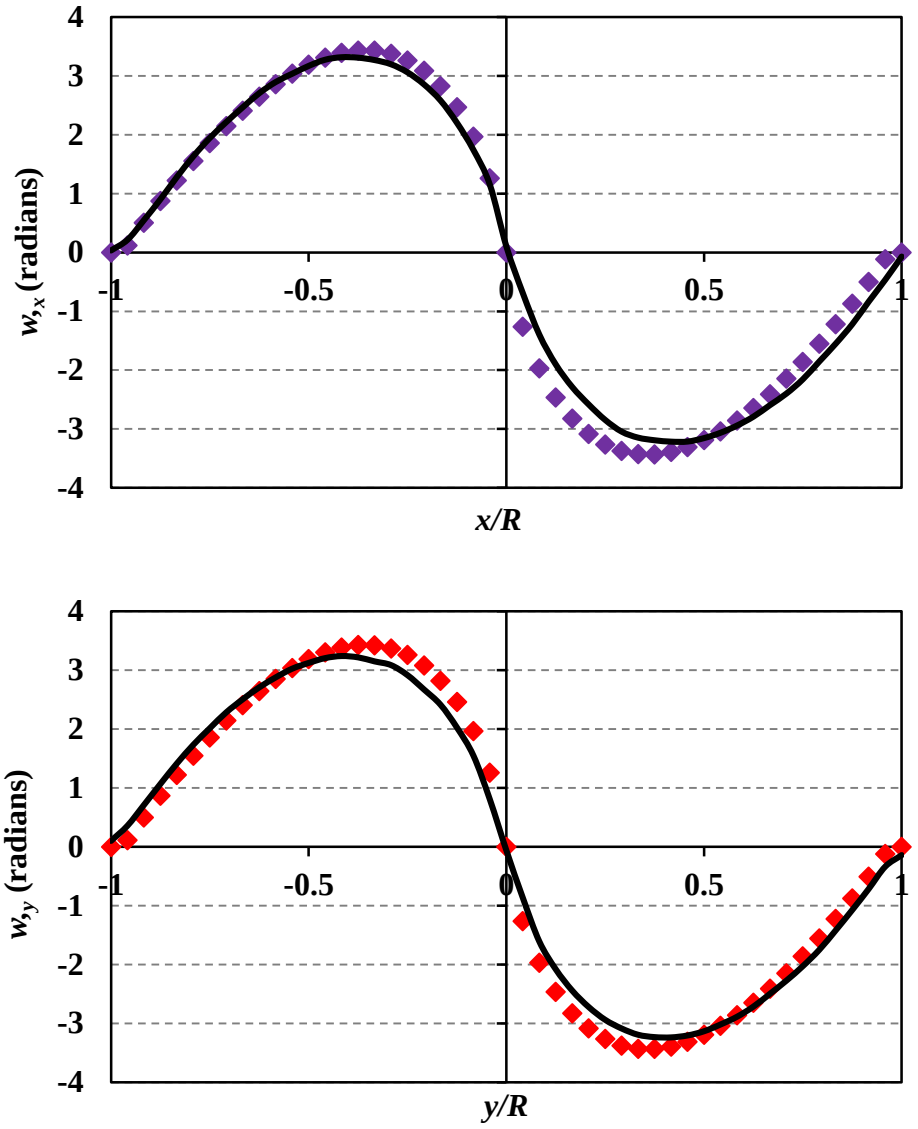

Figure 3.4: Analytical (solid lines) and experimental (symbols) data of $w_{,x} = \frac{\partial w}{\partial x}$ (top) along the x-axis ($x,y=0$) and $w_{,y} = \frac{\partial w}{\partial y}$ (bottom) along the y-axis ($x=0,y$) corresponding to a clamped silicon wafer subjected to a 30 μm central out-of-plane deflection.

$$\frac{\partial^2 w}{\partial x^2; y^2} = \frac{4w}{R^2}\log\left(\frac{\sqrt{x^2+y^2}}{R}\right) + \frac{4(x^2; y^2)w}{R^2(x^2+y^2)} \tag{3.3}$$

are superimposed on the experimental counterparts. The contour plots are shown in steps of 2 x 10^{-4} mm^{-1}. Again, good qualitative and quantitative agreement is evident between experimental and analytical results.

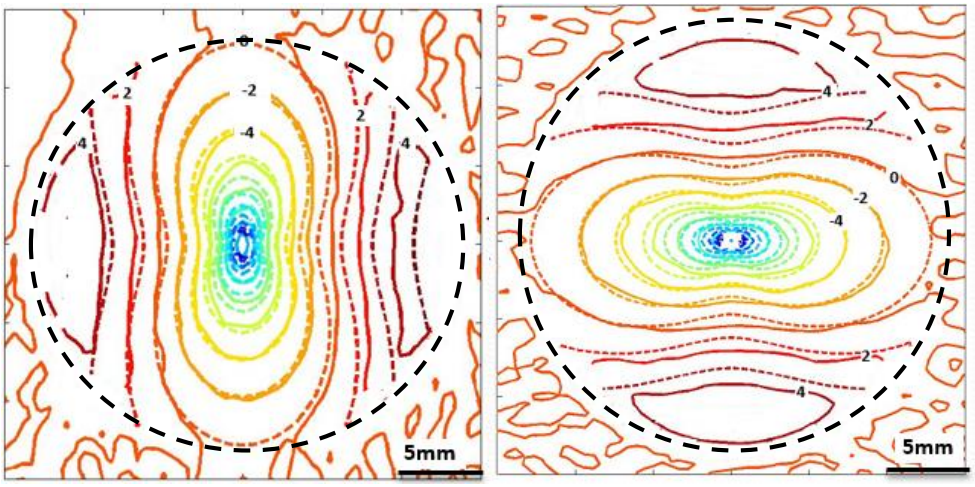

Figure 3.5: Experimental (solid lines) and analytical (broken lines) contours of $\frac{\partial^2 w}{\partial x^2}$ (left) and $\frac{\partial^2 w}{\partial y^2}$ (right) compared for a clamped silicon wafer subjected to 30 μm central displacement. The contour levels are in 1 x 10^{-4} mm^{-1}.

3.3 Surface topography of silicon wafer subjected to central load

In reflection-mode DGS, δ_x and δ_y measurements being proportional to surface slopes, $\frac{\partial w}{\partial x}$ and $\frac{\partial w}{\partial y}$ can be integrated with respect to the in-plane spatial coordinates to estimate topography of the deformed plate. A simple trapezoidal rule of integration was used to obtain the out-of-plane deformations. Integration was carried along both the in-plane directions. The resulting surface topographs are shown in Figure 3.7. The results from integration show a good agreement with the maximum value imposed at the center with the applied displacement.

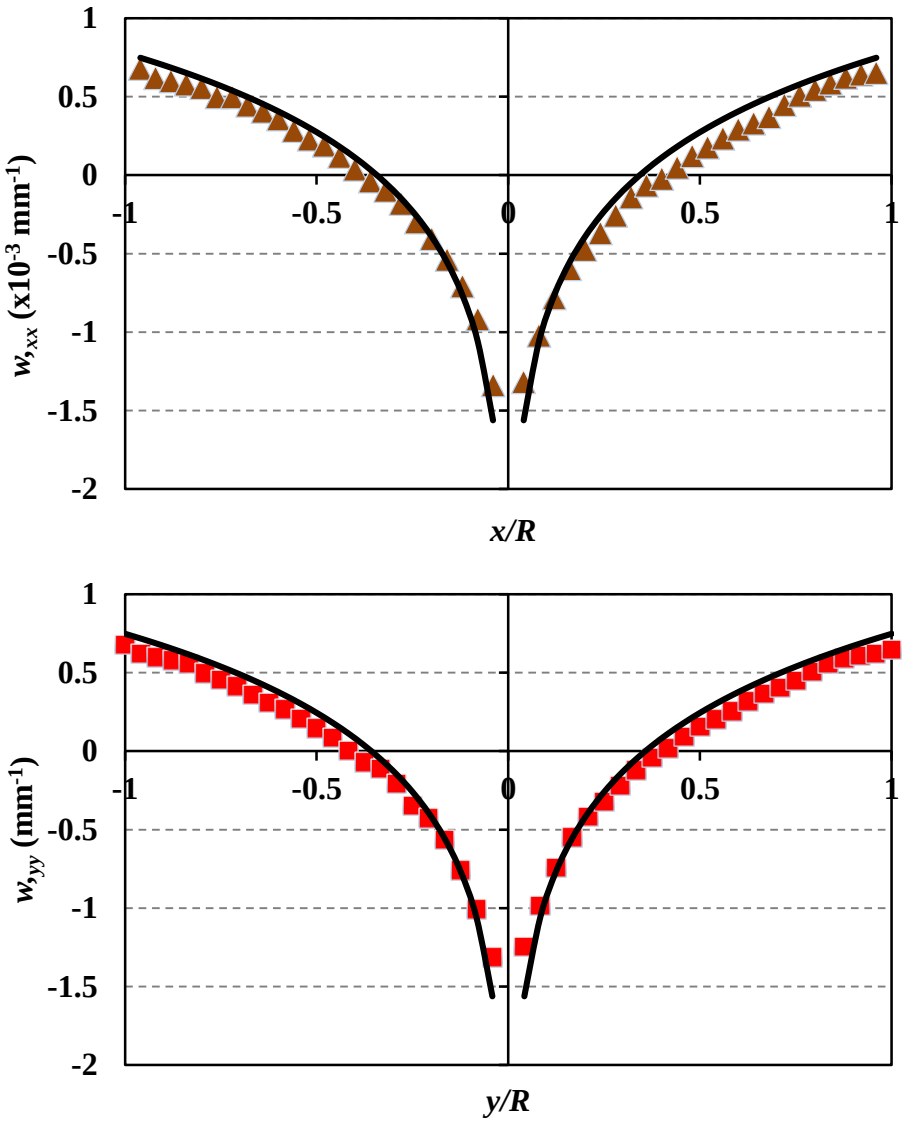

Figure 3.6: Variation of $w_{,xx}$ (top) and $w_{,yy}$ (bottom) along the x-axis ($x,y=0$) and along the y-axis ($x=0,y$) respectively.

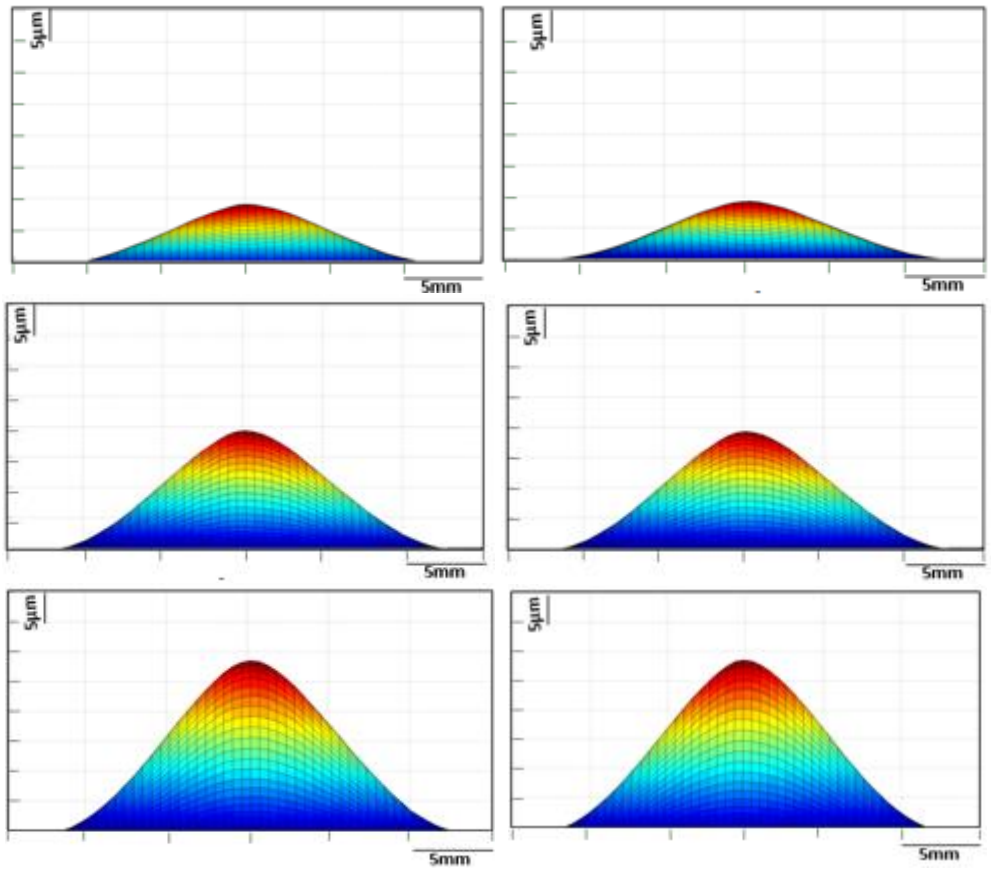

Figure 3.7: Surface plots of integrated values of $\frac{\partial w}{\partial x}$ (left) and $\frac{\partial w}{\partial y}$ (right) for 10 μm, 20 μm, 30 μm respectively corresponding to clamped silicon wafer subjected to central out-of-plane displacement.

Figure 3.7 shows the variation of out-of-plane displacement along the major diameters. Again from the two plots, it can be seen that the integration results agree with the applied displacements very well and the deformed shape of the plate for this axisymmetric problem is as expected. The integrated values reveal that the peak value of integrated data is slightly lower than the applied displacement in each case. This is attributed to the potential inaccuracy (backlash) of the micrometer used to apply the central displacement.

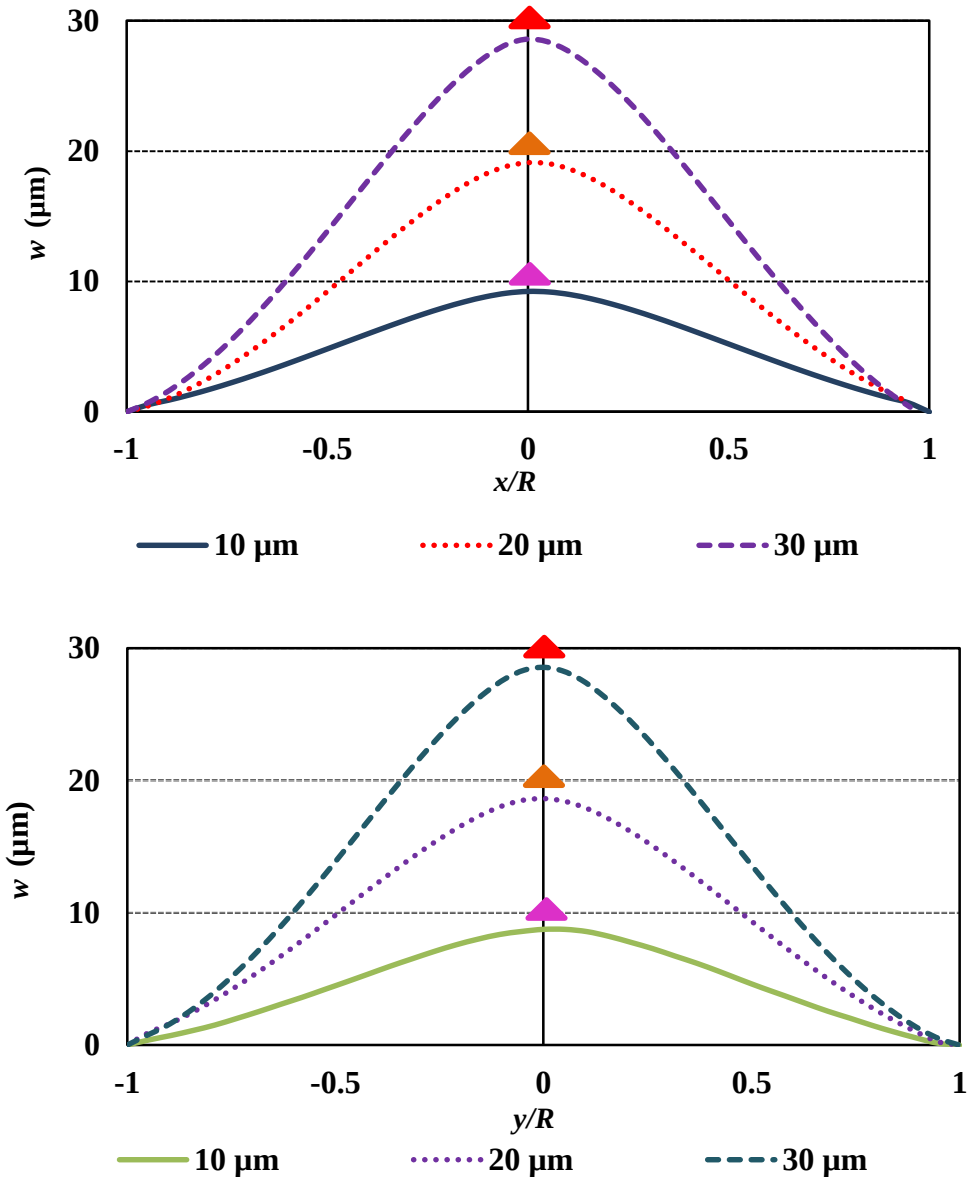

Figure 3.8 Variation of w (out of plane displacement) along x, $y=0$ (top) and $x=0$, y (bottom) obtained by integration of $\frac{\partial w}{\partial x}$ and $\frac{\partial w}{\partial y}$ respectively (applied out-of-plane displacements are represented by symbols).

3.4 Effect of speckle size on measurements

The experiments described above were performed using three different speckle sizes categorized as fine, medium and coarse. The choice of the speckle size was made based on the distance of the specimen from the camera lens, the area of interest and also the magnitude of deformation to be measured. Figure 3.9 shows recordings of all the three speckle patterns used in this experiment.

Figure 3.9: Fine (left), medium (middle), coarse (right) target speckle patterns used in this experiment. (The straight edge of the silicon wafer is located at the top-right of each image).

Figure 3.10 shows $\frac{\partial w}{\partial y}$ contours for an applied displacement of 20 μm. These were obtained by analyzing speckle images by segmenting them into 20 x 20 pixels (1 pixel covered 41.03 μm (fine speckles), 38.76 μm (medium speckles) and 39.6 μm (coarse speckles) on the target plate) during image correlation. Also Figure 3.11 corresponds to the variation of $\frac{\partial w}{\partial y}$ along the vertical axis ($x=0, y$). From the figures it can be seen that good repeatability exists in the measured values of surface slopes from three different sets of speckle targets used.

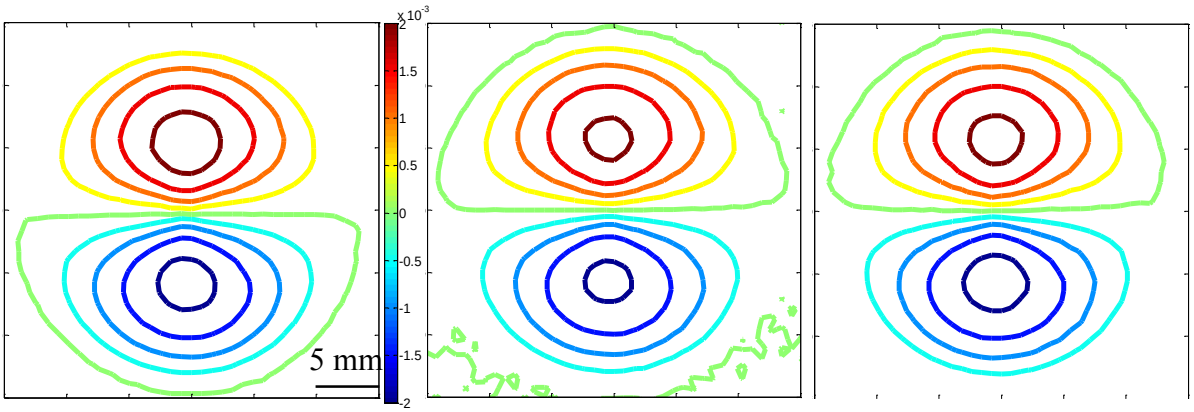

Figure 3.10: Contours of $\frac{\partial w}{\partial y}$ for an applied displacement of 20 μm. Fine (left), medium (middle), coarse (right) speckle patterns used for measurement. Contour levels are in 5 x 10^{-4} radians.

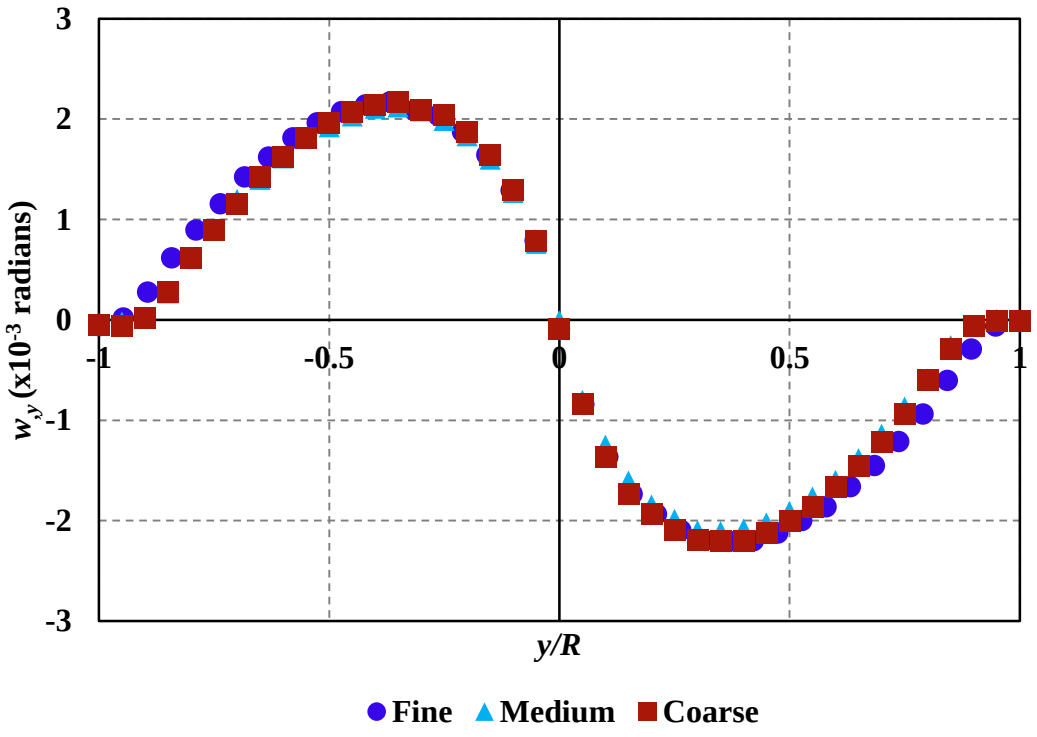

Figure 3.11: Variation of $w_{,y}$ along the vertical axis ($x=0, y$) for an applied out-of-plane displacement of 20 μm.

3.5 Effect of sub-image size

The angular deflections in r-DGS relies on 2D DIC of reference and deformed speckle images, hence correlation parameters such as the sub-image size plays a vital role in the evaluation of surface slope components. The sub-image size chosen here was based on achieving correlation at all points as it was necessary and to have slope components available in the whole field measured in order to be able to perform numerical integration to estimate surface topography. The larger sub-image size produces higher averaging effect when compared to the smaller sub-image size[34]. Hence the trade-offs in this regard based need to be understood. Figure 3.13 shows the measured $\frac{\partial w}{\partial y}$ contours for three different speckle targets used. The top row corresponds to $\frac{\partial w}{\partial y}$ contours obt-

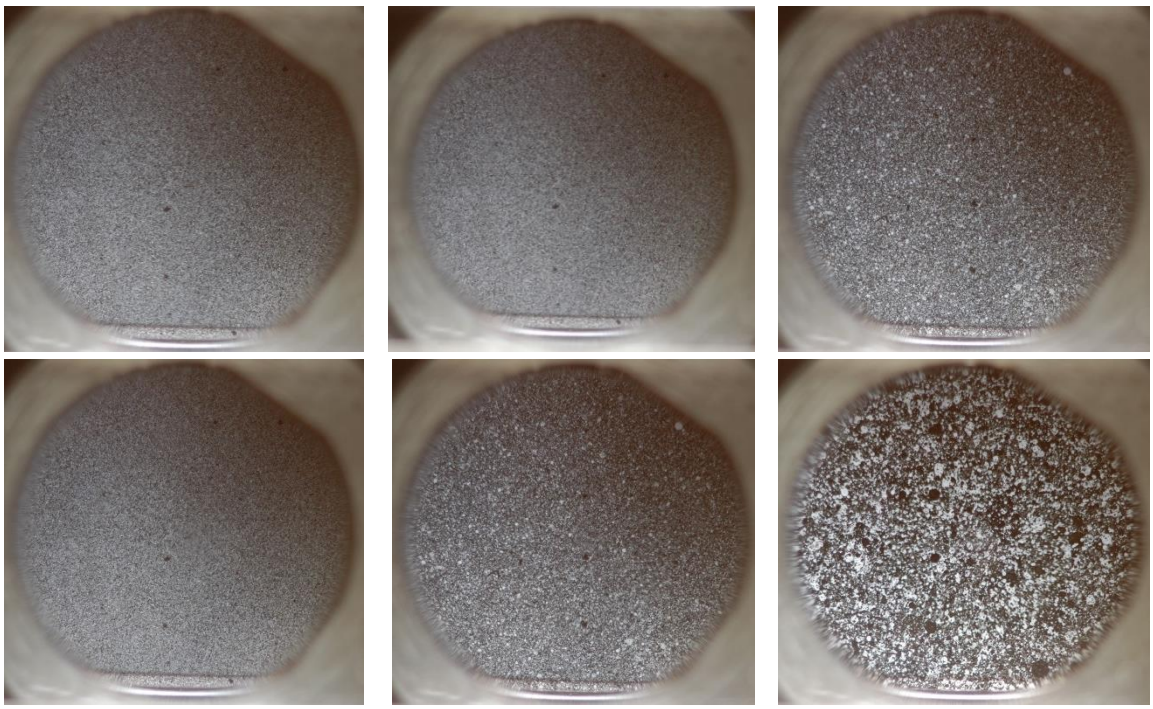

Figure 3.12: Reference images (top row) and deformed images (bottom row) for an applied displacement of 20 μm.

ined by segmenting the image into 20 x 20 pixel sub-images while the bottom row corresponds to $\frac{\partial w}{\partial y}$ contours obtained by segmenting images into 25 x 25 pixel. A good agreement can be seen from the figure.

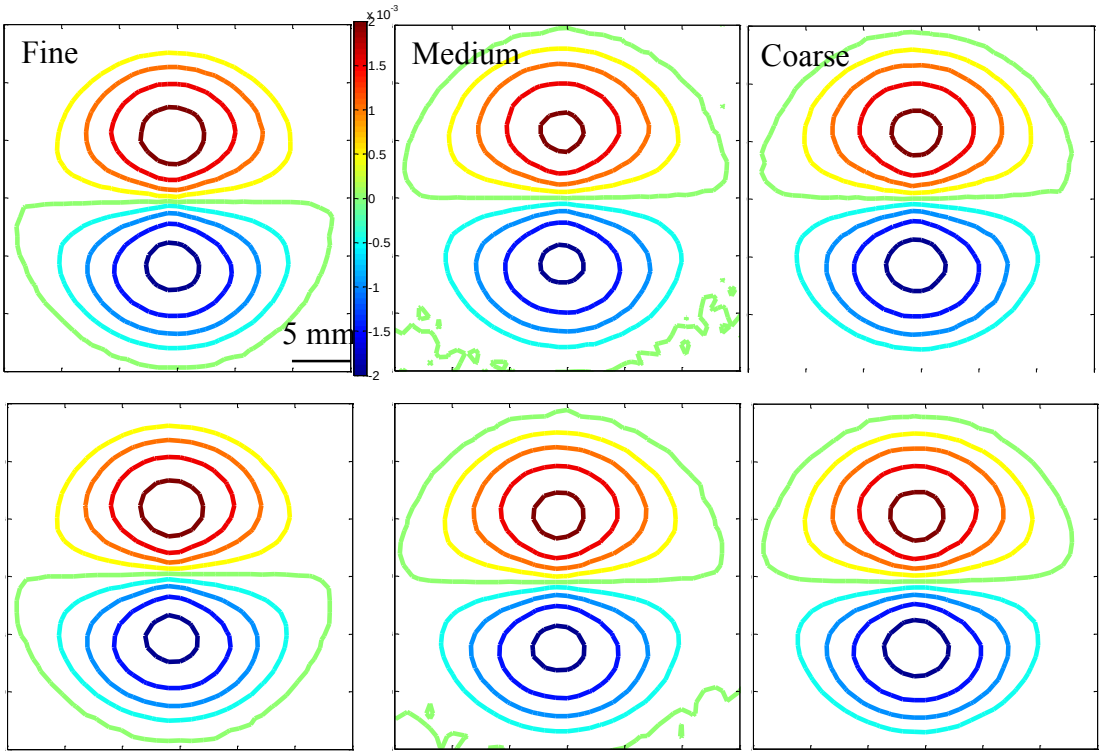

Figure 3.13: Surface slope $\frac{\partial w}{\partial y}$ for an applied displacement of 20 μm. Sub-image size 20 x 20 pixels (top row) and 25 x 25 (bottom row). Contour levels are in 5 x 10^{-4} radians.

3.6 Effect of sub-image overlap

Figure 3.12 shows the effect of overlap of pixels during correlation. The surface slope $\frac{\partial w}{\partial y}$ contours in Figure 3.12 (left) correspond to sub-image size of 20 x 20 pixels without overlap while the figure on the right corresponds to the $\frac{\partial w}{\partial y}$ contour obtained by segmenting the image into 25 x 25 pixels with 10 pixel overlap.

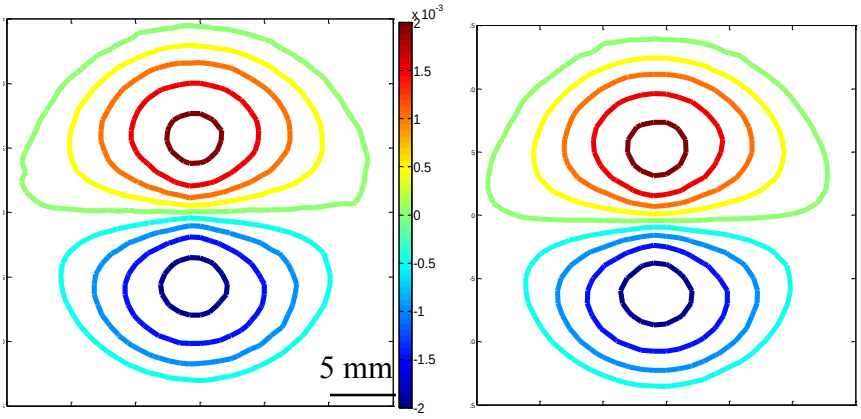

Figure 3.14: Surface slopes $\frac{\partial w}{\partial y}$ for an applied displacement of 20 μm. Sub-image size 20 x 20 pixels without overlap (left) and 25 x 25 pixels with 15 pixels overlap (right). Contour levels are in 5 x 10^{-4} radians.

3.7 Effect of target plate distance

Figure 3.15 shows the speckle images for different target plate distances. One pixel covered 56 μm in 3.15(a), 57.1 μm in 3.15(b) and 58.5 μm in 3.15(c). Figure 3.16 shows the measured $\frac{\partial w}{\partial y}$ contours for three different speckle target plate distances. Also Figure 3.17 corresponds to the variation of $\frac{\partial w}{\partial y}$ along the vertical axis ($x=0$, y) for an applied 20 μm out-of-plane displacement. Again, good agreement is evident from the figures despite changing the value of target distances.

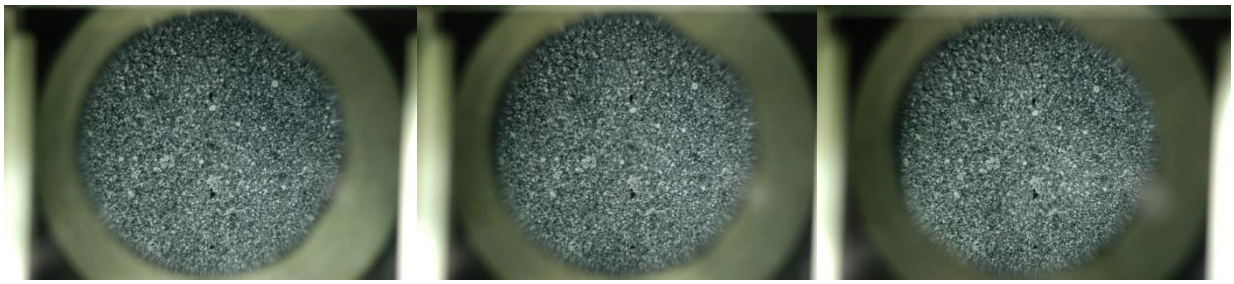

Figure 3.15: Speckle images for different target plate distance. (a) 65mm (b) 85 mm (c) 110mm.

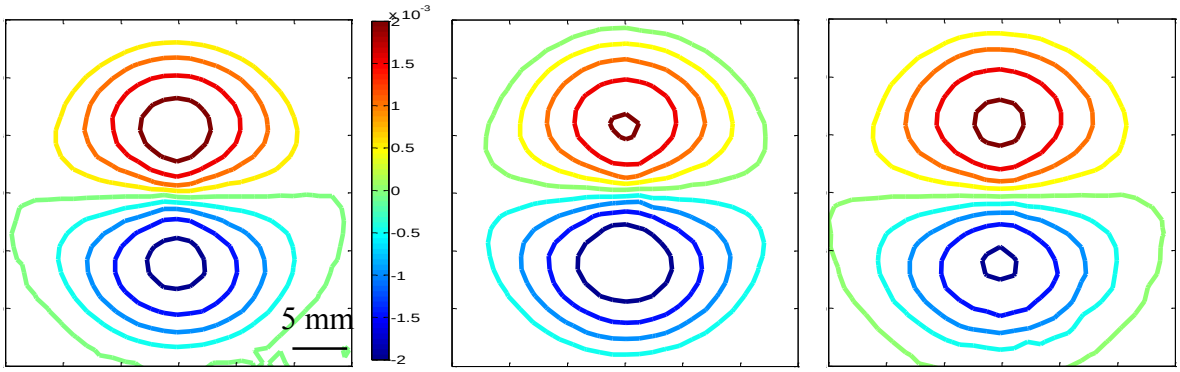

Figure 3.16: Contours of $\frac{\partial w}{\partial y}$ for an applied displacement of 20 μm. Target plate distances: 65mm (left), 85mm (middle), 110 mm (right). Contour levels are in 5 x 10^{-4} radians.

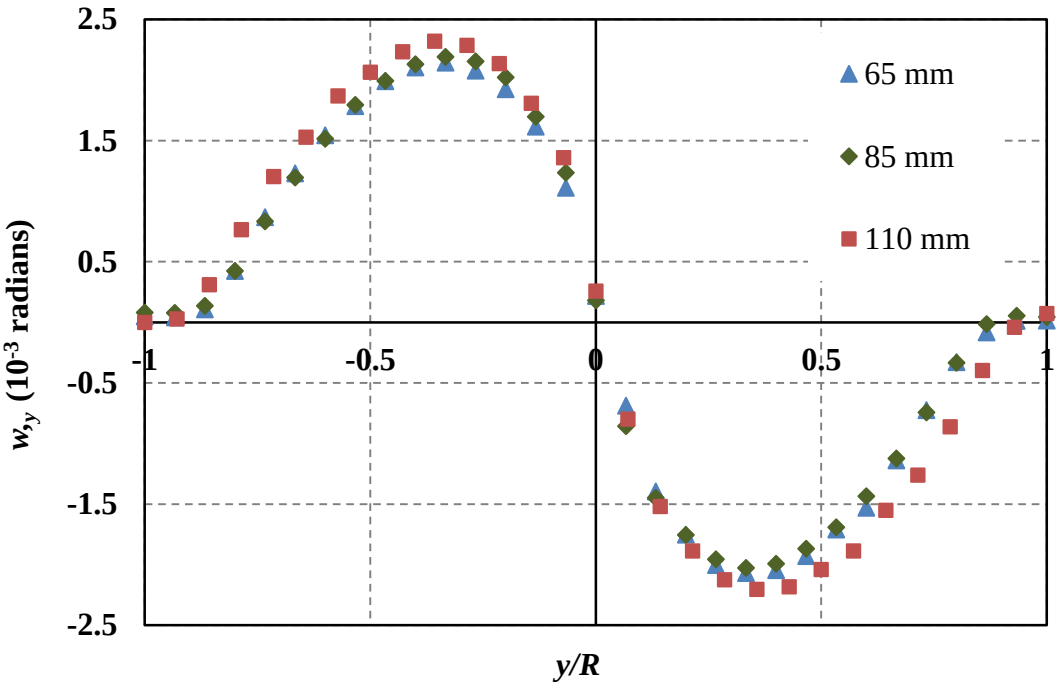

Figure 3.17: Variation of $w_{,y}$ along the horizontal axis ($x=0$, y) for an applied out-of-plane displacement of 20 μm.

3.8 Repeatability study

Next a repeatability study was carried out using the silicon wafer loading apparatus described earlier. The experiment was performed by applying an out-of-plane displacement of 10

μm, 20 μm, 30 μm considered as loading cycle. Next the micrometer was retracted by 10 μm and an image corresponding to an applied displacement of 20 μm was captured. Images from loading and unloading cycles were correlated by segmenting the image into 20 x 20 pixels without any overlap. Figure 3.18 shows the $\frac{\partial w}{\partial y}$ contours obtained by correlating images from the loading (left) and unloading cycles (right). Again, a very good agreement can be seen from the measured slope contours.

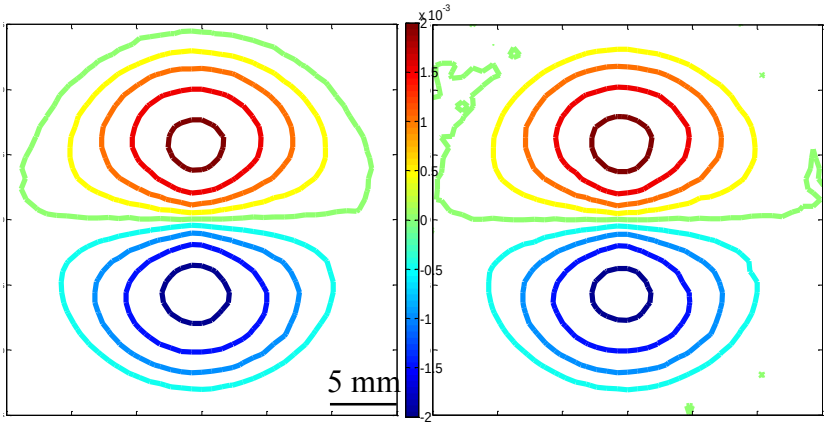

Figure 3.18: Surface slope $\frac{\partial w}{\partial y}$ for an applied displacement of 20 μm. The contours on the left and right correspond to loading and unloading cycles. Contour levels are in 5 x 10^{-4} radians.

3.9 Dynamic impact of thin plates

Periasamy and Tippur [33] have shown that the reflection-mode DGS with time-lapse photography can be applied to monitor time-resolved surface slopes for slow speed events (lasting minutes) such as warping of a silicon wafer due to *in-situ* curing of a thin polymer layer. In this work, the feasibility of the method to study deformation of plate-like structures subjected to stress-wave dominant loading conditions using high-speed digital photography is developed.

3.10 Experimental details

A PMMA (poly-methyl methacrylate) disk of 3 mm thickness and 76.2 mm diameter was used for conducting an impact loading experiment. One face of the disk was made reflective by sputter coating a thin layer of aluminum using vacuum chamber. The schematic of the experimental setup is as shown in Figure 3.19. The target plate was placed at a distance (= Δ) 110 mm from the disk. The PMMA disk was held in position using three 3M soft-gel dots to simulate a free-free boundary condition. A steel ball of diameter 25.4 mm travelling at a speed of 2.3 m/s was used to impact the PMMA disk center. A Cordin (model 550) multi-sensor high-speed digital camera was used for recording speckle images at a speed of 80,425 frames per second was used to capture deformations due to propagating stress waves in PMMA disk after impact. The high-speed camera equipped with 32 CCD sensors was capable of capturing images sequentially upon an initial trigger produced by a photo-gate device. The device consists of two sensors which detect motion and produce a trigger voltage to turn on the camera to capture images. Two sets of images, one captured before the impact and the other during the impact event, were correlated using 2D DIC software ARAMIS. In these experiments, the images as shown in Figure 3.21 were segmented into 30 x 30 pixels (1 pixel covered 76 μm on the target plate) without overlap to extract the displacement components. Here a larger sub-image size was chosen in order to achieve correlation over the entire image as coarse speckles were employed in these experiments.

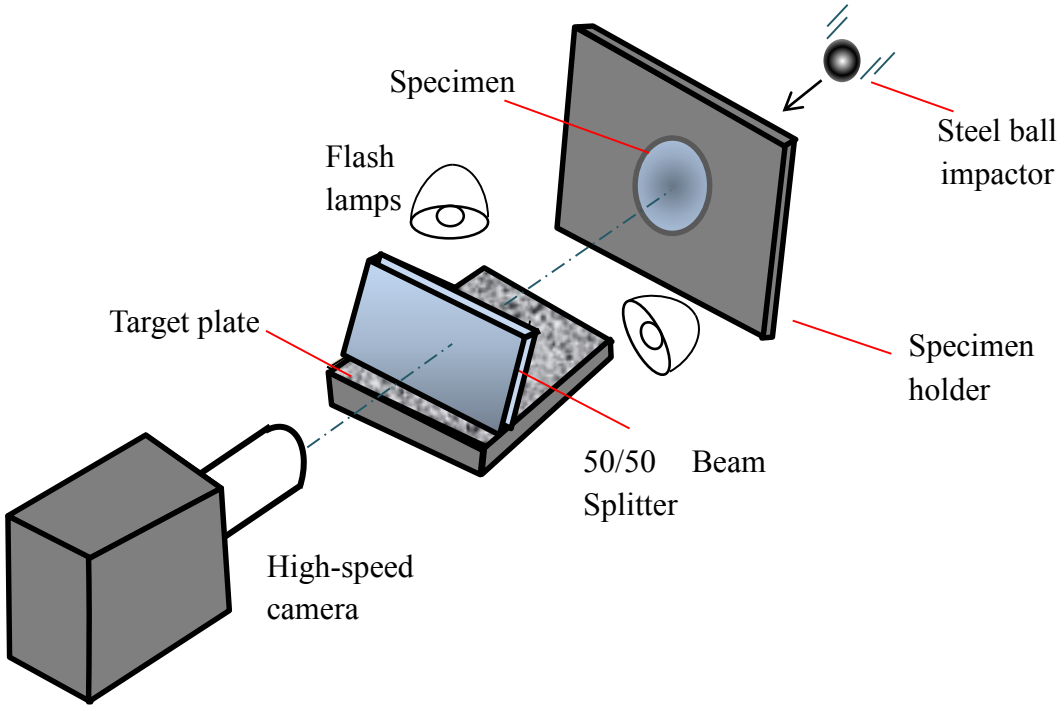

Figure 3.19: Schematic of the experimental setup to measure surface gradients due to transient wave propagation in the disk due to impact.

3.11 Surface slopes due to transient wave propagation

The resulting time-resolved contour plots of angular deflections of light rays in the *x*-*z* and *y*-*z* planes and the corresponding surface slopes due to transient wave propagation are shown in Figures 3.22 and 3.23, respectively. In these, the frame immediately prior to the one where surface slope contours are evident is considered the start of the event or $t = 0$. The qualitative resemblance between these contours with the quasi-static counterparts shown in Figure 3.3 is clearly evident. The longitudinal wave speed in PMMA is approximately equal to 2500 m/sec. Thus, the impact induced stress waves take ~30 μsec to reach the outer edge of the circular disk and ~60 μsec to re-

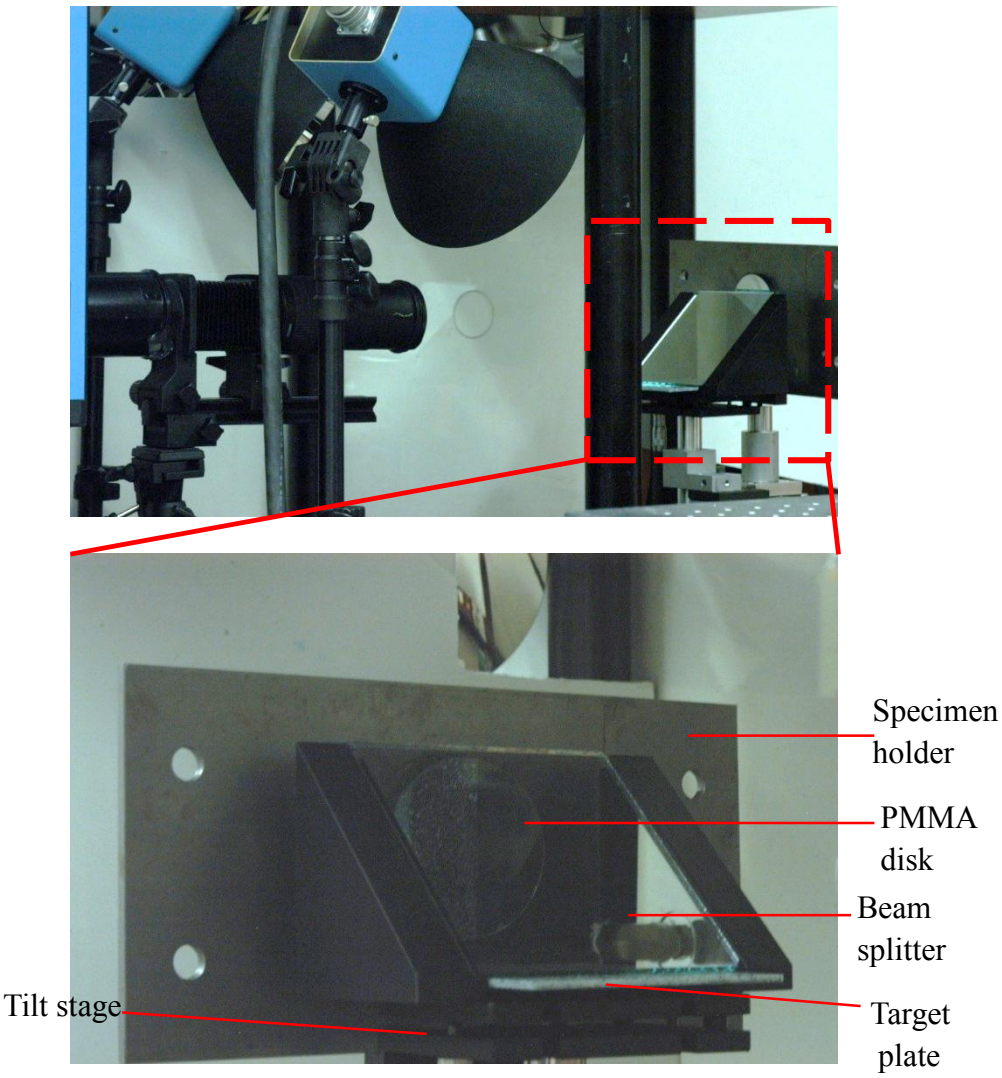

Figure 3.20: Photograph of the experimental setup to measure surface slopes due to transient stress wave propagation in a circular disk. The photo at the bottom shows a close up view of the disk with the beam splitter/target in front of it.

flect back from the edges reaching the impact point (or the origin). In view of this, the deformations in the early stages of impact are highly local, close to the origin, with the rest of the plate undeformed and a zero slope value. This situation is akin to a thin circular plate clamped along its periphery subjected to a central deflection, as reported in the silicon wafer. Accordingly, the two orthogonal surface slope contours shown in Figures 3.22 and 3.23 show qualitative resemblances to those in Figure 3.3. Further the vectorial sum of the two measurements, shown in Figure 3.24,

depicts the expected axisymmetric nature of deformations relative to the impact point. Increase in the number of contours between two successive images indicates the time-dependent deformations as the stress waves propagate in the disk.

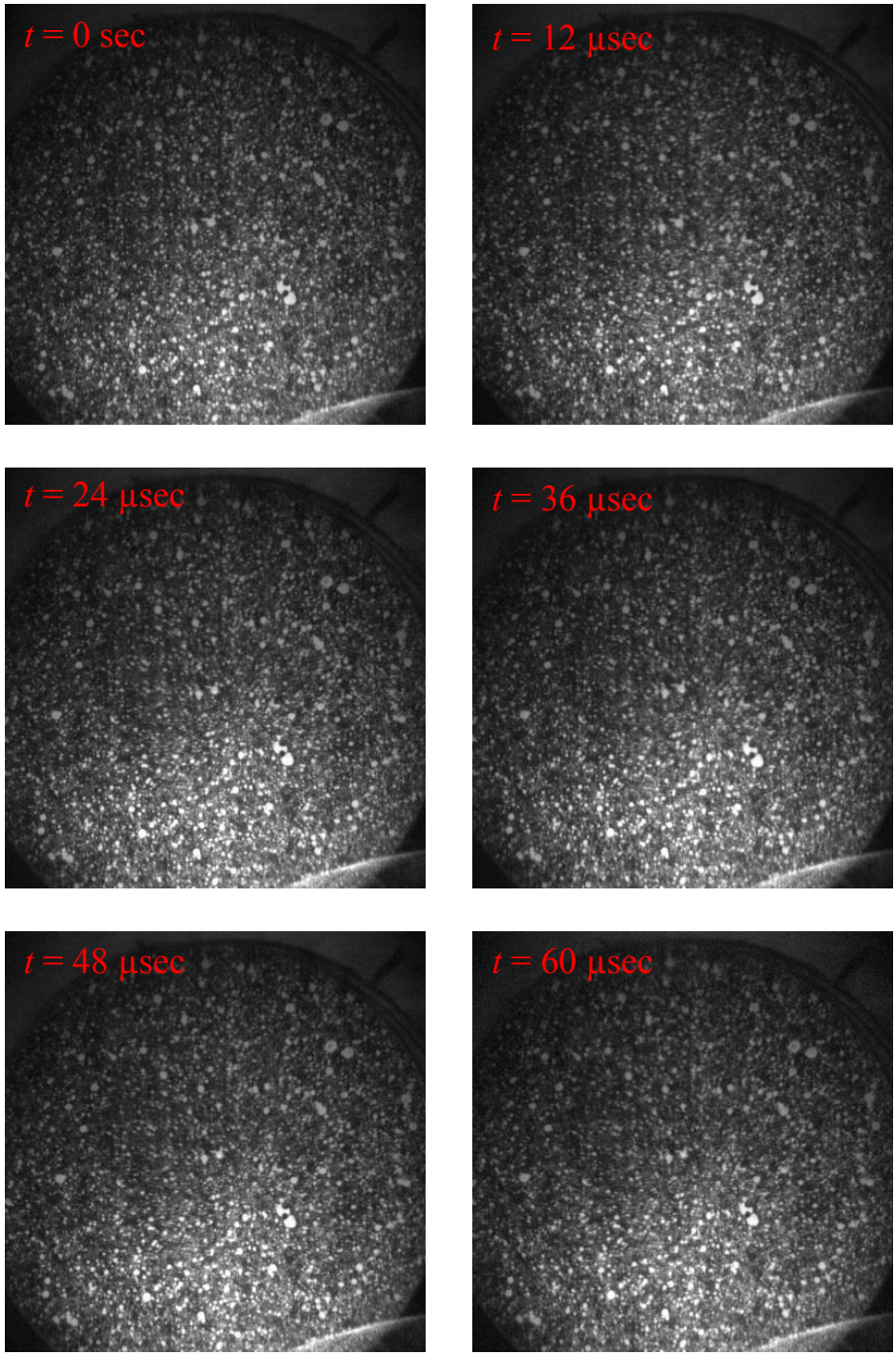

Figure 3.21: Speckle images corresponding to the transient wave propagation due to impact.

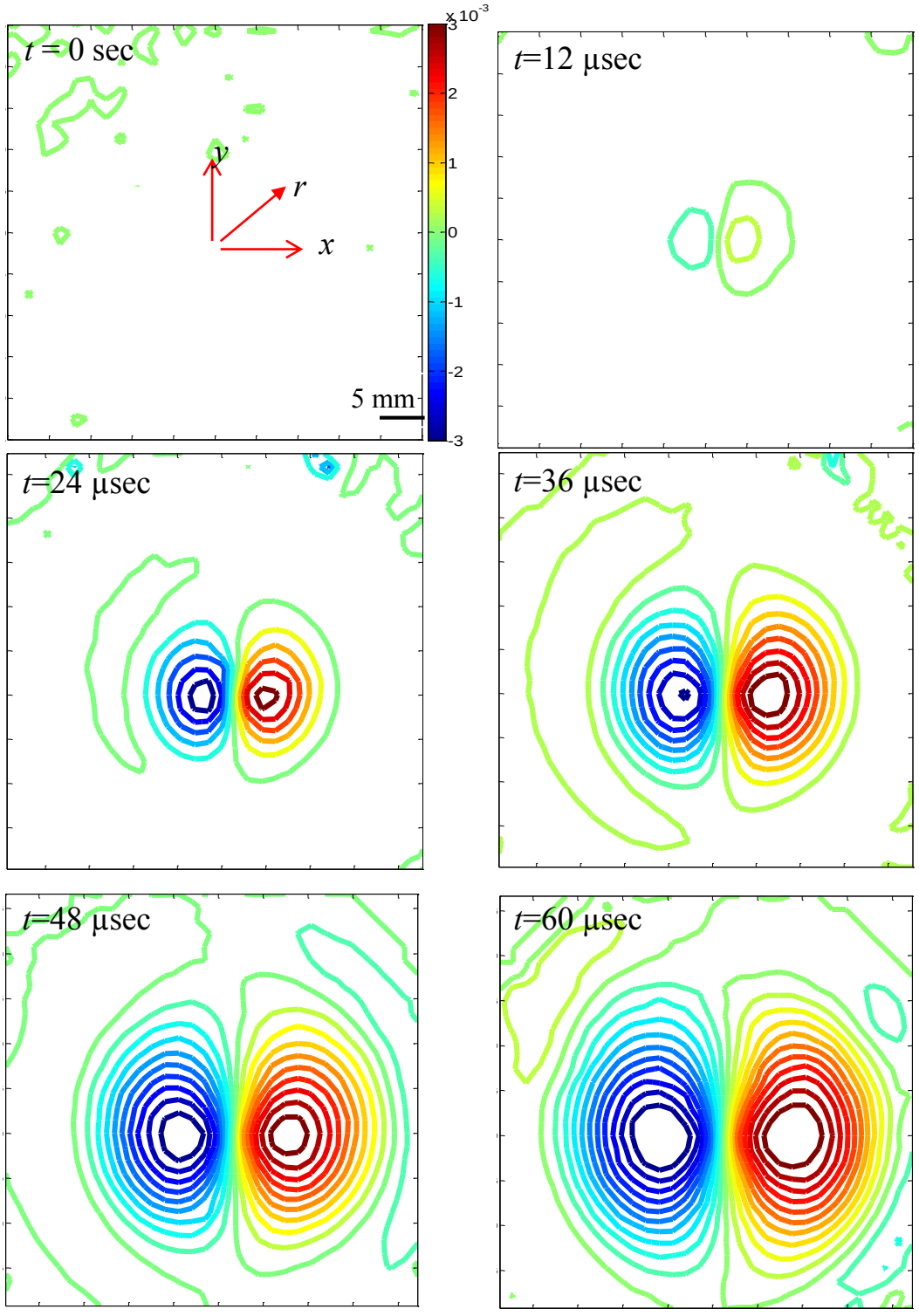

Figure 3.22: Evolution of ϕ_x contours due to impact of a reflective PMMA disk by a steel ball at 2.3 m/s. The contour levels are in 3 x 10^{-4} radians.

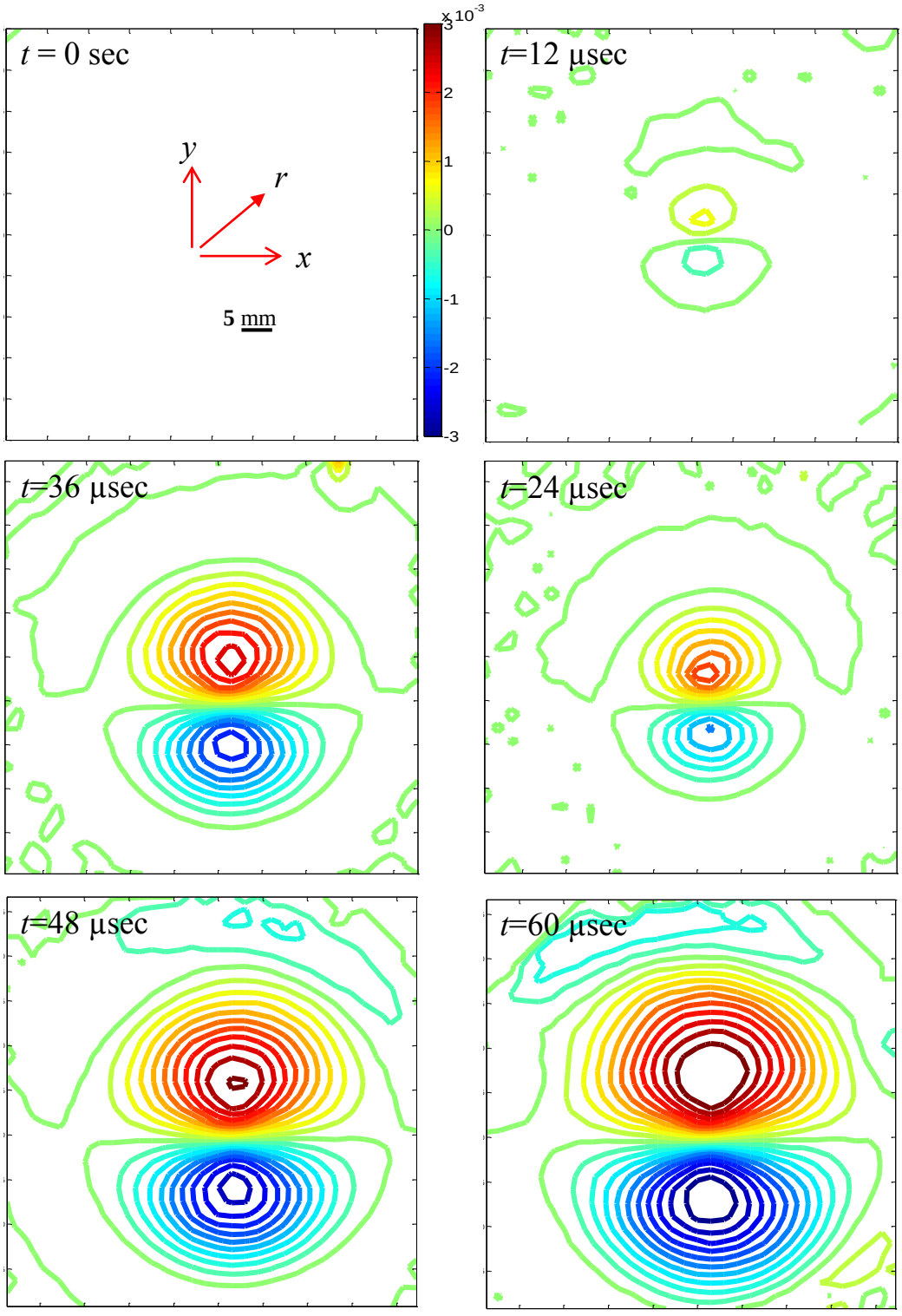

Figure 3.23: Evolution of ϕ_y contours due to impact of a reflective PMMA disk by a steel ball at 2.3 m/s. The contour levels are in 3 x 10^{-4} radians.

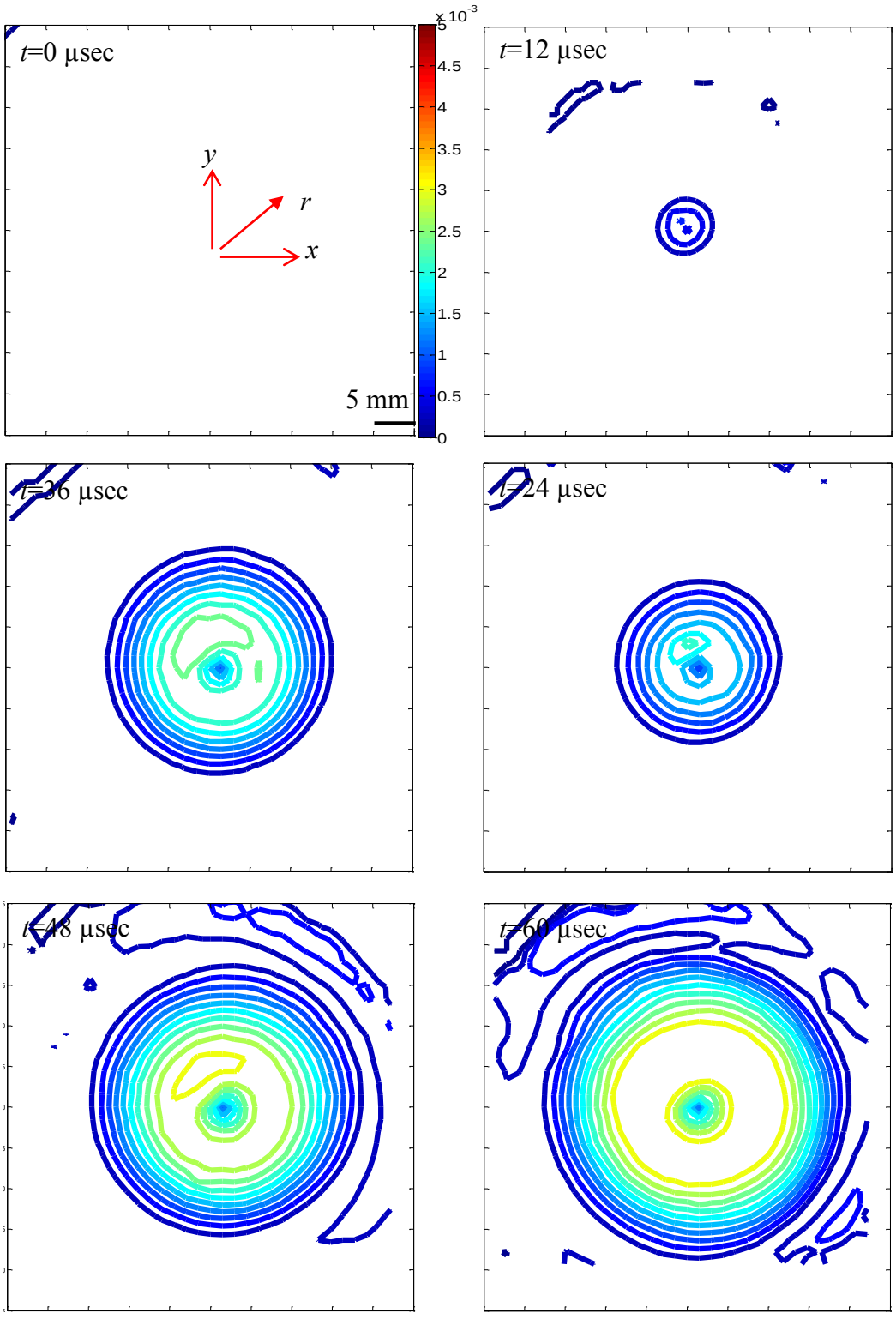

Figure 3.24: Evolution of $\phi_r \left(=\sqrt{\phi_x{}^2 + \phi_y{}^2}\right)$ contours due to impact of a reflective PMMA disk by a steel ball at 2.3 m/s. The contour levels are in 3 x 10^{-4} radians.

For completeness, these measured surface slopes were differentiated using the formula described in equation 3.3 to estimate the curvatures in two orthogonal directions. Figure 3.25 show thus obtained curvature contours at two different time instants. Figure 3.26 shows the variation of $\frac{\partial^2 w}{\partial y^2}$ along the horizontal axis for two different time instances. The slope information was also numerically integrated as in the quasi-static case using a simple trapezoidal rule to estimate the out-of-plane displacements. Thus obtained out-of-plane displacements (w) along the

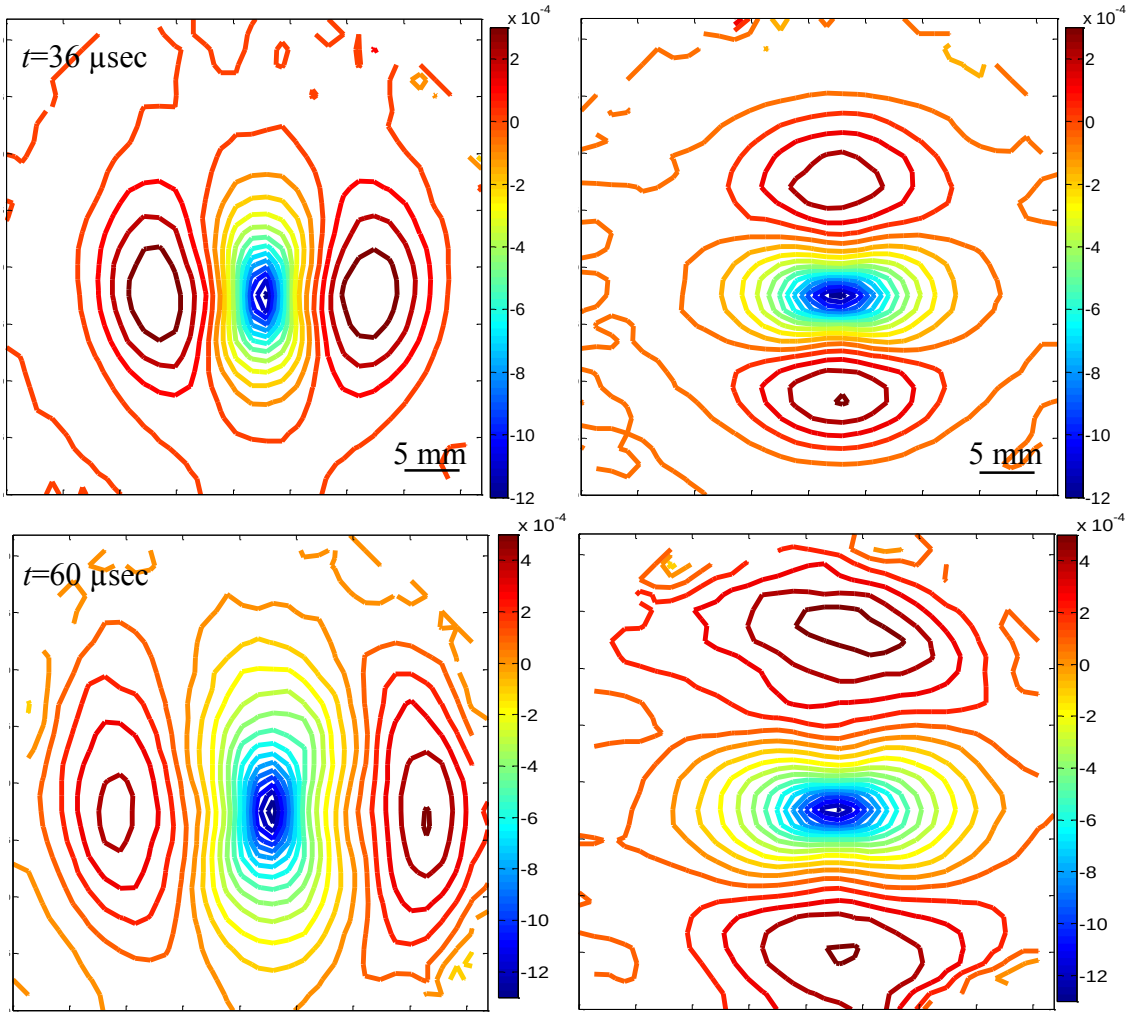

Figure 3.25: Contours of $\frac{\partial^2 w}{\partial x^2}$ (left) and $\frac{\partial^2 w}{\partial y^2}$ (right) due to transient wave propagation in PMMA disk. The contour levels are in 1 X 10^{-4} mm^{-1}.

horizontal and vertical radius of the disk, evaluated from the array of DGS data for each sub-image, are plotted in Figure 3.28 and 3.29 as symbols.

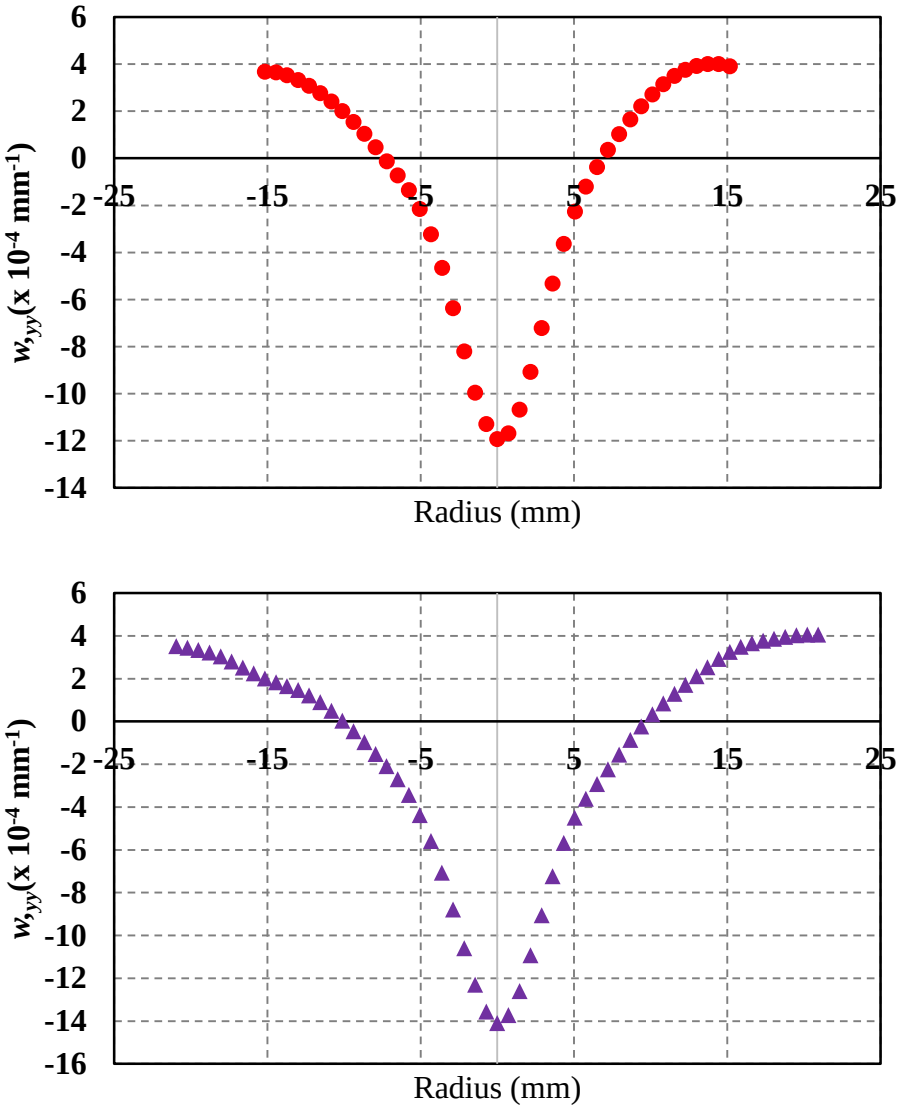

Figure 3.26: Variation of $w_{,yy}$ for t = 36 μs (top) and t = 60 μs (bottom) respectively along the y-axis ($x=0,y$).

3.12 Finite element simulations

A companion finite element simulation was performed using ANSYS™ Workbench software package and a quarter model was simulated. The model was discretized into 500095 quadratic elements (explicit time integration) with 518718 nodes. Frictionless interaction was

defined between the two bodies. The time steps during the analysis were allowed to be automatically controlled by the explicit integration scheme. Output was requested at every 12 μseconds to match with the experimental time interval between two successive images. The dynamic elastic modulus and Poisson's ratio were assigned as 5.8 GPa and 0.27 respectively[35]. The velocity of the steel ball of 2.3 m/sec, measured by a photodetector during the experiments, was used as an input in these simulations.

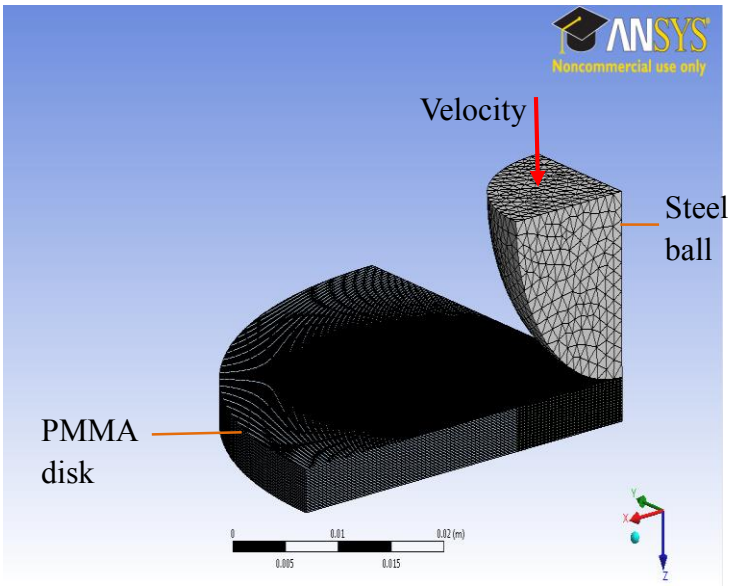

Figure 3.27: Finite element model (quarter model) of ball impact on the PMMA plate.

The out-of-plane displacements along the major diameter on the lower face of the plate were extracted every 12 μsec. The numerical data from the simulation are superimposed on the experimentally obtained out-of-plane displacements in the Figures 3.28 and 3.29. It can be seen that there is a good agreement between both data demonstrating the feasibility of r-DGS for stress-wave dominant problems.

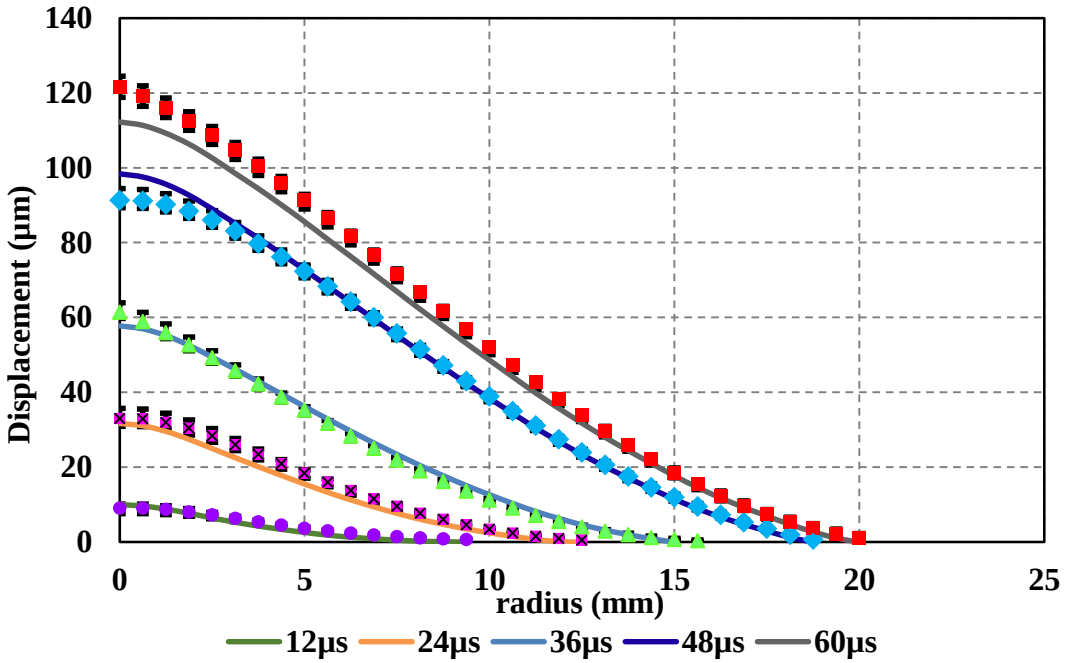

Figure 3.28: Variation of *w* (out of plane displacement) along *(x, y=0)* of $\frac{\partial w}{\partial x}$. Solid lines represent values from FEA.

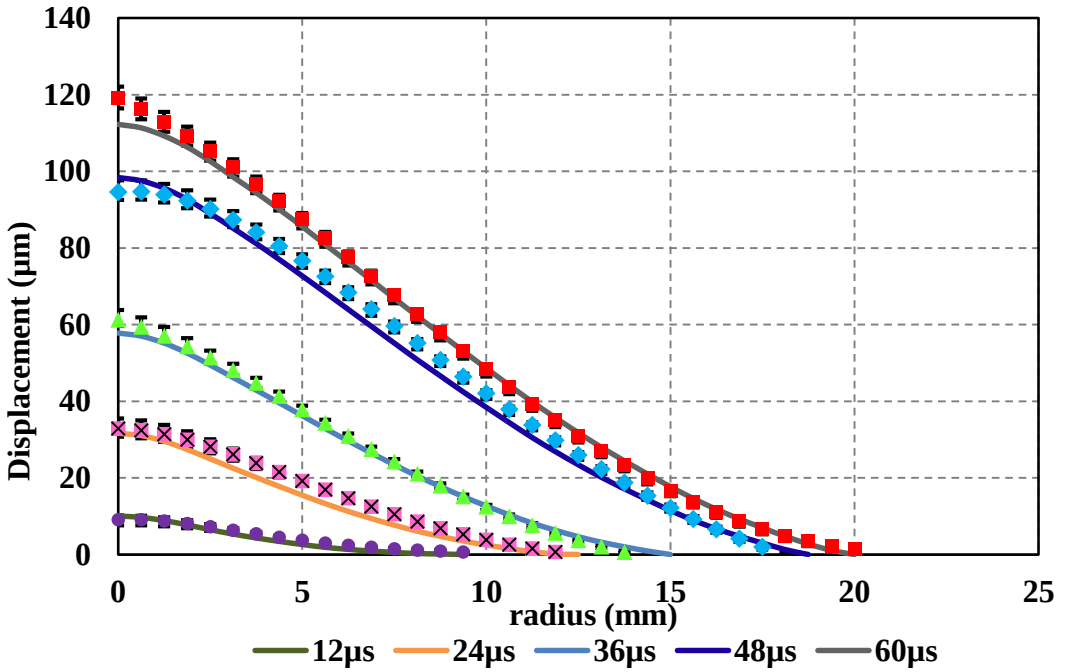

Figure 3.29: Variation of *w* (out of plane displacement) along (*x=0, y)* obtained by integration of $\frac{\partial w}{\partial y}$. Solid lines represent values from FEA.

Chapter 4 : Applications to Disbond and Damage Detection: Feasibility Studies

This chapter details the feasibility of r-DGS method to detect disbond and damage in layered thin plates. First a disbond detection study is carried out on an adhesively bonded bi-layered PMMA plate. Subsequently its applicability is extended to detect delamination due to mechanical impact on a glass fibers woven epoxy composite plate. Lastly, the method is implemented to visualize deformations of a silicon flip-chip assembly to demonstrate its applicability to study thermo-mechanical deformation of electronic packages in service. In view of its simplicity, thermal excitation is used in all these cases to detect the damage and deformations[36].

4.1 Experimental details

Experiments were performed to identify disbond and delamination in (a) thin plates bonded using an acrylic adhesive and (b) on composite plates subjected to impact loading. A schematic of the r-DGS experimental setup used is as shown in Figure 4.1. Specularly reflective test specimens were held vertically in a screw-type sample holder (optical mounts from Edmund Optics) at the bottom edge. The holder consists of two screws 40 mm apart. The bi-layered PMMA plates were held in the holder at a single point with the help of a screw while the composite plate and silicon die were held at two points using the same holder. A 50/50 beam splitter and a target plate coated with random speckles were arranged in front of the specimen to incident the speckle pattern on the reflective face of the specimen for recording. The target plate distance (= Δ) was 105 mm for dis-

bond detection and 65 mm for delamination detection experiments, respectively. A Nikon D100 digital SLR camera with 28-300 mm focal length lens was placed in front of the specimen to photograph the speckle pattern on the specimen. A 75 W lamp was placed behind the specimen at an approximate distance of 70 mm to excite it thermally and produce deformations. A reference image was recorded using a camera resolution of 1504 x 1000 pixels (one pixel covered 73.08 µm and 43 µm in disbond detection and delamination detection, respectively). Deformed images of the specimen were captured after 15 minutes of turning the lamps 'on'. As the specimen absorbed thermal energy, it deformed resulting in the disbonded and damaged regions causing local anomaly in an otherwise uniform r-DGS contour maps due to abrupt changes in surface slopes. The variation in the temperature on the back surface was approximately 3-6 degrees C (for 15 minutes of heating). The images corresponding to the deformed state along with the one from the reference state was then used to extract surface gradient fields ($\frac{\partial w}{\partial x}$ and $\frac{\partial w}{\partial y}$) using 2D digital image correlation.

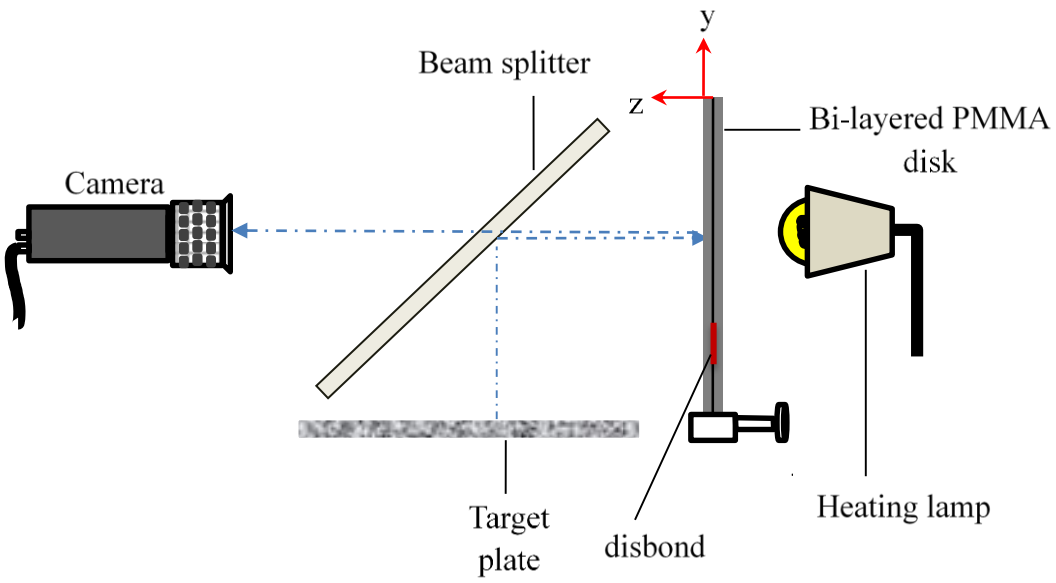

Figure 4.1: Schematic of the experimental setup for disbond detection using r-DGS.

4.2 Disbond detection in laminated plates

Two isotropic PMMA plates of ~1.5 mm thickness and 76.2 mm in diameter were used in this study to prepare a bi-layered disk. The sample preparation involved the two plates bonded together using an acrylic adhesive (Weldon 16). To create a disbond on the interface, one of the faces of PMMA plates was coated with a layer of release agent (BUEHLER 20-8185-002, approx. 25 mm in diameter) as shown schematically in the Figure 4.2. The specimen was allowed to cure for a time period of 48 hours. One of the faces of the cured bi-layered disk was made specularly reflective by coating it with a layer of aluminum using vacuum deposition. Two samples, nominally identical in geometry, one with a layer of release agent coating to create a disbond and the other without disbond were prepared for comparative study. The disks were subjected to thermal loading using an incandescent lamp, as described previously. The surface deformations due to thermal loading between the samples were examined to detect the disbond via abnormalities in the surface slope contours measured using r-DGS.

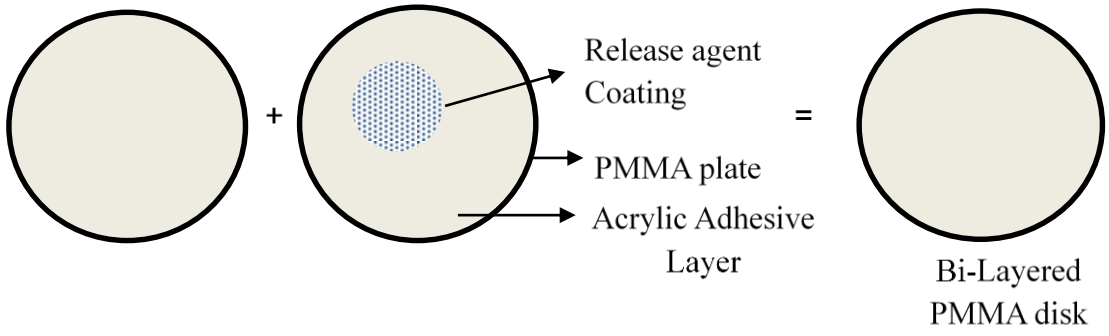

Figure 4.2: Schematic for specimen preparation used for demonstrating disbond detection in bi-layered PMMA disk.

Figures 4.3 show photographed speckle images representing the reference (at room temperature) and thermally excited states of the specimen. Note that Figure 4.3 (right) corresponds

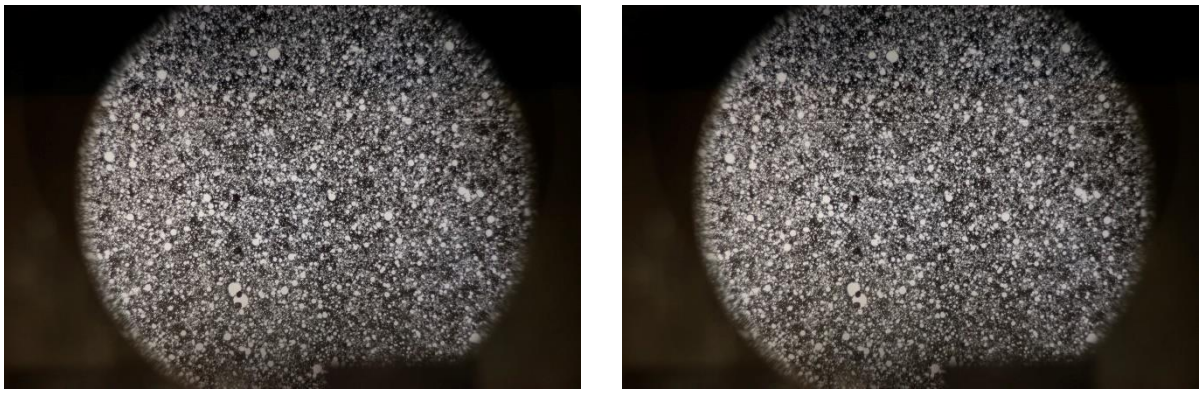

Figure 4.3: Reference (left) and deformed (right) images of speckles from the Bi-layered PMMA plate after 15 minutes of heating.

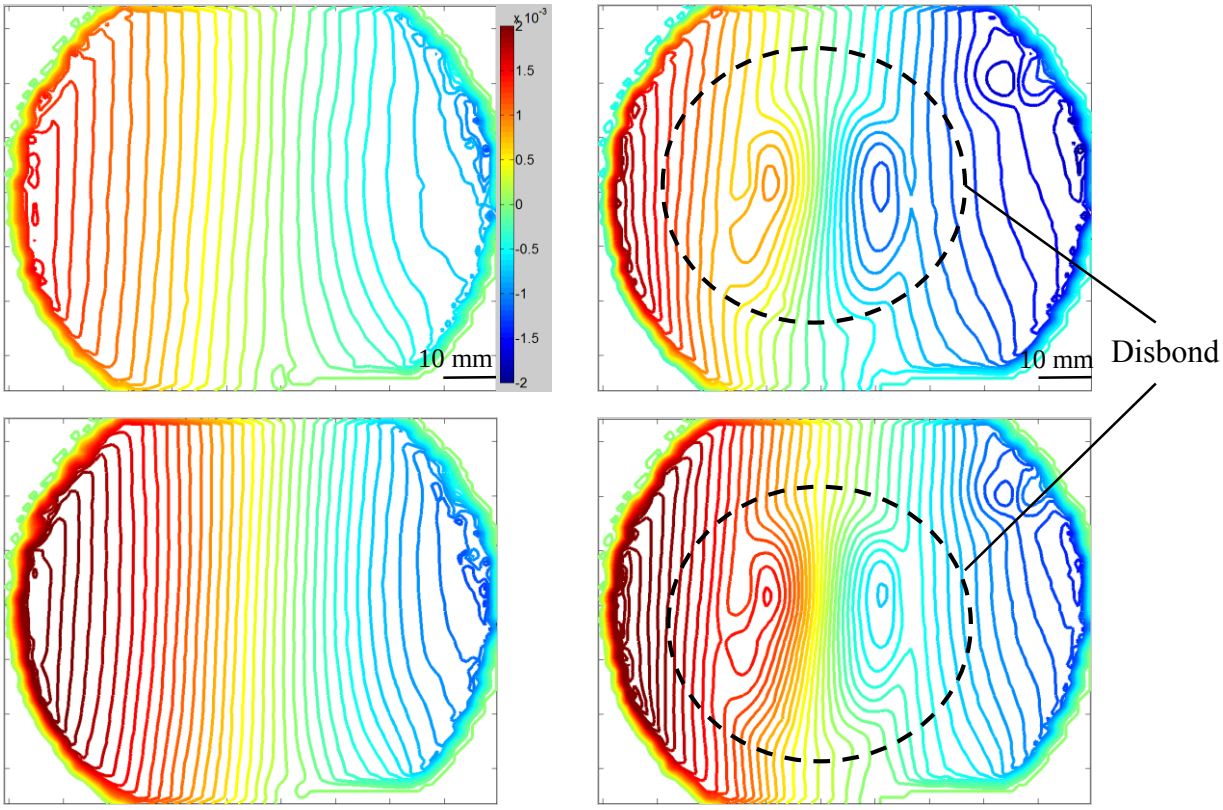

Figure 4.4: Surface slopes representing $\frac{\partial w}{\partial x}$ after 15 minutes (top row) and 30 minutes (bottom row) of heating. Plates without (left column) and with disbond (right column). Disbond region is highlighted in the figure.

a gray scale recording following heating of the disks for 15 minutes and approximately 1 minute of cooling off period.

Figures 4.4 and 4.5 show the resulting orthogonal surface slope contours from r-DGS due to thermal loading of the disks with and without disbond, respectively. During image correlation, the images were segmented into 15 x 15 pixel non-overlapping sub-images. This yielded an array of 99 x 65 data points for analysis.

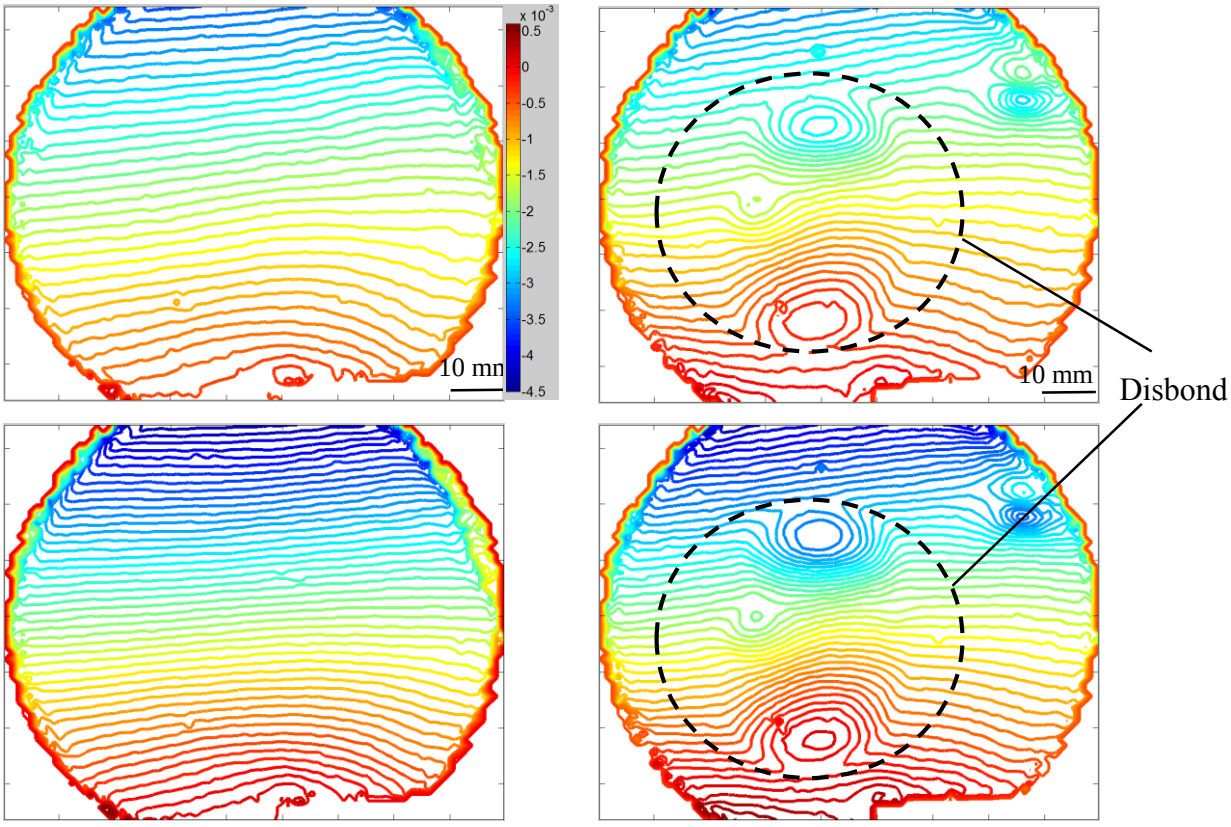

Figure 4.5: Surface gradients $\frac{\partial w}{\partial y}$ after 15 minutes (top row) and 30 minutes (bottom row) of heating. Compact plate (left column) and plate with disbond (right column). Disbond region is highlighted in the figure by the dotted circle.

The surface slope contours in the left column appear to have a relatively uniform spacing (but for the clamp point at the bottom) whereas the contours in the right column show a distinct abnormality that can be attributed to the presence of disbond on the mid-plane of the disk in that region. Interestingly, the contours of $\frac{\partial w}{\partial x}$ show zero slope values coinciding with the vertical axis of symmetry of the disk when clamped at the lower edge of the disk. On the other hand, the

contours of $\frac{\partial w}{\partial y}$ show a monotonically varying slope from the clamped lower edge to the top of the disk, qualitatively consistent with the imposed boundary condition. Further, the number of contours is higher when the disk was exposed to the heating lamp for 30 minutes as opposed to 15 minutes.

4.3 Damage detection in composite plates

Glass fiber reinforced composite plates (G10-FR4 from ePlastics) 76.2 x 76.2 mm^2 and 3.1 mm thickness was used to demonstrate the ability of r-DGS to detect impact induced damage. The composite plate is clamped to a steel support using C-clamps during impact loading, as shown schematically in Figure 4.6. The specimen was impacted using an aluminum impactor having a wedge shaped impact head. The impacting head contacted the composite over a rectangular area of 25.2 x 8.2 mm^2. The impactor system consists of a long-bar using an aluminum striker propelled by compressed gas stored in a cylinder. The striker impact velocity was approximately 8 m/sec. A strain gage (CAE-13-125UN-120 from Vishay Micro-Measurements, Inc) bonded to the long-bar was used to measure the strain history in the bar during impact loading. The strain measurements were done using a Lecroy oscilloscope and an Ectron signal amplifier/conditioner with a quarter Wheatstone bridge circuit. Figure 4.7 shows the measured strain history on the long-bar prior to impact.

The composite plate was prepared next for optical investigation. The face opposite to the impacted face of the composite plate was aluminized using transfer coating method. A PMMA plate was deposited with a thin layer of aluminum using a vacuum deposition system. The surface of the composite that is to be made reflective is cleaned and uncured drops/blobs of epoxy are pla-

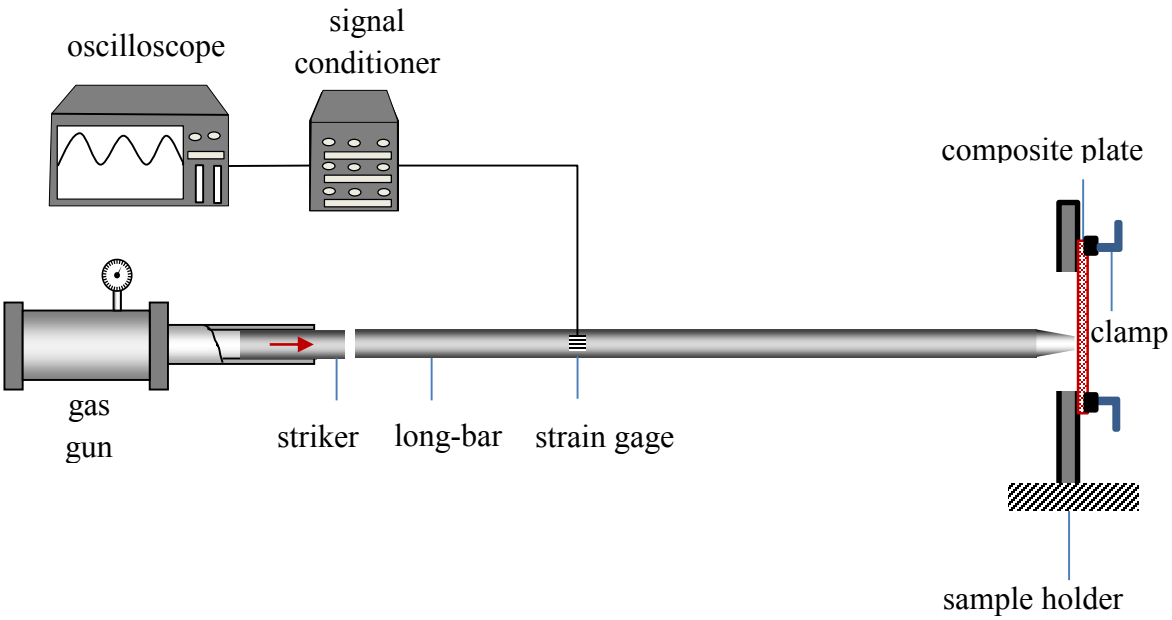

Figure 4.6: Schematic of the impact loading setup used to damage composite plate.

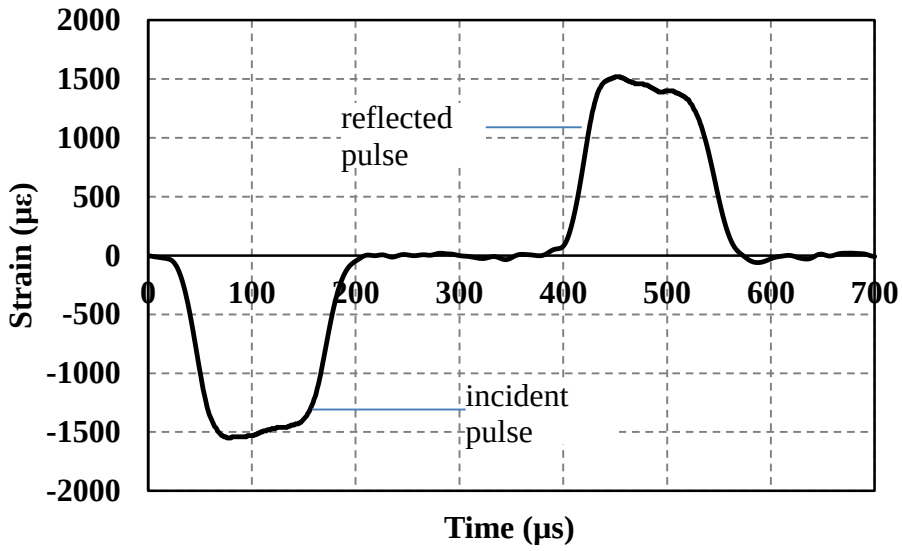

Figure 4.7: Measured strain history on the long-bar impactor using strain gage.

ced on the surface in the region of interest. The PMMA disk with aluminum coating is placed on the composite substrate (aluminized face in contact with the substrate) and excess epoxy is squeezed out using dead-weights. After the epoxy layer (typically a few microns thick) cures, the PMMA disk is pried out from the substrate. Since the bond strength between aluminum and epoxy

exceeds that between aluminum and PMMA, when the disk is pried off the substrate the aluminum layer is left behind on the composite substrate making it a specular substrate. The steps of the process used are shown schematically in Figure 4.8.

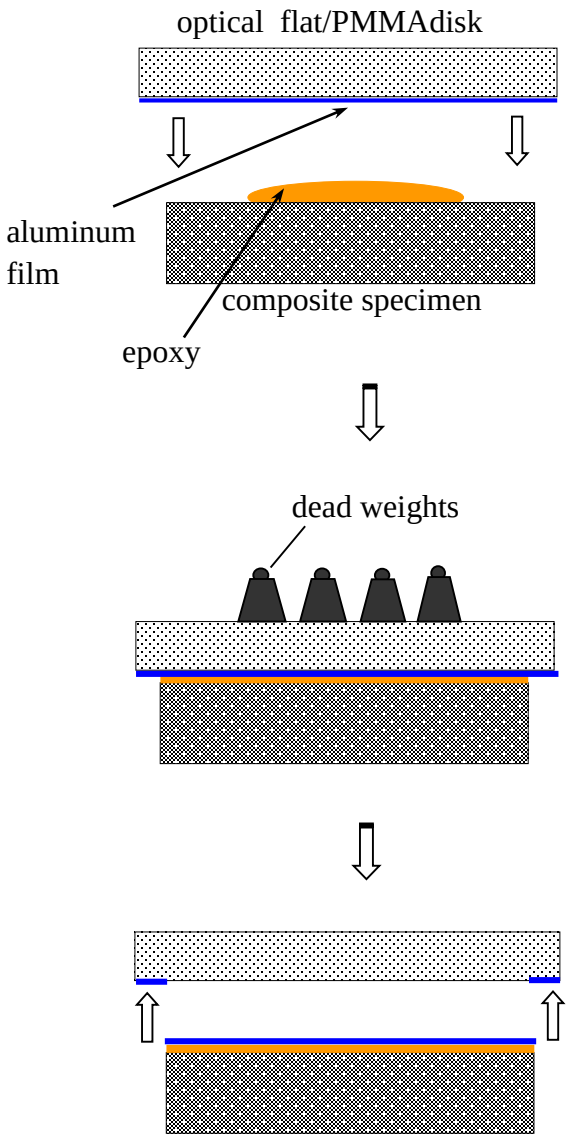

Figure 4.8: Schematic depicting aluminizing an opaque specimen surface to obtain a specularly reflective surface for r-DGS study.

The specimen was then held vertically using a screw clamp as shown in the Figure 4.1 and was subjected to thermal excitation by the incandescent lamp placed on the backside of the sheet when the reflective side faced the camera. Figure 4.11 shows the surface slopes due to thermal excitation for 15 minutes of heating and 5 minutes of cool-off to avoid thermal currents in the specimen neighborhood. (The composite sheet being a black in color absorbed thermal radiation more efficiently than the bi-layered PMMA disk, discussed previously.) The speckle image corresponding to the thermally excited state shows the effect of thermal currents in front of the composite sheet. The speckle images were segmented into 25 x 25 pixel (1 pixel covered 43 μm) subsets with 20 pixel overlap during image correlation. This yielded an array of 48 x 66 data points

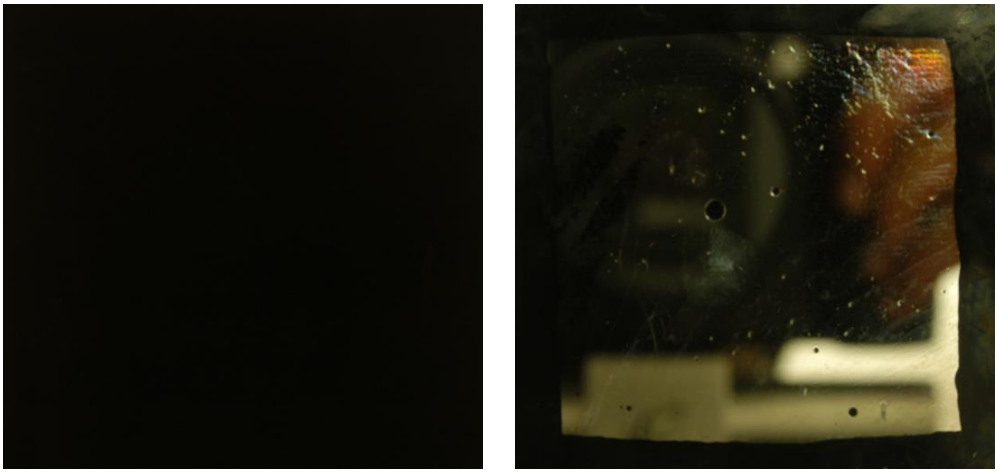

Figure 4.9: G10-FR4 sheet without reflective surface (left) and with reflective surface (right).

for analysis. The delamination can be clearly seen from the surface slope contours. It should be noted although the speckle image in the thermally excited state was recorded somewhat before all the thermal currents died-down, the image correlation operations could be performed, resulting in contour plots depicting the manifestation of the internal damage on the surface. The resulting contour plots are shown in Figure 4.11. The surface slope contours in Figure 4.11 clearly show

Tensile strength, CW(psi)	38,000
Tensile strength, LW (psi)	45,000
Flexural strength, CW (psi)	65,000
Flexural strength, LW (psi)	75,000
Flexural modulus, CW (psi)	2,400
Flexural modulus, LW (psi)	2,700
CTE (x 10^{-5} in./in./°F)	0.66

Table 4.1: Mechanical properties of G10-FR4[4] composite plate

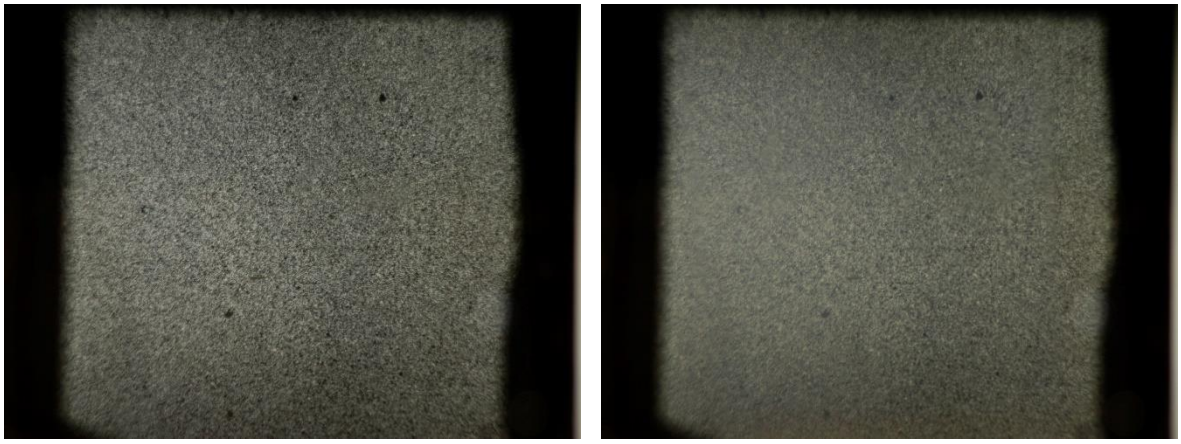

Figure 4.10: Reference (left) and deformed (right) images of speckles taken on the G10-FR4 plate after 15 minutes of heating and 5 minutes of cool-off time.

the foot-print of the rectangular impactor as seen from the opposite side (observing side) of the plate during thermal excitation. The wedge impact being rectangular in shape, concentration of slope contours along the short-edge of rectangle and at the four-corners is evident, demonstrating the feasibility of the method for further quantitative analysis.

[4] Material properties obtained from www.matweb.com.

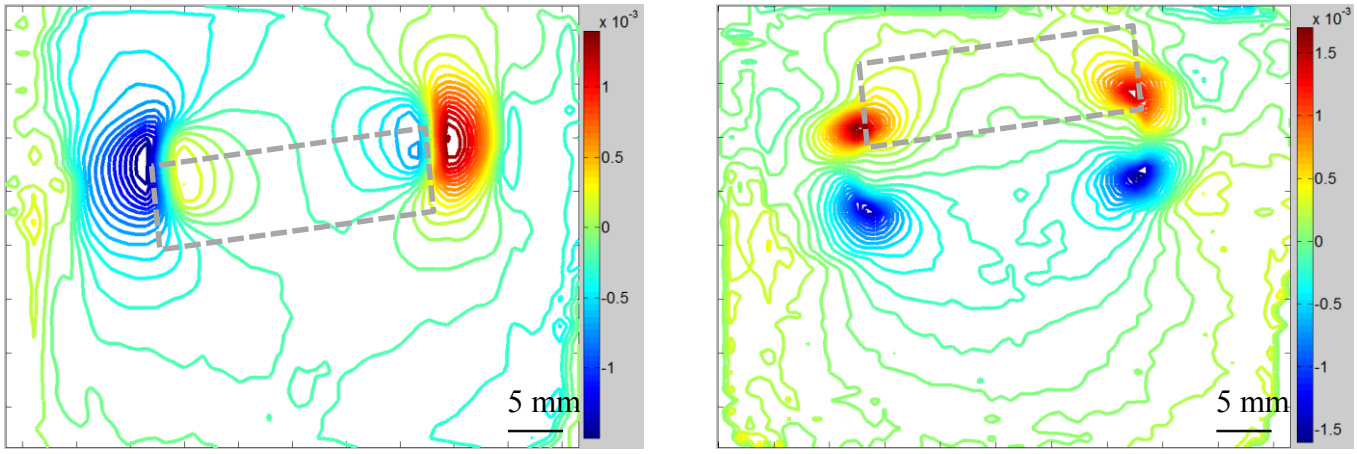

Figure 4.11: Surface slope contours $\frac{\partial w}{\partial x}$ (left) and $\frac{\partial w}{\partial y}$ (right) due to 15 minutes of thermal excitation and 5 minutes of cool-down. Delamination zone is highlighted in the figure by the gray dotted rectangle.

4.4 Measurement of flip-chip silicon-die deformations

Next, measurement of surface deformations of a silicon die attached to a ceramic substrate through 3600 solder balls was performed using r-DGS. The dimensions of silicon die were 20 x 20 mm^2. The silicon die surface was made specularly reflective (Figure 4.13 (left)) from a diffusively reflective (right) state by hand polishing the surface using diamond paste (6 µm grain size). Again thermal excitation method was used to measure the surface gradients. The schematic of the experimental setup used is shown in Figure 4.12. The ceramic die backing was clamped along its bottom edge using a screw clamp and the die face to be inspected was held vertically, facing the camera of the r-DGS setup. A heating (incandescent) lamp was placed at approximately 70 mm to illuminate the backside of the substrate. First, a reference speckle image of the target was captured with the heating lamp turned off (before heating). Next, the die is subjected to heating for a time period of 15 minutes raising the temperature of air on the backside by approximately 5 degree C. A second image was captured after the lamp was turned-off for approximately 5 minutes.

The speckle images recorded in the reference and deformed states of the Si die are shown in Figure 4.14. By correlating the two speckle images as described earlier, surface slope contours were obtained. In these experiments, the speckle images were segmented into 20 x 20 pixel (one pixel covered 29 μm) subsets with 15 overlapping pixels during image correlation. Figure 4.15 shows the resulting surface slope contours for the die due to thermal loading. From the surface gradient contours it can be seen that full field measurements of surface slopes can be made on the silicon die. The surface slopes in the horizontal direction ($\frac{\partial w}{\partial x}$) show a zero-contour approximately coinciding with the vertical line of symmetry of the silicon die and the magnitude of slopes monotonically and linearly varying in the horizontal direction along the horizontal line of symmetry as evident by equi-spaced contours. The contours along the edges tend to curve, possibly due to edge effects.

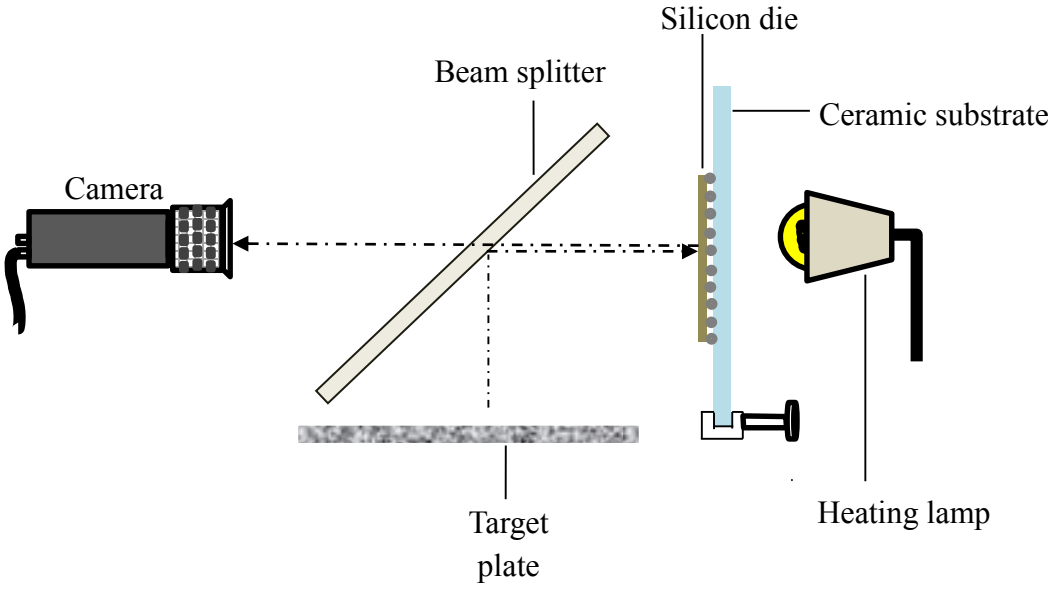

Figure 4.12: Schematic of the experimental setup deformation measurement on the silicon die.

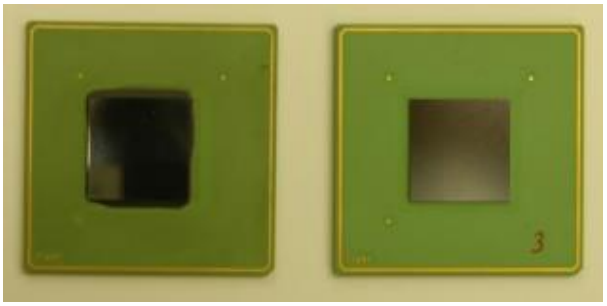

Figure 4.13: Flip-chip silicon die on ceramic substrate. Specularly reflective surface (left) after polishing and diffusively reflective surface (right) supplied by the manufacturer.

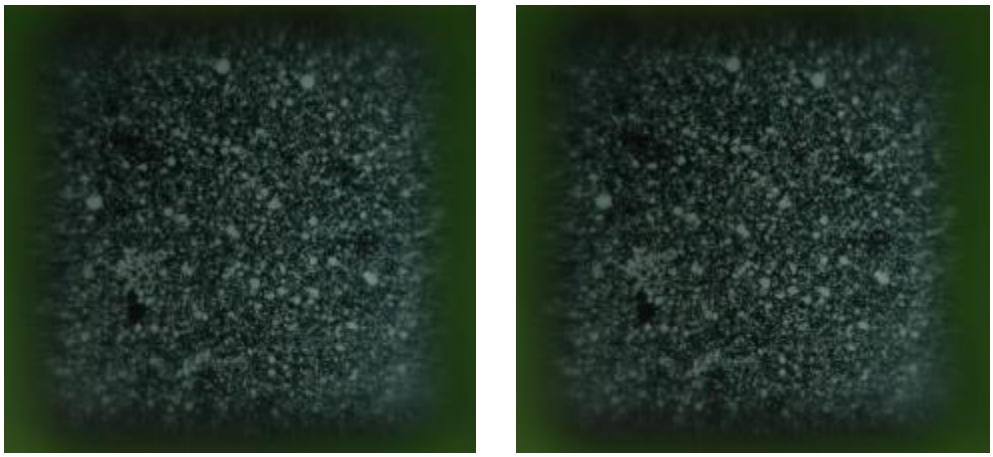

Figure 4.14: Reference (left) and deformed (right) speckle images. Deformed image (right) corresponds to image captured after 15 minutes of thermal excitation.

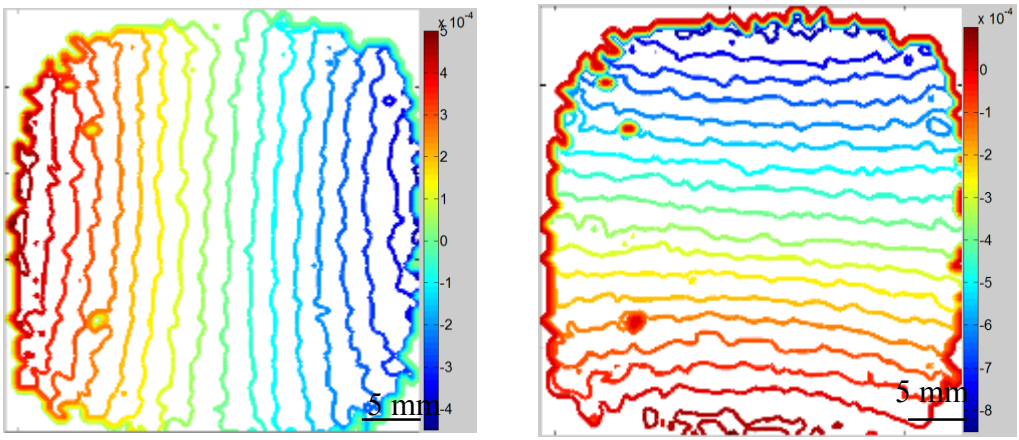

Figure 4.15: Surface slope contours $\frac{\partial w}{\partial x}$ (left column) and $\frac{\partial w}{\partial y}$ (right column) after 15 minutes of thermal excitation on the backside of the die assembly.

The surface slopes contours representing $\frac{\partial w}{\partial y}$ are again equally spaced. However, as a result of clamping the flip-chip assembly using a screw clamp at the bottom of the sample, surface slope contours are monotonically varying in the *y*-direction, possibly due to a rigid rotation of the entire assembly about the clamp axis when heated.

Chapter 5 : Mapping Quasi-Static Crack Tip Deformations

Measurement of fracture parameters in general and stress intensity factors in particular plays an important role in characterizing failure of a structural component. This chapter presents the feasibility of r-DGS for visualizing and quantifying crack tip deformations under quasi-static loading conditions. Both symmetric crack opening (mode-I) and combined crack opening and in-plane shear (mode-I + mode-II) deformations are examined. The focus here is on experimental setups and procedures for implementing r-DGS method for studying fracture problems, performing optical measurements and extracting crack-tip stress intensity factors.

5.1 Experimental details

Quasi-static 3-point bend experiments were performed on edge notched PMMA specimens using r-DGS. A specimen dimension of 130 x 60 x 8.9 mm^3 was used for both mode-I and mixed-mode loading configurations. An initial crack of length 12 mm as shown in the Figure 5.1(a) was used for mode-I loading and an initial crack of 12 mm oriented at 45^0 (Figure 5.1(b)) was used for mixed-mode testing. The specimen resting on two smooth anvils (120 mm span) was loaded in a displacement controlled mode (cross-head speed = 0.005mm/sec) using an Instron 4465 universal testing machine. One of the faces of the PMMA specimen was deposited with a thin layer of alum-

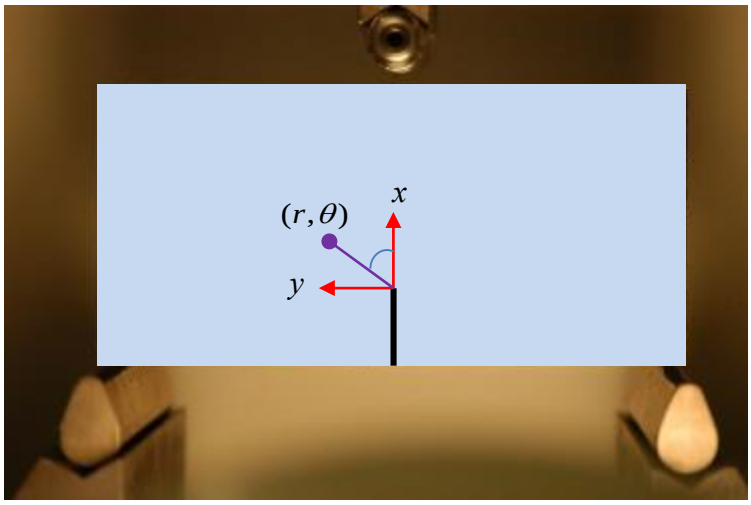

(a)

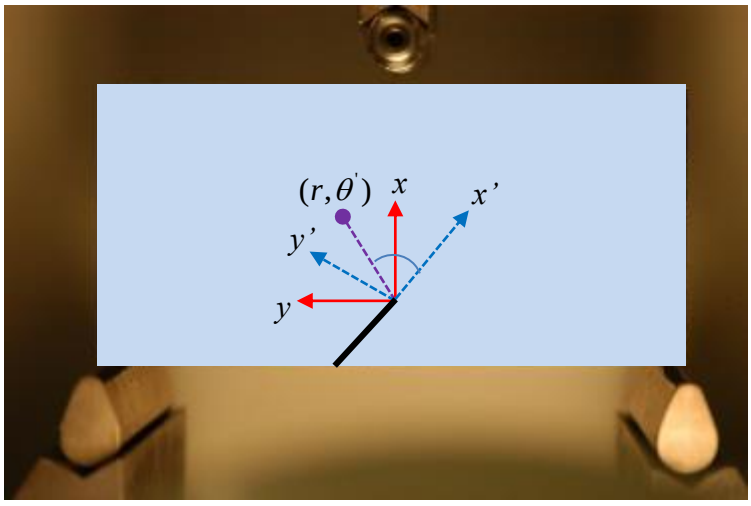

(b)

Figure 5.1: Specimen configurations for crack tip deformation measurement: (a) mode-I loading. (b) mixed-mode loading.

inum (a few nanometers thick) using vacuum deposition to obtain a specularly reflective surface. A 50/50 beam splitter was positioned between the specimen and the camera at an angle of 45^{o} to the optical axis of the camera (see Figure 5.3). A target plate spray painted with alternate mists of black and white paint to obtain random speckle pattern was placed at 45^{0} to the beam splitter.

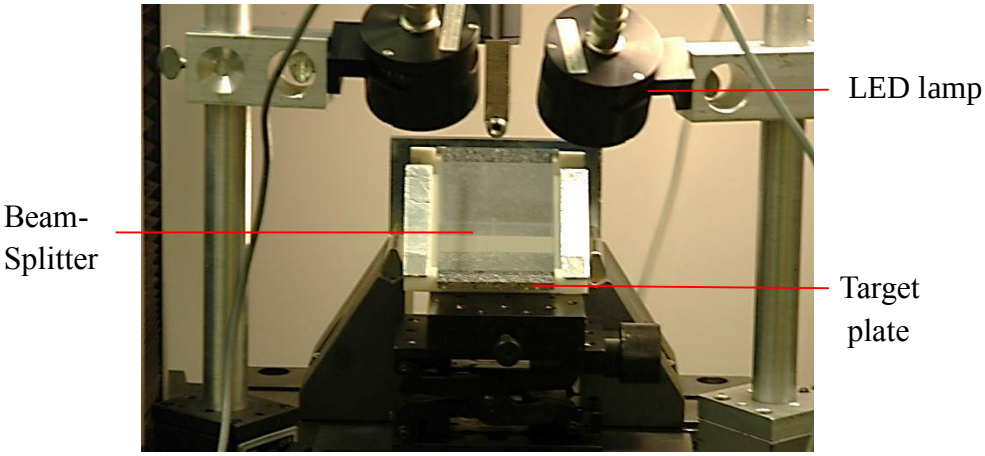

Figure 5.2: Experimental setup used for measuring angular deflections of light rays caused by a mode-I crack in a planar transparent 3-point bend specimen subjected to quasi-static loading.

The normal distance between the specimen surface and the speckle plane was $(\Delta =)65\,\text{mm}$. Using this optical arrangement, the camera was focused on the speckles via the specular specimen surface. The target plate was marked with a few reference points to obtain scale factor for relating the image dimensions with the actual specimen dimensions. A Nikon D100 digital SLR camera fitted with 28-300 mm focal length macro lens was placed in front of the specimen at a distance of ~1150 mm. To achieve a good focus on the speckles the camera also used with an adjustable extension tube. Lowest possible aperture size ($F^{\#}$ = 32) was selected to achieve good focus. The target plate was uniformly illuminated by using two LED lamps. A reference image was recorded using a camera resolution of 1504 × 1000 pixels (one pixel covered 28.06 μm on the target for mode-I experiments and 31.06 μm for mixed-mode experiments) in the no-load state. During the experiment, speckle images were recorded every 5 seconds once using time-lapse photography at different load levels representing the deformed state of the specimen. Due to deformations near t-

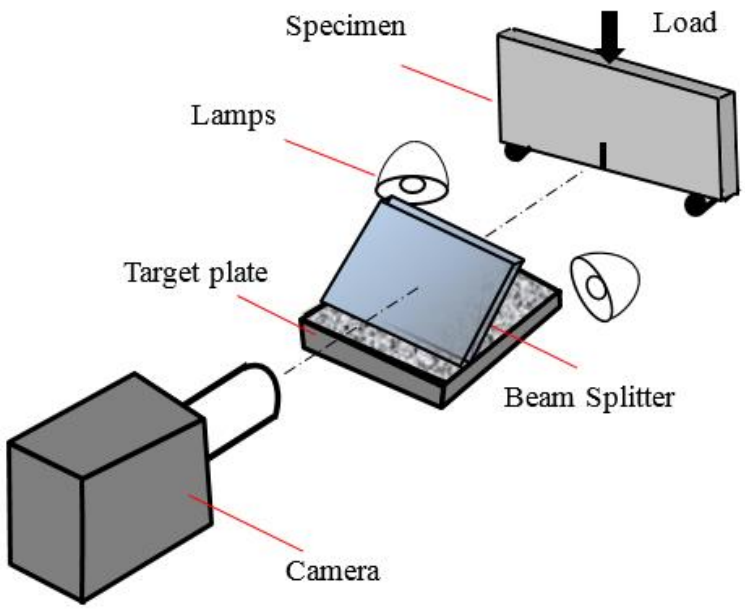

Figure 5.3: Schematic of the experimental setup to measure crack-tip deformations.

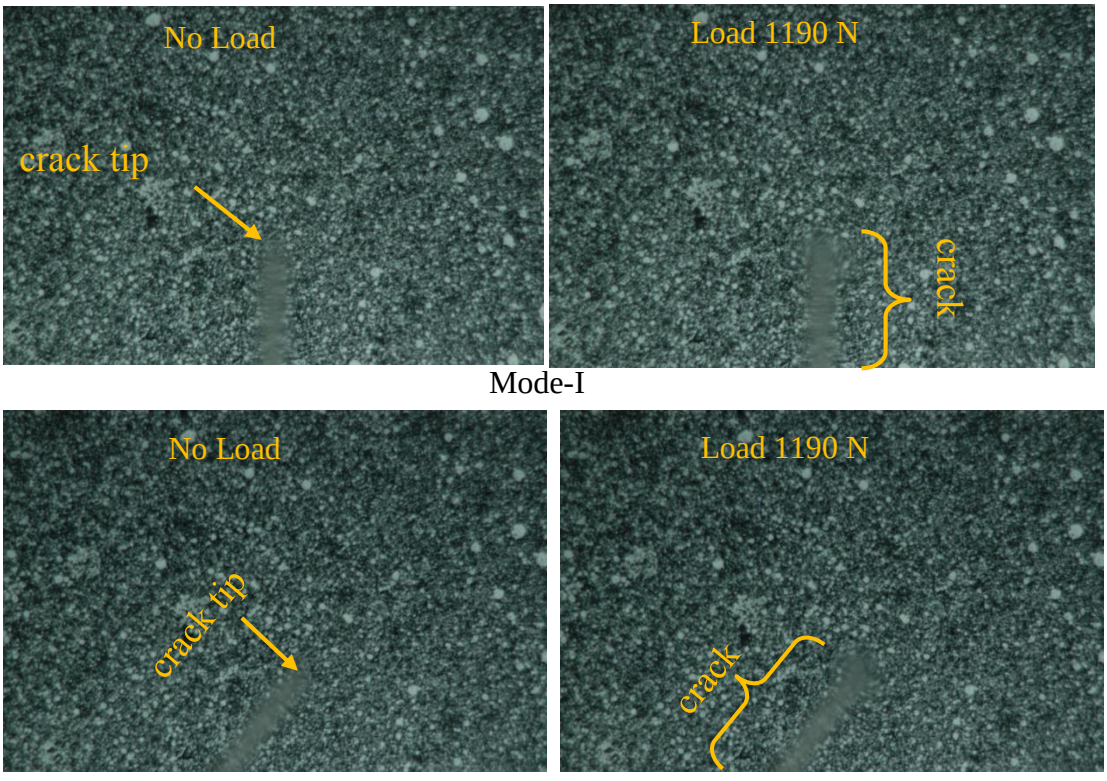

Figure 5.4: Representative speckle images recorded during quasi-static tests using r-DGS setup. Mode I image covers (42 x 28 mm^2), and mixed-mode image covers (46.5 x 31 mm^2).

he crack tip vicinity, the reflected light rays carry information pertaining to the change in surface slopes relative to the reference state. Using 2D digital image correlation method, the angular deflection fields representing ϕ_x and ϕ_y were obtained by correlating images corresponding to the deformed state with the one from the reference state. The images were divided into 15×15 pixel sub-images with 5 pixel overlap during image correlation. This resulted in an array of 297×196 data points, one for each sub-image, for subsequent analysis. A representative speckle image recorded for both mode–I and mixed-mode loading configuration is as shown in the Figure 5.4.

Figure 5.5 shows the resulting contours representing surface slopes near the crack tip for different load levels. The contours represent surface slopes $\frac{\partial w}{\partial x}$ (left column) and $\frac{\partial w}{\partial y}$ (right column) where *w* is the displacement in the out-of-plane (*z*) direction. The contour lines adjacent to the crack faces appear smeared due to unavoidable edge effects.

5.2 Static mode-I

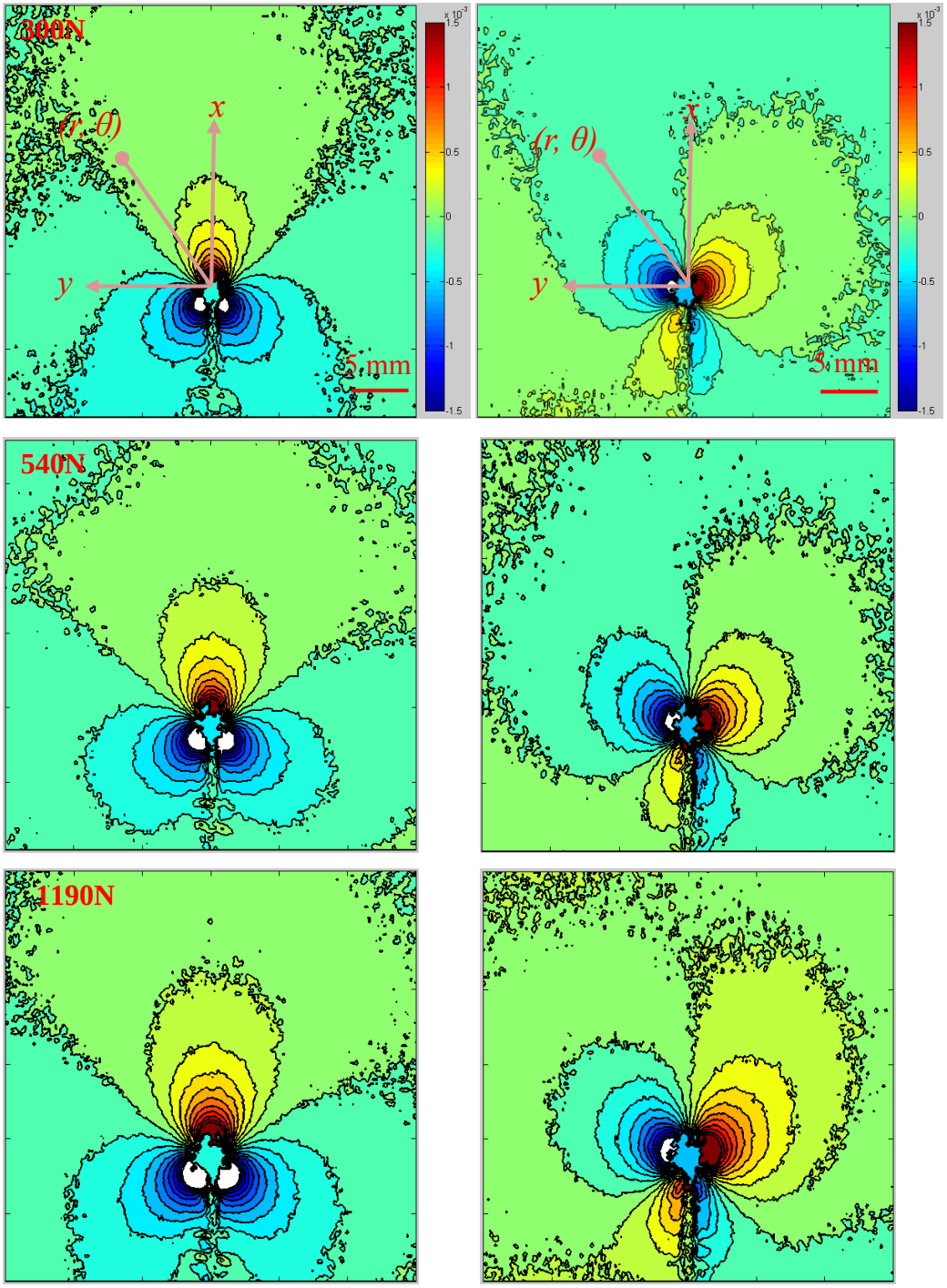

Figure 5.5: Experimentally measured contours of angular deflections of light rays ϕ_x (left) and ϕ_y (right) in the crack tip vicinity for different load levels. Contours are plotted every 15 x 10^{-5} radian.

5.3 Extraction of mode-I stress intensity factors using least-squares regression analysis

From William's asymptotic stress field expansion for mode-I cracks, the in-plane gradients of out-of-plane displacement (or angular deflection) can be expressed [21] as,

$$\begin{aligned}\frac{\phi_x}{2} &= \frac{\partial w}{\partial x} = -\frac{\nu B}{2E}\sum_{N=1}^{\infty} A_N \left(\frac{N}{2}-1\right) r^{\left(\frac{N}{2}-2\right)} \cos\left(\frac{N}{2}-2\right)\theta, \\ \frac{\phi_y}{2} &= \frac{\partial w}{\partial y} = -\frac{\nu B}{2E}\sum_{N=1}^{\infty} A_N \left(\frac{N}{2}-1\right) r^{\left(\frac{N}{2}-2\right)} \sin\left(\frac{N}{2}-2\right)\theta,\end{aligned} \tag{5.1}$$

where elastic modulus $E = 3GPa$, Poisson's ratio $\nu = 0.35$, sample thickness B = 8.9 mm. In the above equation (r,θ) are the crack-tip polar coordinates and $A_1 = K_I\sqrt{\frac{2}{\pi}}$ with K_I being the mode-I stress intensity factor. In equation 5.1, if *K*–dominance is assumed to prevail in the crack tip vicinity, terms corresponding to $N > 1$ in Eq. 5.1 are neglected to get

$$\begin{aligned}\frac{\phi_x}{2} &= \frac{\partial w}{\partial x} = -\frac{\nu B}{2E}\left[\left(-\frac{A_1}{2}\right) r^{\left(-\frac{3}{2}\right)} \cos\left(-\frac{3\theta}{2}\right)\right], \\ \frac{\phi_y}{2} &= \frac{\partial w}{\partial y} = -\frac{\nu B}{2E}\left[\left(-\frac{A_1}{2}\right) r^{\left(-\frac{3}{2}\right)} \sin\left(-\frac{3\theta}{2}\right)\right].\end{aligned} \tag{5.2}$$

An overdeterministic regression analysis was performed from the measured angular deflection data using the above equations. The angular deflection values corresponding to the region around crack tip $(0.5 \le r/B \le 1.5)$ and an angular extent (-150° $\le \theta \le$ +150°) were used in the regression analysis. The region was chosen to minimize the triaxial effects near the crack tip [21] by limiting to regions rich in *K*-dominant data. The variation of stress intensity factors for

different load levels are plotted in the Figure 5.6. Error bars correspond to stress intensity factors obtained by choosing different crack tip locations in the regression analysis.

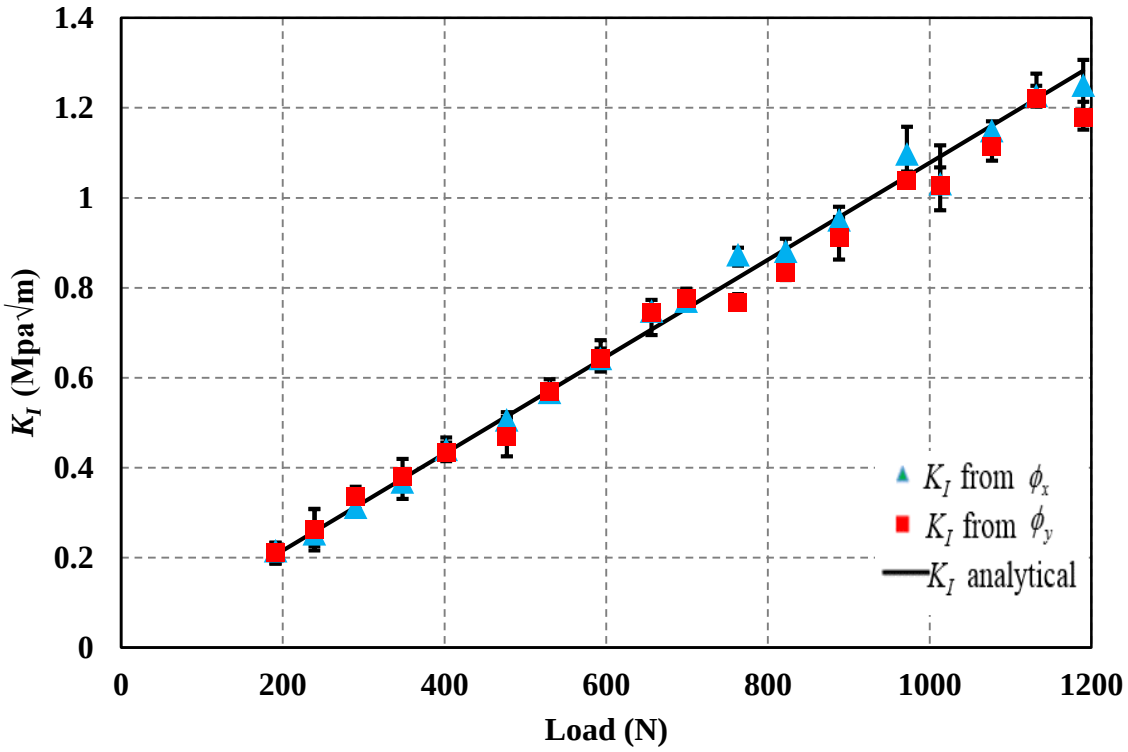

Figure 5.6: Variation of experimentally measured stress intensity factors (symbols) with applied load. The solid line represents stress intensity factors from boundary collocation solution for a static 3-point bend crack problem.

5.4 Comparison of measured data with analytical solution

The mode I stress intensity factors based on boundary collocation method is given by[37],

$$K_I = \frac{F \cdot S}{B \cdot W^{\frac{3}{2}}} \cdot \frac{3\left(\frac{a}{W}\right)^{\frac{1}{2}}\left[1.99 - \frac{a}{W}\left(1-\frac{a}{W}\right)\left\{2.15 - 3.93\left(\frac{a}{W}\right) + 2.7\left(\frac{a}{W}\right)^2\right\}\right]}{2\left(1+2\frac{a}{W}\right)\left(1-\frac{a}{W}\right)^{\frac{3}{2}}}, \qquad (5.3)$$

where F is the applied load, S is the distance between the supports, a is the initial crack length, and W is the specimen width. The stress intensity factors obtained from the above equation are plotted in Figure 5.6 for comparison with the estimated values based on regression analysis. Evidently the agreement between the analytical and experimental stress intensity factor is rather good, further validating the feasibility of the r-DGS method for fracture mechanics applications.

5.5 Mixed-mode crack tip deformations

Figure 5.7 shows r-DGS contours due to surface deformations near the mixed-mode crack tip. The measured orthogonal surface slopes for two load levels are shown using the global coordinate system x and y defined at the crack tip aligned with the loading direction and the specimen edges. The availability of two orthogonal slopes in the field of view offers flexibility to evaluate slopes in a rotated coordinate system aligned with the crack orientation, denoted by the coordinate system x' and y' in Figure 5.1(b). Accordingly, in this research, the orthogonal angular deflections of light rays and hence the respective surface slopes in the x' and y' directions were evaluated using the transformations,

$$\begin{aligned} \frac{\phi_x'}{2} &= \frac{\partial w}{\partial x'} = \frac{\partial w}{\partial x}\cos\alpha + \frac{\partial w}{\partial y}\sin\alpha \\ \frac{\phi_y'}{2} &= \frac{\partial w}{\partial y'} = \frac{\partial w}{\partial x}\left(-\sin\alpha\right) + \frac{\partial w}{\partial y}\cos\alpha \end{aligned} \qquad (5.4)$$

where α (= 45° in this work) is the crack orientation angle (Figure 5.1(b)). Figure 5.6 (second and fourth row) represents the surface slope contours after rotating them into the local coordinate system x' and y'.

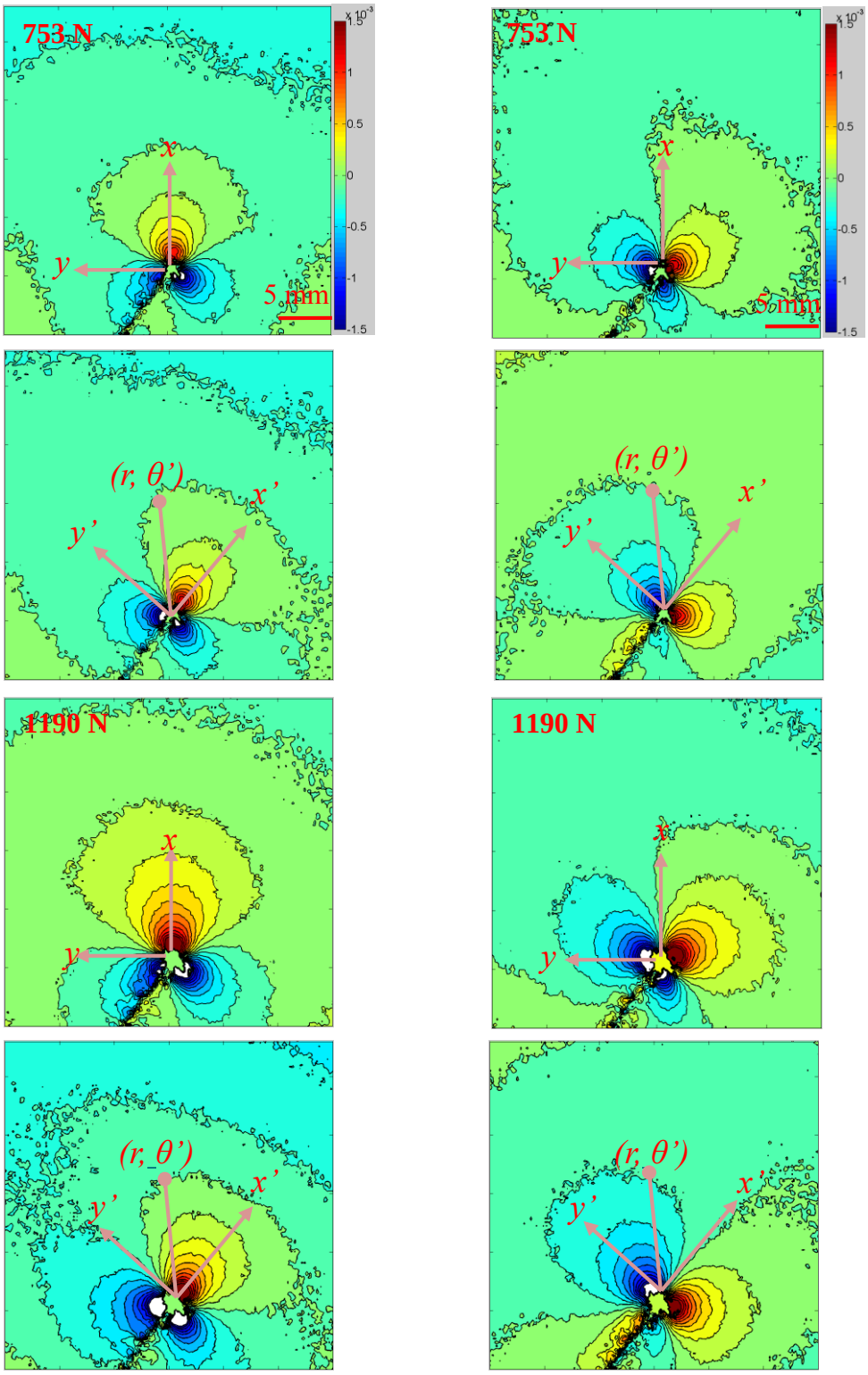

Figure 5.7: Contours representing surface slopes in the mixed-mode crack tip vicinity. The first row for both loads represents the slopes in local co-ordinates (x, y) and the second row represents slopes in local coordinates (x', y'). Contour increments 15 x 10^{-5} radians.

5.6 Extraction of mixed-mode stress intensity factors

The asymptotic expansion for in-plane surface slopes due to out-of-plane crack tip displacements for mixed-mode loading condition is obtained by superposing the mode-I and mode-II fields [38],

$$\frac{\phi_x^{'}}{2}=\frac{\partial w}{\partial x^{'}}=\frac{-\nu B}{2E}\left[\begin{array}{l}\left\{\sum_{N=1}^{\infty}\left(A_N(\frac{N}{2}-1)r^{((\frac{N}{2})-2)}\cos(\frac{N}{2}-2)\theta^{'}\right)\right\}+\\ \left\{\sum_{N=1}^{\infty}\left(B_N(\frac{N}{2}-1)r^{((\frac{N}{2})-2)}\sin(\frac{N}{2}-2)\theta^{'}\right)\right\}\end{array}\right]$$

$$\frac{\phi_y^{'}}{2}=\frac{\partial w}{\partial y^{'}}=\frac{-\nu B}{2E}\left[\begin{array}{l}\left\{\sum_{N=1}^{\infty}\left(A_N(\frac{N}{2}-1)r^{((\frac{N}{2})-2)}\sin(\frac{N}{2}-2)\theta^{'}\right)\right\}+\\ \left\{\sum_{N=1}^{\infty}\left(B_N(\frac{N}{2}-1)r^{((\frac{N}{2})-2)}\cos(\frac{N}{2}-2)\theta^{'}\right)\right\}\end{array}\right] \quad (5.5)$$

where $(r,\theta^{'})$ are polar coordinates centered at the crack tip in the local coordinates *x'* and *y'* with $\theta^{'}=\theta+\alpha$ ($\alpha=-45^0$ is the crack orientation angle), elastic modulus $E=3$ GPa, Poisson's ratio $\nu=0.35$, thickness *B* = 8.9 mm and $A_1=K_I\sqrt{\frac{2}{\pi}}$ with K_I being the mode-I stress intensity factor and $B_1=K_{II}\sqrt{\frac{2}{\pi}}$, K_{II} being the mode-II stress intensity factor. A two term solution (*N* = 3) was used to extract the stress intensity factors and was found to capture the overall behavior of a mixed-mode crack well. The results thus obtained are plotted in Figure 5.8 for different load levels. The error bars are due to the variation in the selection of crack tip location during regression analysis.

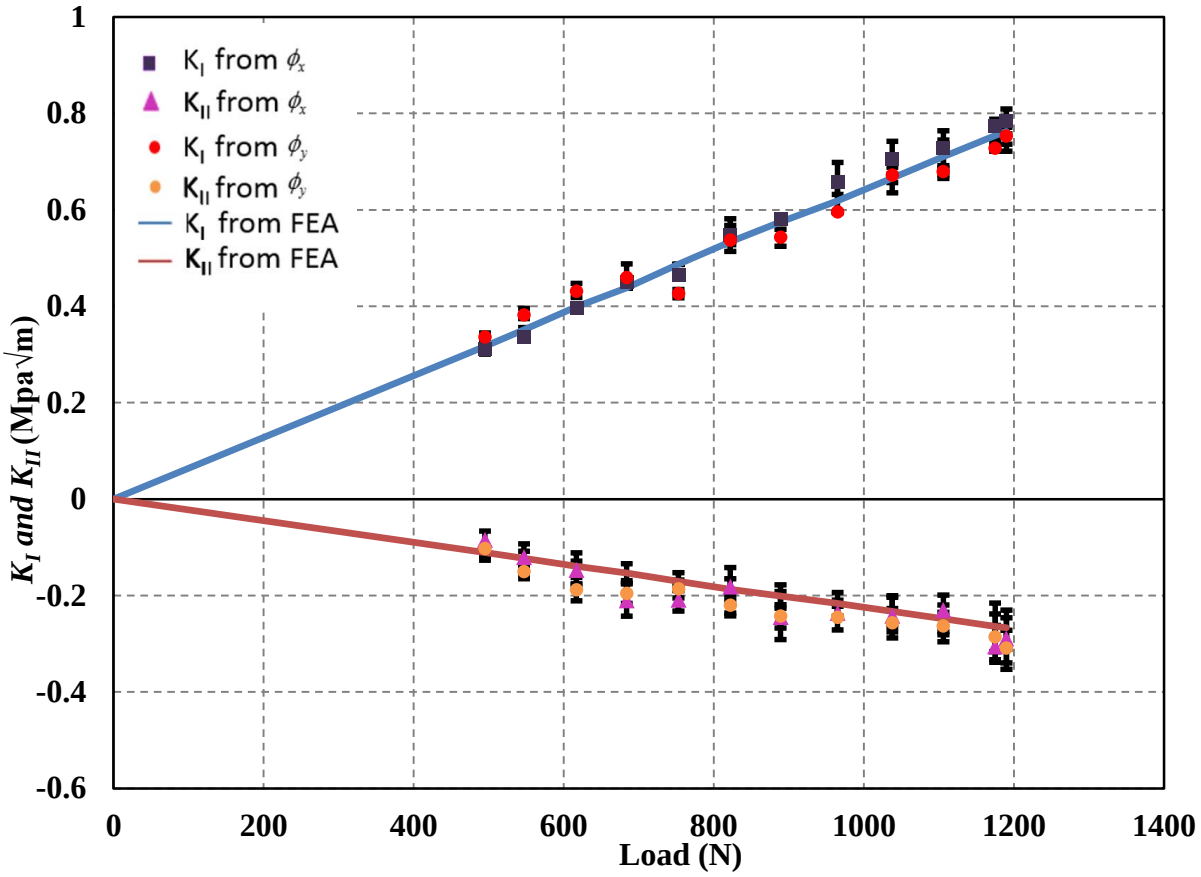

Figure 5.8: Comparison of mixed-mode stress intensity factors from r-DGS and finite element simulation.

5.7 Finite element analysis

A finite element analysis was carried out using ABAQUS™ software package to complement experimental results in the absence of closed form solution. The finite element model shown in Figure 5.9 consists of 23269 eight-node plane stress elements. The crack tip region was discretized using a fine mesh with the crack tip element size as small as $0.01a$ (a crack length). The mesh near the crack tip is as shown in the Figure 5.8. No special attempt was made to create singularity at the crack tip by using special elements. An elastic modulu $E = 3$ GPa, Poisson's

ratio $\nu = 0.35$ were used in the simulation. The analysis was carried out at different load levels corresponding to experimentally measured values and the crack opening and crack sliding displacements were used to obtain the stress intensity factors for different load levels. The crack

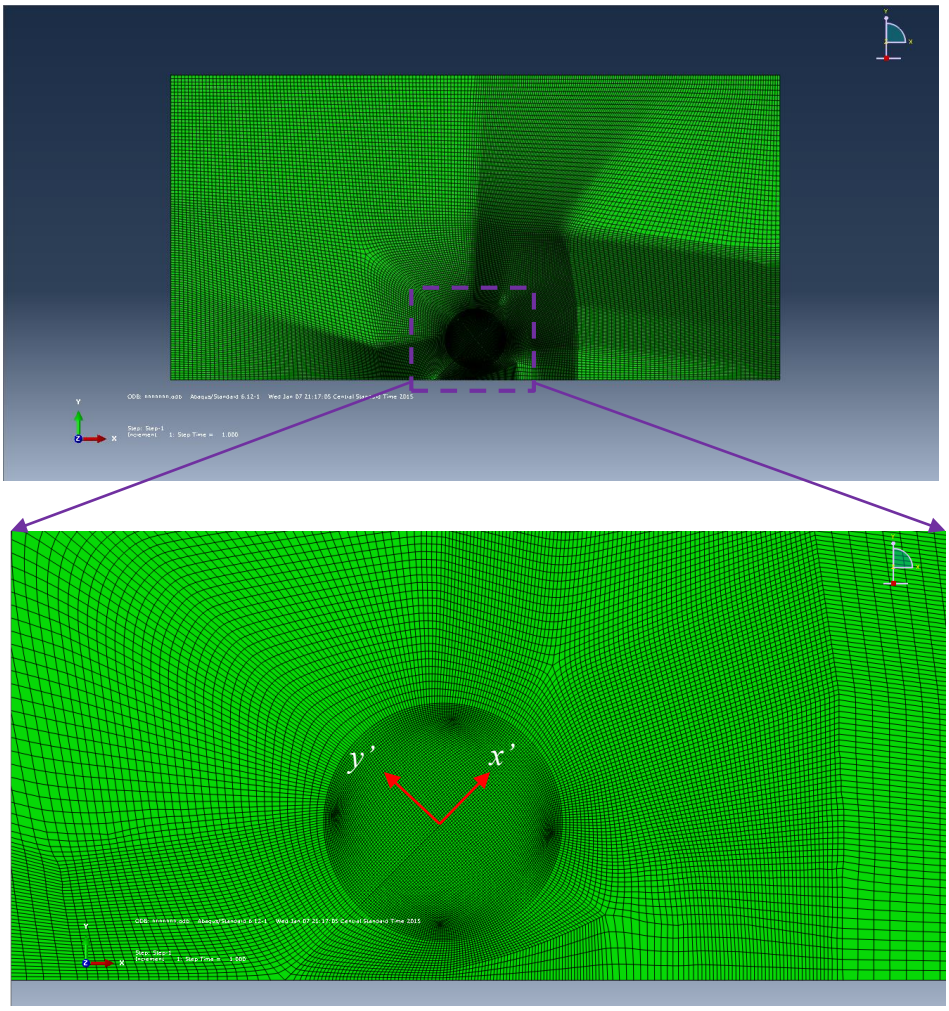

Figure 5.9: Finite element model for mixed-mode crack tip analysis. Enlarged view of the mesh near the crack tip is shown.

opening and sliding displacements from the finite element model were output in the local coordinate system *x'* and *y'*. Mode-I and -II stress intensity factors were estimated by performing regression analysis of these values using[39],

$$K_I = \frac{E\sqrt{2\pi}}{8\sqrt{r}}\left(u_{2-upper} - u_{2-lower}\right)\Big|_{(r,\theta=\pi)}$$
$$K_{II} = \frac{E\sqrt{2\pi}}{8\sqrt{r}}\left(u_{1-upper} - u_{1-lower}\right)\Big|_{(r,\theta=\pi)} \qquad (5.7)$$

where u_2 is the crack face opening displacement and u_1 is crack face sliding displacement at a node along the upper and lower crack faces. The linear region of K_I and K_{II} were extrapolated in the K_I and K_{II} vs radius plot to obtain the stress intensity factor at the crack tip [40]. Figure 5.10 and 5.11 show the variation of stress intensity factors along the distance from the crack tip. The apparent stress intensity factors are extrapolated to obtain the actual stress intensity factors which are as shown in the figures.

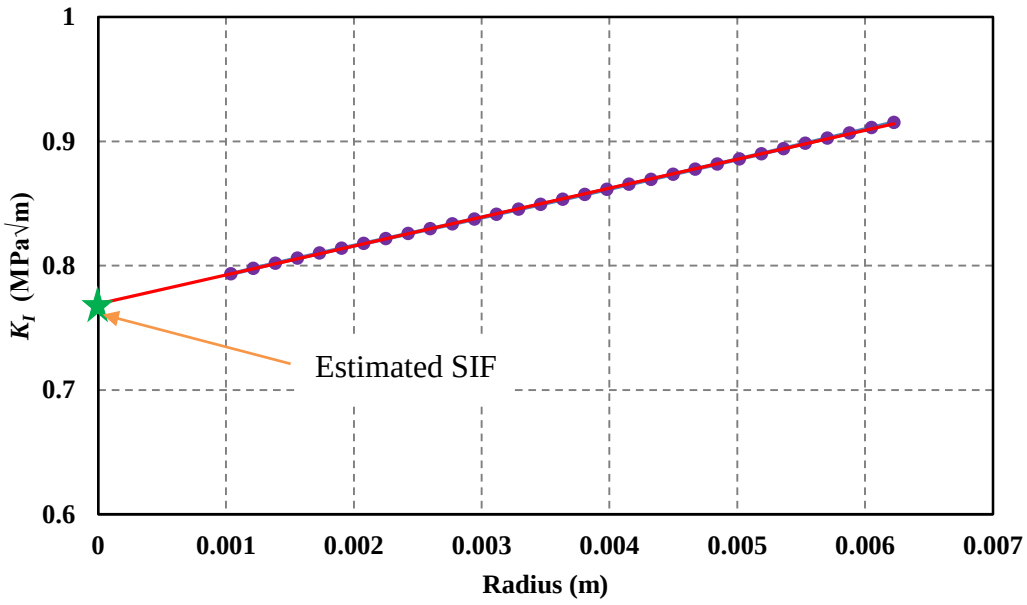

Figure 5.10: Evaluation of mode-I stress intensity factor using crack opening displacement from FEA for an applied load of 1190 N.

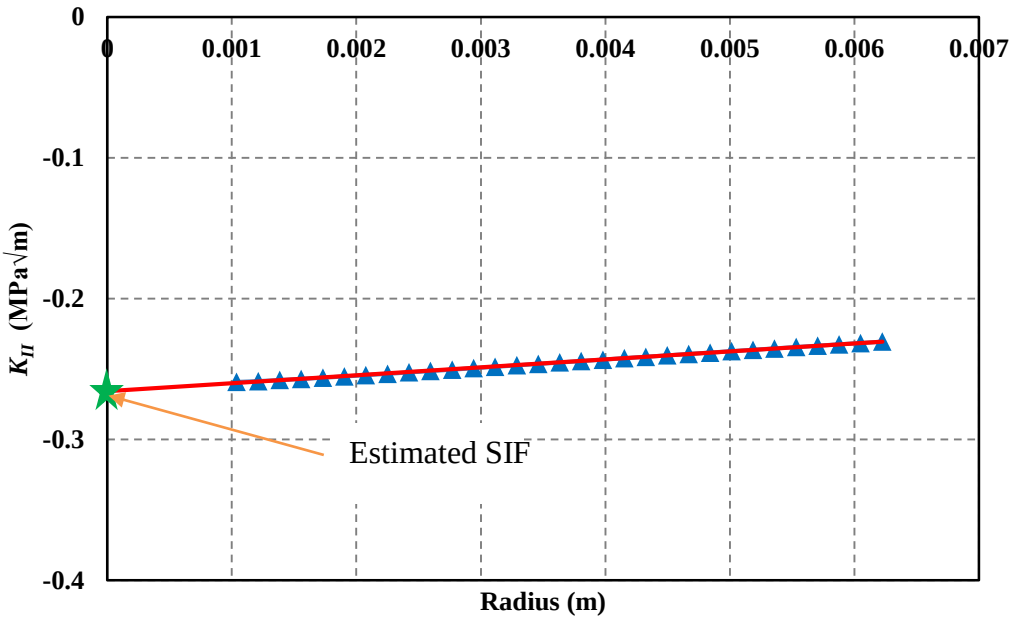

Figure 5.11: Evaluation of mode-II stress intensity factor using crack sliding displacement from FEA at an applied load of 1190 N.

Figure 5.8 shows the variation of stress intensity factors for different load levels corresponding to the experimentally measured load. A good agreement is evident from the plot between the two, supporting the feasibility of r-DGS for studying mixed-mode fracture problems.

Chapter 6 : Crack-Tip Deformation Measurements: Dynamic Case

This chapter describes measurement of the crack tip deformations when a cracked specimen is subjected to mode-I and mixed mode (mode I + mode II) dynamic loading conditions. An ultrahigh-speed camera was used to record speckle images as done in the plate impact example in the previous chapter. The stress intensity factor histories are obtained from the measured surface slopes near the crack tip and compared with a companion elasto-dynamic numerical simulation until crack initiation.

6.1 Experimental details

The crack tip deformations under mode I and mixed-mode (mode I + mode II) for an edge notched PMMA specimen due to stress wave propagation were performed using a long-bar setup used in conjunction with high-speed photography and r-DGS. The schematic of the experimental setup is as shown in the Figure 6.1. The loading device consisted of an aluminium 7075-T6 long-bar (25.4 mm diameter and 2 m long) with a bull-nose head, a compressed air chamber and a high-speed digital image acquisition system. The long-bar was aligned with the barrel of a gas-gun containing a 305 mm long, 25.4 mm diameter aluminum cylindrical striker. The crack tip deformation event was photographed using a Cordin 550 high-speed digital camera equipped with 32 CCD sensors and two high-energy flash lamps to illuminate the speckle pattern on the target

plate. A 50/50 beam splitter positioned between the lens and the specimen at an angle of 45^0 was used to view the speckle pattern on the target via the reflective face of the specimen. Other experimental parameters such as framing rate, flash duration and image storage was managed with the help of a computer connected to the camera. The bull-nose tip of the long-bar was registered against the edge of an edge notched PMMA specimen of dimensions 130 x 60 x 8.9 mm^3 for both mode I and mixed-mode loading conditions. The notched specimens were rested on an adjustable platform between two strips of (2 mm thick) soft putty at the top and bottom faces (60 x 8.9 mm^2) to approximately simulate 'free-free' conditions. For mode-I loading the tip of the long-bar was aligned in-line with the edge notch whereas for the mixed-mode loading case an eccentricity of 20 mm with respect to the crack line and the tip of the long-bar. One of the faces of the specimen was made specularly reflective by sputter coating a layer of aluminium using a vacuum chamber. The loading was initiated by releasing the compressed air from the gas chamber which propelled the striker situated initially in the barrel. A compressive stress wave was initiated in the long-bar as the accelerating striker impacts the long-bar, and the stress wave travelled the length of the bar before imparting a transient line-load to the edge of the specimen.

A strain gage (CAE-13-125UN-120 from Vishay Micro-Measurements, Inc) bonded to the long-bar was used to measure the strain history in the bar during impact loading. The strain measurements were done using a Lecroy oscilloscope and an Ectron signal amplifier/conditioner[41] with a quarter Wheatstone bridge circuit. As soon as the striker contacted the long-bar, an electrical circuit was completed and with the help of a pre-set delay using a delay generator, the high-speed camera was triggered to capture speckles on the stationary target plane via the specimen surface during stress wave propagation. Particle velocity of the long-bar was subsequently calculated using the strain history measured from the oscilloscope. The distance

between the target plate and specimen was (Δ) 102 mm and the distance between the camera lens and the specimen was ~715 mm.

To carry out the digital image correlation process, a set of 32 reference images (one image corresponding to each CCD sensor of the Cordin camera) prior to crack tip deformation was captured by operating the camera at 150,000 frames per second. Next the camera was triggered

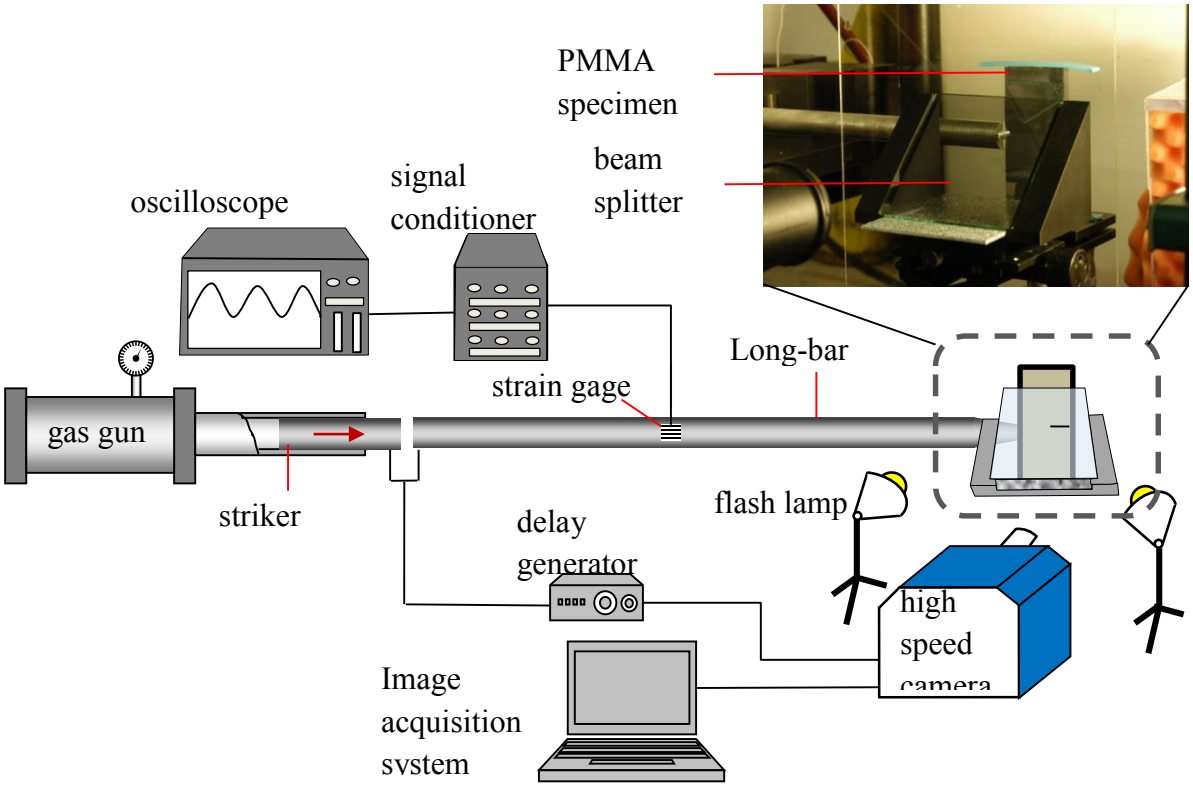

Figure 6.1: Schematic of the experimental setup used in the dynamic mode-I fracture study. Inset is the photograph showing the close up view of the experimental arrangement.

with a pre-set delay as the striker contacted the long bar. A set of 32 speckle images while the specimen was undergoing deformation was captured at the same framing rate. A set of speckle images recorded during mode-I and mixed-mode dynamic fracture experiment is shown in Figure 6.3 and 6.4. These images show speckle recordings corresponding to time instants before and after

crack initiation with corresponding time stamps relative to the image with initial visible crack tip deformation. In these images, the current location of the crack tip can be evidenced by a visible smear in the discernibility of speckles.

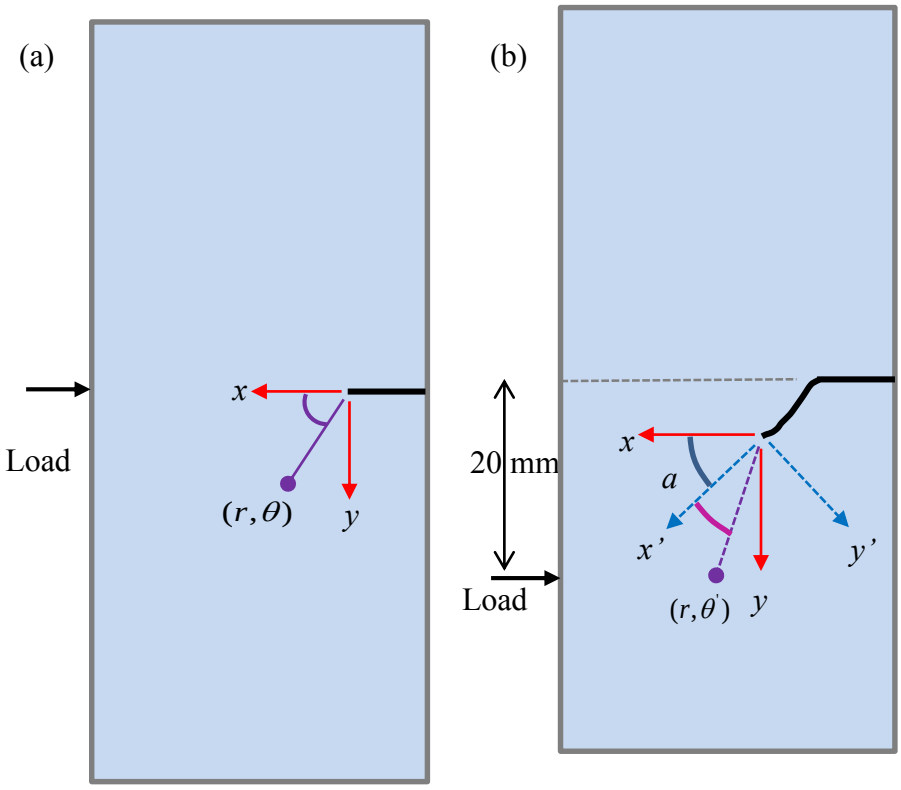

Figure 6.2: Specimen loading configuration (a) Global crack tip coordinates (b) Global and local crack-tip coordinates for mixed-mode crack propagation.

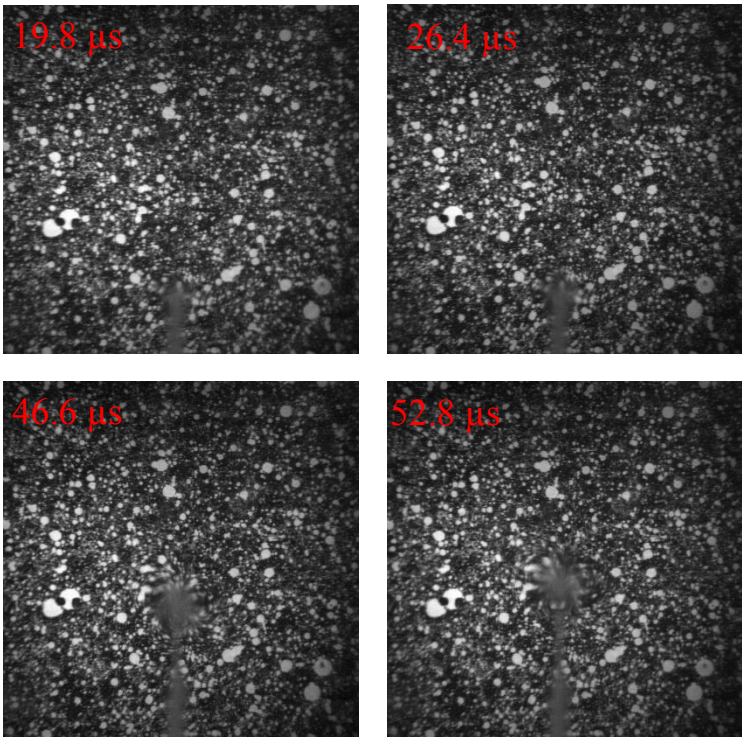

Figure 6.3: Speckle images captured for mode-I loading.

The deformed and undeformed image pairs corresponding to the same sensor of the high-speed camera were paired after the experiment and correlated using digital image correlation software ARAMIS to obtain orthogonal displacements δ_x and δ_y on the target plane. These were subsequently converted into orthogonal angular deflection of light rays ϕ_x and ϕ_y in the *x*-*z* and *y*-*z* planes, respectively, and the surface slopes $\frac{\partial w}{\partial x}$ and $\frac{\partial w}{\partial y}$ on the specimen plane. The image correlation was carried out using a sub-image size of 15 x 15 pixels (one pixel covered 36.1 µm on the target for mode-I experiments and 34.8 µm for mixed-mode experiments) with 5 pixels overlap for during analysis.

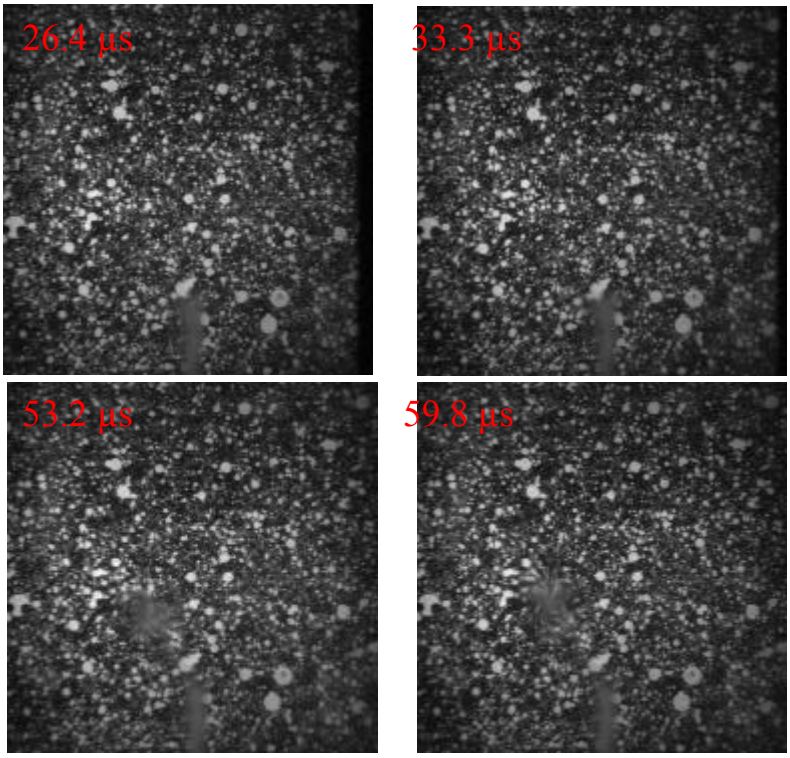

Figure 6.4: Speckle images captured for mixed-mode loading.

6.2 Mode I fracture results

Figure 6.5 shows the surface slopes around the dynamically loaded mode-I crack. The first row of images corresponds to pre crack initiation state and the last two rows correspond to post crack initiation regime. Following crack initiation, it can be seen that the crack travels in the initial notch direction without any kink resulting from a symmetric far-field loading condition. These contours show qualitative similarity with those for the static mode-I experiments shown in Figure 5.4. The contour lines adjacent to the crack tip are lost due to a combination of diffraction effects, the numerical aperture of the camera used and the large deformations limiting the correlation of speckles.

6.3 Extraction of mode-I stress intensity factor history

The expressions for surface gradient fields corresponding to a steadily propagating crack in an elastic planar solid are given by [21, 42],

$$\frac{\phi_x(t)}{2}=\frac{\partial w(t)}{\partial x}=\frac{-\nu B}{2E}\left[\begin{array}{l} f(V;C_L;C_S)\left\{\left(A_1(t)(\frac{N}{2}-1)r^{((\frac{N}{2})-2)}\cos(\frac{N}{2}-2)\theta\right)\right\} \\ +\sum_{N=2}^{\infty}\left(A_N(t)(\frac{N}{2}-1)r^{((\frac{N}{2})-2)}\cos(\frac{N}{2}-2)\theta\right)\end{array}\right] \qquad (6.1)$$

$$\frac{\phi_y(t)}{2}=\frac{\partial w(t)}{\partial y}=\frac{-\nu B}{2E}\left[\begin{array}{l} f(V;C_L;C_S)\left\{\left(A_1(t)(\frac{N}{2}-1)r^{((\frac{N}{2})-2)}\sin(\frac{N}{2}-2)\theta\right)\right\} \\ +\sum_{N=2}^{\infty}\left(A_N(t)(\frac{N}{2}-1)r^{((\frac{N}{2})-2)}\sin(\frac{N}{2}-2)\theta\right)\end{array}\right]$$

where, E = elastic modulus of PMMA (5.8 GPa), f is a function of crack velocity V, dilatational and shear wave speeds C_L (2602 *m/s*)and C_S (1354 *m/s*) respectively and $A_1(t)=K_I(t)\sqrt{\frac{2}{\pi}}$ with $K_I(t)$ being the instantaneous mode-I stress intensity factor. Also, for plane stress conditions,

$$f(V;C_L,C_S)=\frac{\left(1+\alpha_S^2\right)\left(\alpha_L^2-\alpha_S^2\right)}{4\alpha_S\alpha_L-\left(1+\alpha_S^2\right)^2} \qquad (6.2)$$

where, $\alpha_{L:S}=\sqrt{1-\frac{V^2}{C_{L:S}^2}}$. The instantaneous crack length measured from the high-speed images and are shown in Figure 6.6. The crack velocity for the propagating crack was estimated by measuring the change in the crack length between successive images and dividing by the time interval between them (1/framing rate). The dilatational and shear wave speeds of the specimen were mea-

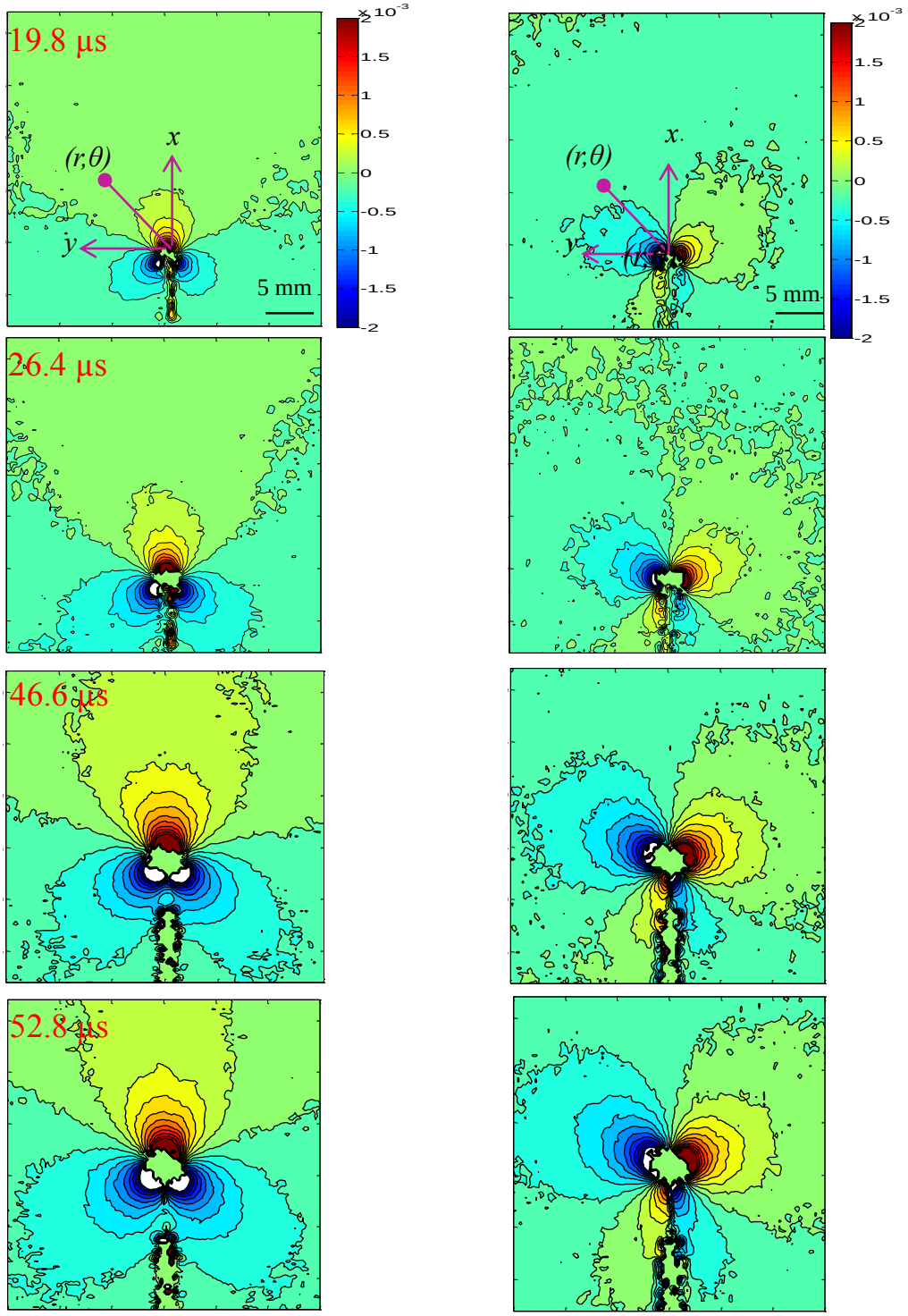

Figure 6.5: Experimentally measured ϕ_x (column 1) and ϕ_y (column 2) contours near the mode-I crack-tip at different time instants during dynamic impact. Contours are plotted in increments of 2 x 10^{-4} radians. Time *t=0* corresponds to instance just before crack tip deformation.

sured using ultrasonic pulse-echo measurements [43]. The surface gradient fields in the Eq. (6.1) were used to extract the dynamic mode-I stress intensity factor ($K_I(t)$) history by performing an overdeterministic regression analysis of the measured surface slopes in the crack tip vicinity. A two term expansion of surface slopes ($N = 3$) was found to capture the overall fracture behavior. As in the quasi-static case, data in the $\left(0.5 \le r/B \le 1.5\right)$ range and $(-150 \le \theta \le 150)$ were used in the regression analysis. The error bars in the Figure 6.7 correspond to variation of stress intensity factor due to different selection of the crack-tip location. The crack initiates at about 33.3 μs after impact and the mode-I stress intensity factor increases monotonically. (The figure also includes the stress intensity factors determined by a companion finite element simulation, to be discussed in the next section, up to crack initiation represented by the solid line.)

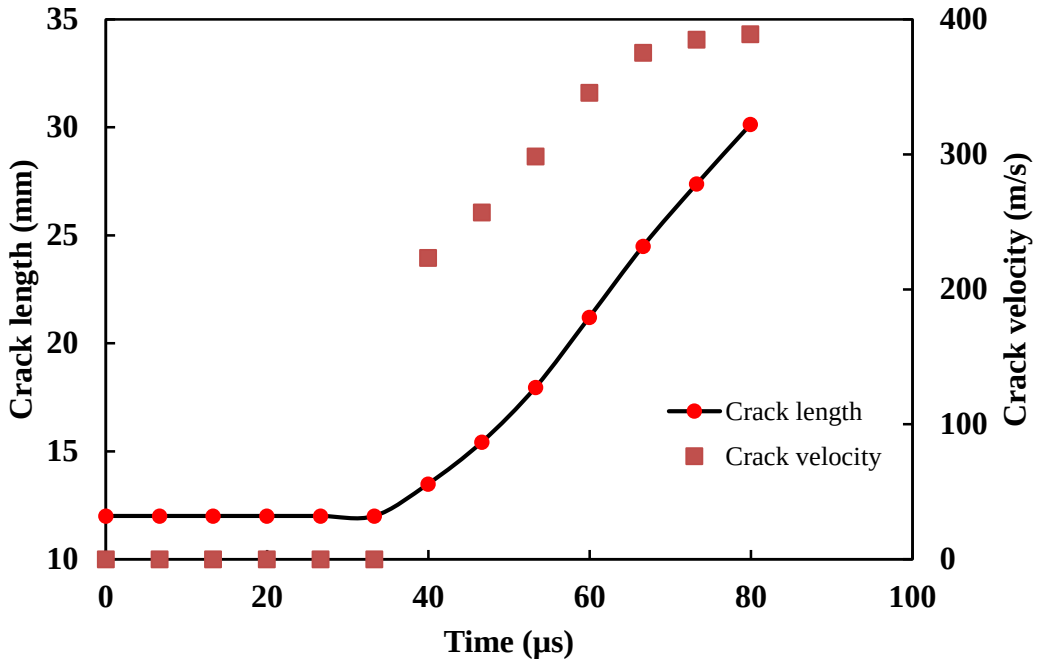

Figure 6.6: Crack growth and crack velocity history in edge cracked PMMA specimen subjected to mode-I loading.

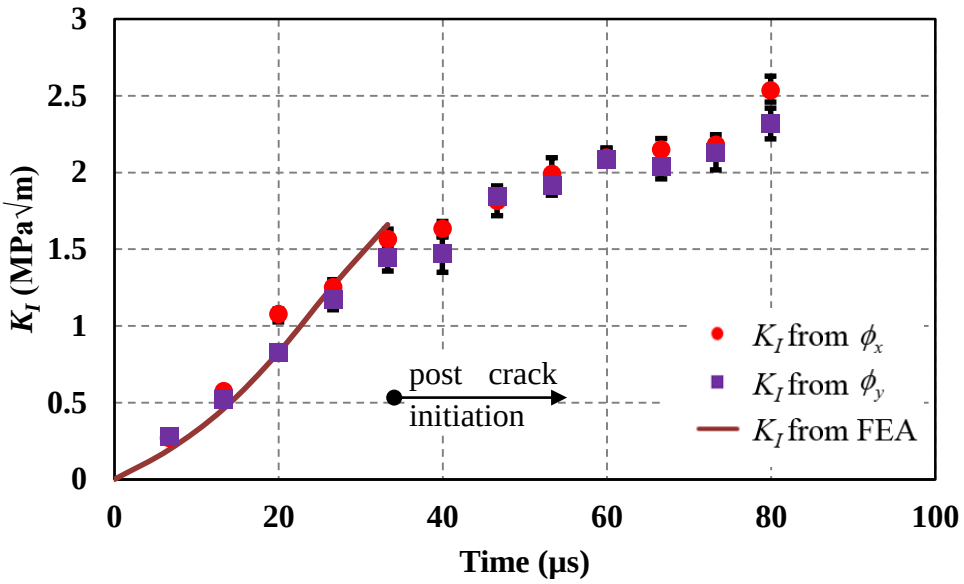

Figure 6.7: Dynamic mode-I stress intensity factor histories from over-deterministic regression analysis of surface gradient data. Solid line represents SIF histories from a companion elasto-dynamic finite element analysis based on measured impact velocity.

6.4 Finite element analysis

A companion 3D elasto-dynamic finite element simulation of the mode-I dynamic loading experiment was performed using ABAQUS™/Explicit software package. The simulation was limited to extracting dynamic stress intensity factors independently for a dynamically loaded stationary crack. The model included an edge cracked specimen and a long-bar as shown in the Figure 6.9 (left). The discretized finite element model consisted of 176,711 quadratic 3D stress elements (C3D10M) with a fine mesh near the crack tip having element size of 0.1 mm. The semicircular head of the long bar was aligned to be in contact (frictionless contact was defined between the two bodies) with the specimen along the edge opposite to the crack tip and the particle velocity measured from the strain history on the bar was input on the far end of the long-bar. The particle velocity on the long bar was obtained by,

$$V_p = C_{Al}\varepsilon \qquad (6.3)$$

where V_p = particle velocity of the long bar, C_{Al} = wave speed of the Al bar (5370 m/sec) and ε = measured strain history. The stress waves were transmitted into the specimen from the semicircular head of the long bar placed against the edge of the specimen. The time steps during the analysis were automatically controlled by the explicit integration scheme. The instantaneous mechanical fields including in-plane displacements were output at time instants corresponding to the framing rate used during experiments. Using these displacement fields, instantaneous mode-I stress intensity factor was calculated using the crack opening displacement of the upper face using[39],

$$K_I(t) = \frac{E\sqrt{2\pi}}{4\sqrt{r}} u_2(t); \quad (r, \theta = \pi) \qquad (6.4)$$

where E = 5.8 *GPa* is the dynamic elastic modulus [35] of PMMA and u_2 is crack opening displacement of nodes along the upper crack flank. A sample regression analysis for time instance $t=33.3\mu s$ is shown in the Figure 6.8. The stress intensity factor corresponding to the first measurable deformation from the finite element simulation near the crack faces is taken as the first time instant and the time instant previous to it is assigned as time $t=0$. In-plane displacements of the crack faces were requested every 6.6 μsec and the stress intensity factor corresponding to each time instance was evaluated and superimposed with the experimental data up to the crack initiation period as shown in the Figure 6.7. A good agreement can be seen between experimental and numerical solution.

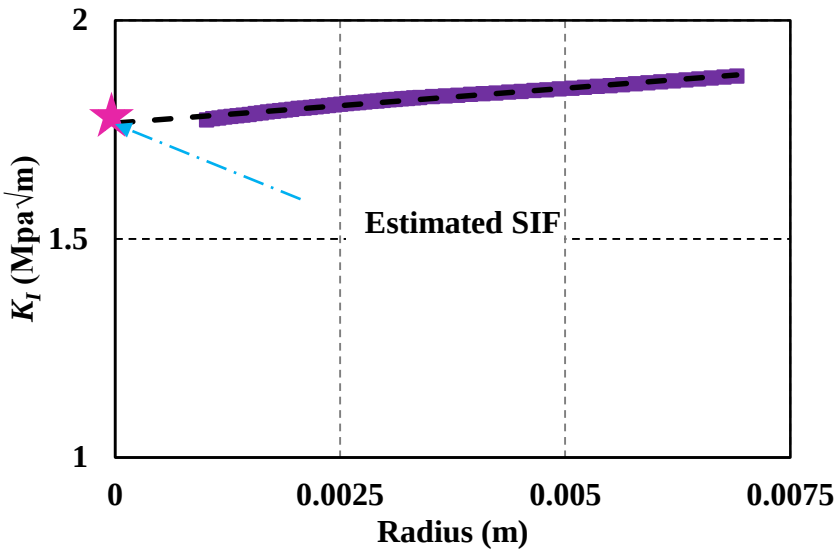

Figure 6.8: Evaluation of mode-I stress intensity factor using crack opening displacement from FEA for time instance *t=33.3 μs*.

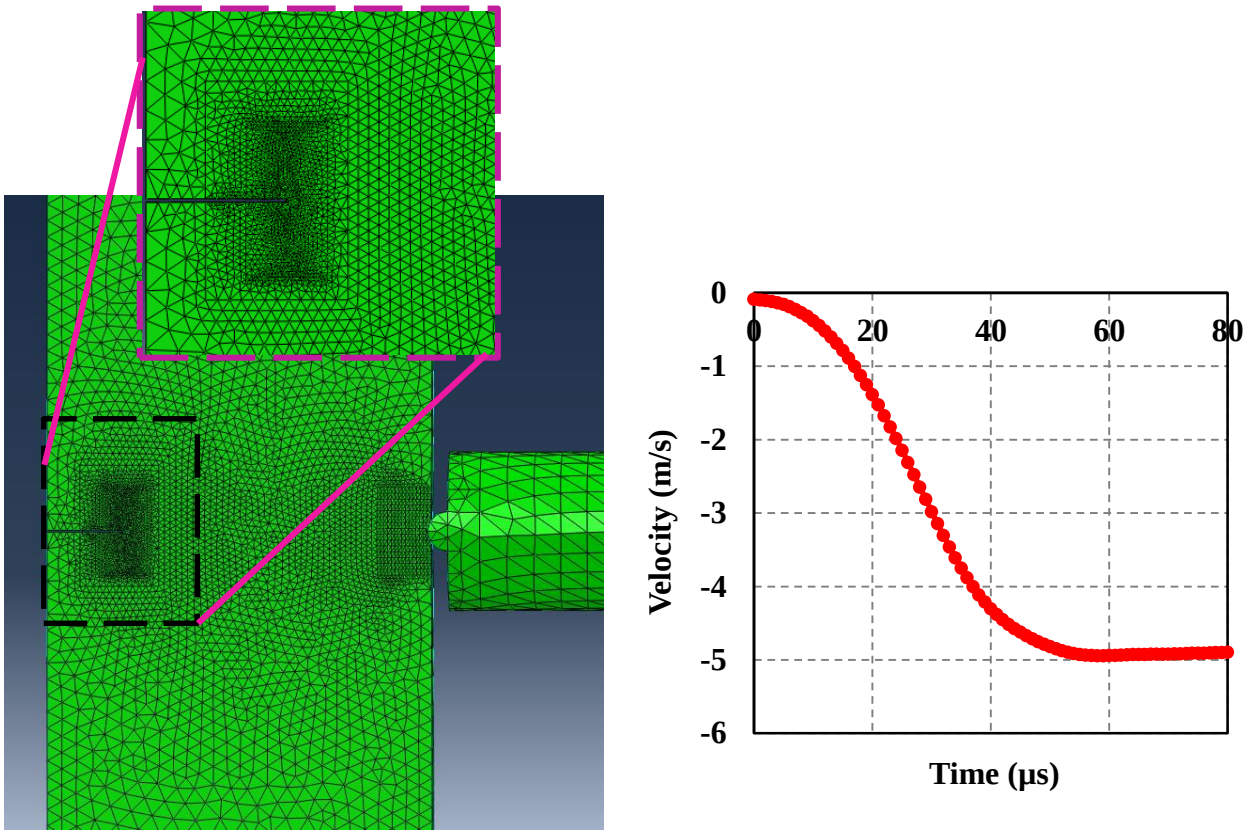

Figure 6.9: Finite element model used to simulate dynamic loading (left) and particle velocity history (right) used as an input to the simulation.

6.5 Mixed-mode crack-tip deformations

Figures 6.11 and 6.12 shows r-DGS contours due to surface deformations near the mixed-mode crack tip. The measured orthogonal surface slopes (Figure 6.11) for a few time instances are shown using the global coordinate system *x* and *y* defined at the crack tip aligned with the loading direction and the specimen edges as shown in the Figure 6.2. Figure 6.12 shows the surface gradient contours in global coordinates (a and c) and in local coordinates (b and d).

6.6 Extraction of stress intensity factors:

The stress intensity factors in pre-crack initiation phase was performed in the global coordinate system (*x* and *y*) defined at the crack tip aligned with the loading direction and the specimen edges, as shown in Figure 6.2(a). Stress intensity factors in the pre-crack initiation regime for a stationary but dynamically loaded crack was evaluated using the asymptotic equation given by [21, 42],

$$\frac{\phi_x(t)}{2}=\frac{\partial w(t)}{\partial x}=\frac{-\nu B}{2E}\left[\begin{array}{l}\left\{\left(A_1(t)(\frac{N}{2}-1)r^{((\frac{N}{2})-2)}\cos(\frac{N}{2}-2)\theta\right)\right\}\\+\left\{\left(B_1(t)(\frac{N}{2}-1)r^{((\frac{N}{2})-2)}\sin(\frac{N}{2}-2)\theta\right)\right\}\\+\sum_{N=2}^{\infty}\left\{\begin{array}{l}\left(A_N(t)(\frac{N}{2}-1)r^{((\frac{N}{2})-2)}\cos(\frac{N}{2}-2)\theta\right)+\\\left(B_N(t)(\frac{N}{2}-1)r^{((\frac{N}{2})-2)}\sin(\frac{N}{2}-2)\theta\right)\end{array}\right\}\end{array}\right] \tag{6.5}$$

where (r,θ) are polar coordinates centered at the crack tip in the global coordinates *x* and *y*, elastic modulus $E = 5.8$ GPa, thickness *B* = 8.9 mm and $A_1 = K_I\sqrt{\frac{2}{\pi}}$ with K_I being the mode-I stress intensity factor and $B_1 = K_{II}\sqrt{\frac{2}{\pi}}$, K_{II} being the mode-II stress intensity factor.

The stress intensity factor evaluation in the post-crack initiation regime was performed by orienting the surface slopes in the crack propagation direction. That is, along the local coordinates *x'* and *y'* as shown Figure 6.2(b). The orthogonal angular deflections of light rays and hence the respective surface slopes in the *x'* and *y'* directions were evaluated using the transformation,

$$\frac{\phi_x^{'}}{2} = \frac{\partial w}{\partial x^{'}} = \frac{\partial w}{\partial x}\cos\alpha + \frac{\partial w}{\partial y}\sin\alpha \tag{6.6}$$

where α is the instantaneous crack orientation angle. Examples of surface slope contours following this transformation are shown in Figure 6.12(b and d) for time instants 53.2 and 59.8 μsec. For steadily propagating cracks, stress intensity factors are evaluated by using,

$$\frac{\phi_x^{'}(t)}{2} = \frac{\partial w(t)}{\partial x^{'}} = \frac{-\nu B}{2E}\left[\begin{array}{l} f(V;C_L;C_S)\left\{\left(A_1(t)(\frac{N}{2}-1)r^{((\frac{N}{2})-2)}\cos(\frac{N}{2}-2)\theta^{'}\right)\right\} \\ +g(V;C_L;C_S)\left\{\left(B_1(t)(\frac{N}{2}-1)r^{((\frac{N}{2})-2)}\sin(\frac{N}{2}-2)\theta^{'}\right)\right\} \\ +\sum_{N=2}^{\infty}\left[\begin{array}{l}\left(A_N(t)(\frac{N}{2}-1)r^{((\frac{N}{2})-2)}\cos(\frac{N}{2}-2)\theta^{'}\right)+ \\ \left(B_N(t)(\frac{N}{2}-1)r^{((\frac{N}{2})-2)}\sin(\frac{N}{2}-2)\theta^{'}\right)\end{array}\right]\end{array}\right] \tag{6.7}$$

Where *f* and *g* denote functions associated with the instantaneous crack velocity, dilatational and shear wave speeds C_L and C_S respectively, and (r,θ') denote the crack tip polar coordinates ($\theta' = \theta + \alpha$) associated with the a growing crack. For plane stress the functions *f* and *g* are given by[44],

$$f(V;C_L,C_S) = \frac{\left(1+\alpha_S^2\right)\left(\alpha_L^2-\alpha_S^2\right)}{4\alpha_S\alpha_L - \left(1+\alpha_S^2\right)^2}$$

$$g(V;C_L,C_S) = \frac{2\alpha_S\left(1-\alpha_L^2\right)}{4\alpha_S\alpha_L - \left(1+\alpha_S^2\right)^2} \qquad (6.8),$$

where $\alpha_{L:S} = \sqrt{1-\frac{V^2}{C_{L:S}^2}}$. The instantaneous crack velocity for the propagating crack was calculated by measuring the change in the crack length between successive images and dividing by the time interval between them (1/framing rate). The dilatational and shear wave speeds were measured using ultrasonic pulse-echo measurements. A two term solution (N = 3) was used to extract the stess intensity factors and was found to capture the overall behavior of a mixed-mode crack well. Least-squares regression analysis was performed in the data range $\left(0.5 \le r/B \le 1.5\right)$ and $(-150 \le \theta' \le 150)$ to extract stress intensity factors. Figure 6.10 shows the extracted stress intensity factors. The error bars are due to different selection of the crack tip location in the regression analysis. Solid lines represent the stress intensity factors obtained from numerical simulation up to the time instance of crack propagation.

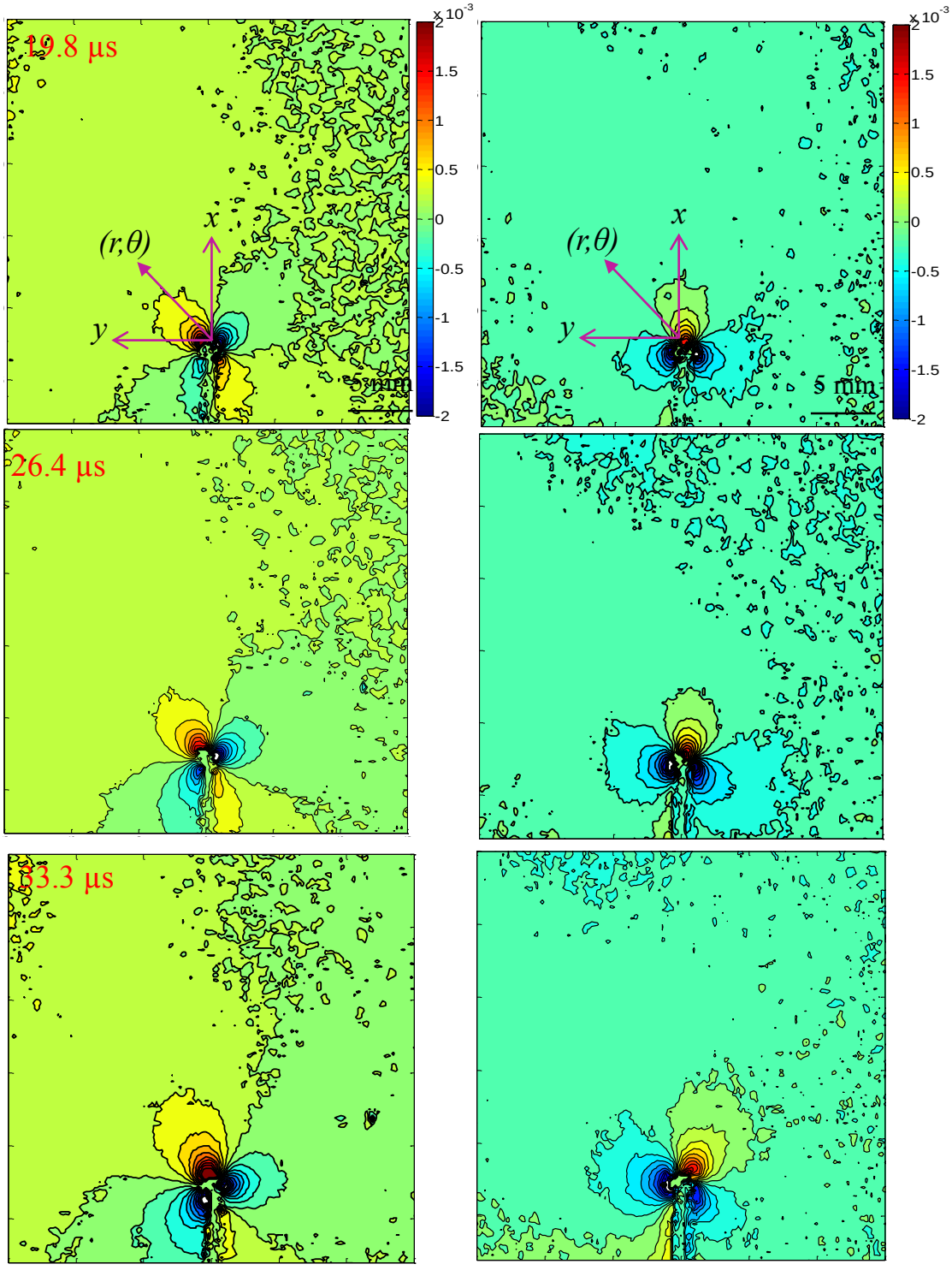

Figure 6.10: Experimental ϕ_x (column 1) and ϕ_y (column 2) contours near the crack-tip before and after crack initiation. Contours are plotted every 20 x 10^{-5} radian.

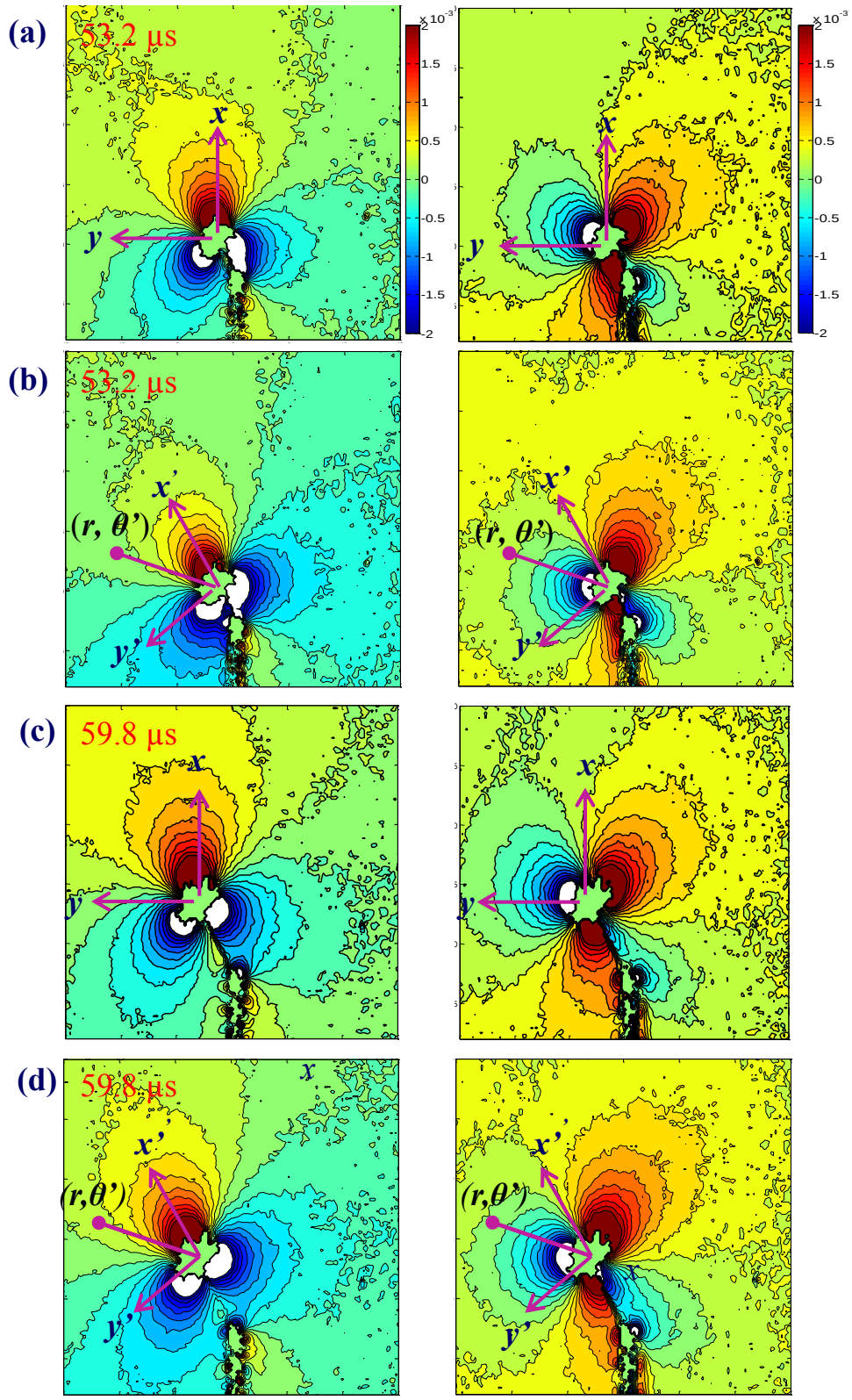

Figure 6.11: Experimental ϕ_x (column 1) and ϕ_y (column 2) contours near the crack-tip in global coordinates (a and c) and local coordinates (b and d). Contours are plotted every 20 x 10^{-5} radian.

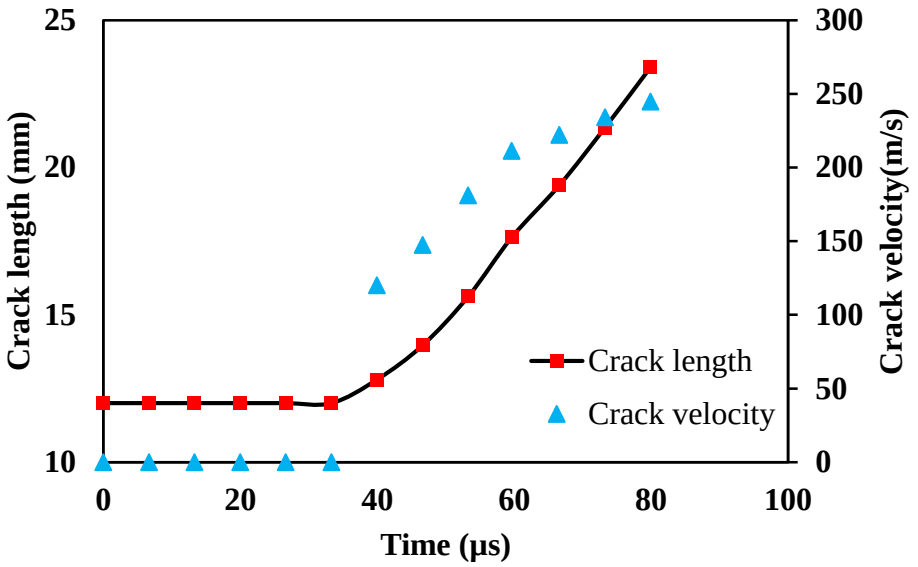

Figure 6.12: Crack growth and Crack velocity history in PMMA for mixed-mode loading.

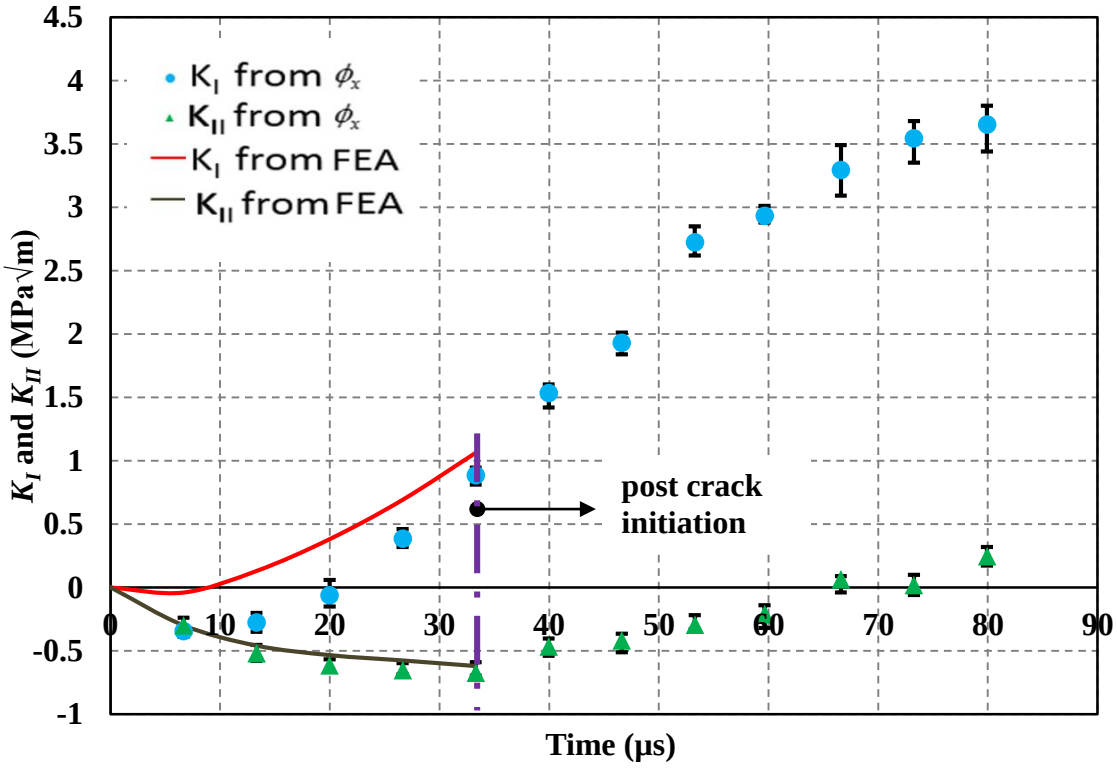

Figure 6.13: Dynamic mixed-mode stress intensity factor histories from overdeterministic regression analysis of surface gradient data. Solid line represents SIF histories from finite element analysis.

6.7 Finite element analysis

A 3D elasto-dynamic finite element simulation similar to mode-I as described earlier was performed using ABAQUS™/Explicit software package in parallel with the experiments. Similar to the mode-I case, simulation was limited to the extraction of dynamic stress intensity factors K_I and K_{II} for a dynamically loaded stationary crack. The model included a specimen and a long bar as shown in the Figure 6.11. The model consisted of 163,891 3D stress elements with a fine mesh

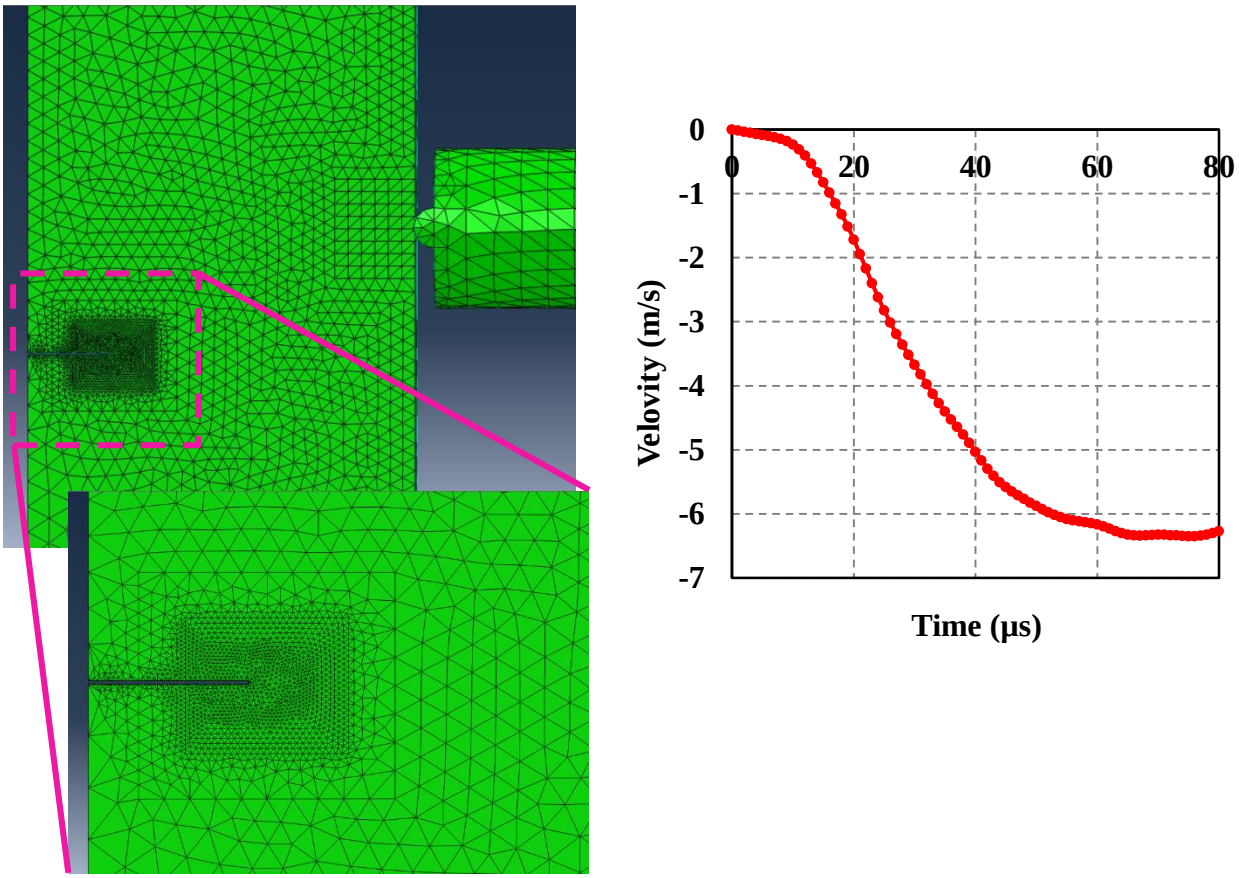

Figure 6.14: Finite element model used to simulate dynamic eccentric loading on an edge cracked PMMA plate (left) and particle velocity history (right) used as input during simulation.

near the crack tip having element size of 0.1 mm. The semicircular head of the long bar was aligned

in contact with the specimen and the particle velocity measured from the strain history as described earlier was used as input to the simulation. The particle velocity of the long bar is as shown in the Figure 6.14 (right). Stress intensity factors were calculated using the crack opening and sliding displacement of the upper and lower faces using[39],

$$K_I(t) = \frac{E\sqrt{2\pi}}{8\sqrt{r}}\left(u_{2-upper} - u_{2-lower}\right)\Big|_{(r,\theta=\pi)}$$
$$K_{II}(t) = \frac{E\sqrt{2\pi}}{8\sqrt{r}}\left(u_{1-upper} - u_{1-lower}\right)\Big|_{(r,\theta=\pi)} \qquad (6.10)$$

where E = 5.8 GPa is the dynamic elastic modulus of PMMA and u_2 is crack opening displacement and u_1 corresponds to crack sliding displacement. In-plane displacements of the crack faces were requested every 6.6 μsec and the stress intensity factors corresponding to each time instance were evaluated and superimposed with the experimental data up to the crack initiation period as shown in the Figure 6.14. Initially mode-I stress intensity factor is negative due to the eccentric loading causing the crack flanks to close. As the time progresses the crack starts to open which results in mode-I stress intensity factor to become positive. Mode-II stress intensity factor is negative and consistent with the imposed loading. Further, it monotonically increases in magnitude until the crack initiates. After crack initiation, magnitude of mode-II stress intensity factor decreases to zero as the crack reorients and propagates in a locally mode-I condition.

Conclusions

A full-field optical technique called reflection-mode Digital Gradient Sensor (r-DGS) was implemented in this thesis for measuring small angular deflections in solids subjected to mechanical loading. The working principle of r-DGS has been explained along with its governing equations. The measured components of light rays in two mutually orthogonal planes are related to surface slopes. The method uses a relatively simple experimental setup - a digital recording device, white light illumination, a randomly decorated gray scale (speckle pattern), and image correlation software - makes it a easy to implement yet robust tool for characterizing mechanical behavior of reflective materials. Several benchmark experiments have been performed to validate the r-DGS principle.

The method has been successfully implemented to study deformation of thin plates due to quasi-static and dynamic loading in the out-of-plane direction. The measured surface slopes in quasi-static case were in good agreement with the closed form solution for a clamped circular plate subjected to central deflection. The curvatures evaluated from the surface slopes also showed a good agreement with the ones from the closed form solution for the problem. Further, the surface topography evaluated from the measured slopes show a good agreement when compared to the applied out-of-plane displacement. The role of various experimental parameters such as speckle characteristics, object plane to target plane distance, sub-image size and pixel overlap used during image correlation, have all been examined. The transient deformation of a plate subjected to a single-point projectile impact has been studied by implementing r-DGS in conjunction with high-

speed photography. The evolution of surface slope fields were measured from impact initiation instant until stress waves reflect off the free edges of a 'free-free' circular plate. The slope fields showed qualitative resemblance with the quasi-static counterparts of a clamped plate subjected to central deflection until the reflected stress waves returned to the impact point. The estimated topographical information at different instants of time corresponding to the high-speed camera recording rate was in good agreement with a complementary elasto-dynamic finite element simulation of the problem.

The r-DGS technique has also been demonstrated as a potential NDE tool for damage and disbond detection in layered materials. The embedded disbond in an adhesively bonded bi-layered PMMA was detected by subjecting it to thermal excitation and mapping the resulting surface slope fields. The anomaly in the surface gradient contours in an otherwise uniform field revealed the presence of disbond in the interior region. Delamination detection due to mechanical impact on glass fibers reinforced epoxy composite plate was also undertaken. An impact damages composite plate was studied by mapping surface slopes using thermal excitation. The footprint of the impactor head was seen when the surface gradient were mapped using r-DGS confirming the presence of damage in the plate.

The r-DGS method has also been successfully implemented to measure surface slopes around mode-I and mixed-mode (mode I + mode II) crack tip under both quasi-static and dynamic loading conditions. In the quasi-static case, edge cracked samples with vertical and inclined cracks were subjected to three-point bending resulting in symmetric and asymmetric deformations respectively. Stress-intensity factors were evaluated by performing an over-deterministic least squares regression analysis of the measured surface gradient fields using asymptotic crack-tip field equations. In the inclined crack case, transformation of orthogonal slope fields in the direction of

the crack was adopted. The stress intensity factors from experiments have been successfully complemented by the analytical and finite element simulations. Dynamic fracture experiments under mode-I and mixed-mode conditions have been carried out using 'free-free' edge cracked samples subjected to stress-wave loading in a long-bar impactor apparatus. Symmetrically and eccentrically loaded 1-point impact samples have been monitored using r-DGS and a high-speed camera (150,000 frames/sec) for making time-resolved measurements before and after crack initiation. A self-similarly growing mode-I crack and a kinked mixed-mode crack occur following initiation in symmetric and eccentric loading cases. These optical measurements have been analyzed using crack tip fields corresponding to elasto-dynamic steady-state growth assumptions to estimate pre- and post-crack initiation stress intensity factors. The method of transforming the measured surface slopes in the instantaneous crack growth direction, developed under static counterparts, has been utilized for extracting dynamic fracture parameters. Complementary elasto-dynamic analyses support experimental measurements until crack initiation.

References

1. Ligtenberg, F.K., Proc. Soc. Exp. Stress Anal. 12, 83 (1954).
2. Rieder, G. and R. Ritter, *Krümmungsmessung an belasteten Platten nach dem Ligtenbergschen Moiré-Verfahren.* Forschung im Ingenieurwesen A, 1965. **31**(2): p. 33-44.
3. Chiang, F.P. and G. Jaisingh, *Dynamic moiré methods for the bending of plates.* Experimental Mechanics, 1973. **13**(4): p. 168-171.
4. Chiang, F.P. and C.J. Lin, *Time-average reflection-moiré method for vibration analysis of plates.* Applied Optics, 1979. **18**(9): p. 1424-1427.
5. Archbold, E. and A.E. Ennos, *Displacement Measurement from Double-exposure Laser Photographs.* Optica Acta: International Journal of Optics, 1972. **19**(4): p. 253-271.
6. Chiang, F.-P. and R.-M. Juang, *Laser speckle interferometry for plate bending problems.* Applied Optics, 1976. **15**(9): p. 2199-2204.
7. Chiang, F.P. and Q.B. Li, *Real-time laser speckle photography.* Applied Optics, 1984. **23**(24): p. 4469-4470.
8. Mohan, N.K., H. Saldner, and N.E. Molin, *Electronic speckle pattern interferometry for simultaneous measurement of out-of-plane displacement and slope.* Optics Letters, 1993. **18**(21): p. 1861-1863.
9. Gindl, W. and U. Müller, *Shear strain distribution in PRF and PUR bonded 3–ply wood sheets by means of electronic laser speckle interferometry.* Wood Science and Technology, 2006. **40**(5): p. 351-357.
10. Chiang, F.D. and R.P. Khetan, *Strain analysis by one-beam laser speckle interferometry. 2: Multiaperture method.* Applied Optics, 1979. **18**(13): p. 2175-2186.
11. Chen F. , C.Z., Fang R. , and Chen P. , *Dynamic deformation measurement by mismatch white light speckle method.* Appl. Math. Mech.,, 1986. **9**: p. 102–106.
12. F. Chen, C.T.G., and Y. Y. Hung, , *Digital speckle metrology: Techniques and applications* SEM Proc, 1996: p. 483–486.
13. Chiang, F.-P., *Evolution of white light speckle method and its application to micro/nanotechnology and heart mechanics.* Optical Engineering, 2003. **42**(5): p. 1288-1292.
14. Kao, T.Y. and F.P. Chiang, *Family Of Grating Techniques Of Slope And Curvature Measurements For Static And Dynamic Flexure Of Plates.* Optical Engineering, 1982. **21**(4): p. 214721-214721-.
15. Subramanian, G. and P.N. Akella, *A selective diffraction order based lens plane grating shearing interferometer for the study of bent plates.* Strain, 1987. **23**(2): p. 55-59.
16. Subramanian, G., K.J. Rose, and A. Subramania, *TECHNIQUES: A MULTIPLEXED GRATING SHEARING INTERFEROMETER FOR REFLECTION MOIRÉ ANALYSIS OF PARTIAL SLOPES AND CURVATURES OF BENT PLATES.* Experimental Techniques, 2000. **24**(5): p. 27-30.

17. Hung, Y.Y., *Shearography: A New Optical Method For Strain Measurement And Nondestructive Testing.* Optical Engineering, 1982. **21**(3): p. 213391-213391-.
18. Lee, J.-R., J. Molimard, A. Vautrin, and Y. Surrel, *Application of grating shearography and speckle shearography to mechanical analysis of composite material.* Composites Part A: Applied Science and Manufacturing, 2004. **35**(7): p. 965-976.
19. Toh, S., F. Chau, V. Shim, C. Tay, and H. Shang, *Application of shearography in nondestructive testing of composite plates.* Journal of materials processing technology, 1990. **23**(3): p. 267-275.
20. Tippur, H.V. and A.J. Rosakis, *Quasi-Static and Dynamic Crack-Growth Along Bimaterial Interfaces - a Note on Crack-Tip Field-Measurements Using Coherent Gradient Sensing.* Experimental Mechanics, 1991. **31**(3): p. 243-251.
21. Tippur, H.V., S. Krishnaswamy, and A.J. Rosakis, *Optical mapping of crack tip deformations using the methods of transmission and reflection coherent gradient sensing: a study of crack tip K-dominance.* International Journal of Fracture, 1991. **52**(2): p. 91-117.
22. Tippur, H.V., *Simultaneous and real-time measurement of slope and curvature fringes in thin structures using shearing interferometery.* Optical Engineering, 2004. **43**(12): p. 3014-3020.
23. Kirugulige, M. and H. Tippur, *Mixed-mode dynamic crack growth in functionally graded glass-filled epoxy.* Experimental Mechanics, 2006. **46**(2): p. 269-281.
24. Tippur, H. and S. Ramaswamy, *Measurement of mixed-mode fracture parameters near cracks in homogeneous and bimaterial beams.* International Journal of Fracture, 1993. **61**(3): p. 247-265.
25. Rousseau, C.-E. and H. Tippur, *Dynamic fracture of compositionally graded materials with cracks along the elastic gradient: experiments and analysis.* Mechanics of Materials, 2001. **33**(7): p. 403-421.
26. Rousseau, C.E. and H.V. Tippur, *Evaluation of crack tip fields and stress intensity factors in functionally graded elastic materials: Cracks parallel to elastic gradient.* International Journal of Fracture, 2002. **114**(1): p. 87-112.
27. Liu, C., A.J. Rosakis, R.W. Ellis, and M.G. Stout, *A Study of the Fracture Behavior of Unindirectional Fiber- Reinforced Composite Using Coherent Gradient Sensing (CGS) Interferometry.* International Journal of Fracture, 1998. **90**(4): p. 355-382.
28. Lee, H., A.J. Rosakis, and L.B. Freund, *Full-field optical measurement of curvatures in ultra-thin-film–substrate systems in the range of geometrically nonlinear deformations.* Journal of Applied Physics, 2001. **89**(11): p. 6116-6129.
29. Park, T.S., S. Suresh, A.J. Rosakis, and J. Ryu, *Measurement of full-field curvature and geometrical instability of thin film-substrate systems through CGS interferometry.* Journal of the Mechanics and Physics of Solids, 2003. **51**(11–12): p. 2191-2211.
30. Tippur, H., S. Krishnaswamy, and A. Rosakis, *A coherent gradient sensor for crack tip deformation measurements: analysis and experimental results.* International Journal of Fracture, 1991. **48**(3): p. 193-204.

31. Periasamy, C. and H.V. Tippur, *A full-field reflection-mode digital gradient sensing method for measuring orthogonal slopes and curvatures of thin structures.* Measurement Science & Technology, 2013. **24**(2).
32. Periasamy, C., *Digital Gradient Sensing (DGS) : A Full-Field Optical Technique to Measure Angular Deflections of Light Rays and Its Applications to Failure Mechanics.* 2012.
33. Periasamy, C. and H.V. Tippur, *A full-field reflection-mode digital gradient sensing method for measuring orthogonal slopes and curvatures of thin structures.* Measurement Science and Technology, 2013. **24**(2): p. 025202.
34. Periasamy, C., *Digital Gradient Sensor(DGS) : A full field optical technique to measure angular deflections of light rays and its application to failure mechanics*. 2012, Auburn University.
35. Periasamy, C. and H. Tippur, *Measurement of orthogonal stress gradients due to impact load on a transparent sheet using digital gradient sensing method.* Experimental Mechanics, 2013. **53**(1): p. 97-111.
36. Ambu, R., F. Aymerich, F. Ginesu, and P. Priolo, *Assessment of NDT interferometric techniques for impact damage detection in composite laminates.* Composites Science and Technology, 2006. **66**(2): p. 199-205.
37. M. Janssen, J. Zuidema, and R.J.H. Wanhill,. "Fracture Mechanics", 2 ed, VSSD,2006.
38. Kirugulige, M.S. and H.V. Tippur, *Mixed-Mode Dynamic Crack Growth in Functionally Graded Glass-Filled Epoxy.* Experimental Mechanics, 2006. **46**(2): p. 269-281.
39. Beinert, J. and J.F. Kalthoff, *Mechanics of Fracture*, ed. G.C.Sih. Vol. Vol. 7. 1981,Nijhoff Publishers
40. Rousseau, C.-E. and H. Tippur, *Influence of elastic gradient profiles on dynamically loaded functionally graded materials: cracks along the gradient.* International Journal of Solids and Structures, 2001. **38**(44): p. 7839-7856.
41. Periasamy, C., R. Jhaver, and H. Tippur, *Quasi-static and dynamic compression response of a lightweight interpenetrating phase composite foam.* Materials Science and Engineering: A, 2010. **527**(12): p. 2845-2856.
42. Williams, M., *J Appl Mech.* 1959. **24**: p. 109-114.
43. Butcher, R.J., C.E. Rousseau, and H.V. Tippur, *A functionally graded particulate composite: Preparation, measurements and failure analysis.* Acta Materialia, 1998. **47**(1): p. 259-268.
44. Periasamy, C. and H.V. Tippur, *Measurement of crack-tip and punch-tip transient deformations and stress intensity factors using Digital Gradient Sensing technique.* Engineering Fracture Mechanics, 2013. **98**: p. 185-199.